ABSTRACT

Title of Document: THE GENERATION AND APPLICATIONS OF A SPECTRALLY RESOLVED INFRARED RADIANCE CLIMATOLOGY DERIVED FROM THE ATMOSPHERIC INFRARED SOUNDER

Mitchell David Goldberg, Doctor of Philosophy, 2009

Directed By: Professor Eugenia Kalnay and Professor Zhanqing Li, Department of Atmospheric and Ocean Sciences

There is growing consensus that persistent and increasing anthropogenic emissions, since the beginning of the industrial revolution in the 19th century, are increasing atmospheric temperatures, increasing sea levels, melting ice caps and glaciers, increasing the occurrence of severe weather, and causing regional shifts in precipitation patterns. Changes in these parameters or occurrences are responses to changes in climate forcing terms, notably greenhouse gases. The NASA Atmospheric InfraRed Sounder (AIRS), launched in May of 2002, is the first high spectral resolution infrared sounder with nearly complete global coverage on a daily basis. High spectral resolution in the infrared provides sensitivity to nearly all climate forcings, responses and feedbacks. The AIRS radiances are sensitive to

changes in carbon dioxide, methane, carbon monoxide, ozone, water vapor, temperature, clouds, aerosols, and surface characteristics. This study uses the raw AIRS data to generate the first ever spectrally resolved infrared radiance (SRIR) dataset (2002- 2006) for monitoring changes in atmospheric temperature and constituents and for assessing the accuracy of climate and weather model analyses and forecasts. The SRIR dataset is a very powerful tool. Spectral signatures derived from the dataset confirmed the largest depletion of ozone over the Arctic in 2005, and also verified that the European Center for Medium Range Weather (ECMWF) model analysis water vapor fields are significantly more accurate than the analyses of the National Centers for Environmental Prediction (NCEP). The NCEP moisture fields are generally 20% more moist than those from ECMWF. This research included computations of radiances from NCEP and ECMWF atmospheric states and compared the calculated radiances with those obtained from the SRIR dataset. Comparisons showed very good agreement between the SRIR data and ECMWF simulated radiances, while the agreement with NCEP values was rather poor. Interannual differences of radiances computed from ECMWF analyses were nearly identical to those derived from the SRIR dataset, while the corresponding NCEP interannual differences were in poorer agreement. However, further comparisons with the SRIR dataset in 2006 found degradation in the ECMWF upper tropospheric water vapor fields due to an operational change in ECMWF assimilation procedures. This unexpected result demonstrates the importance of continuous routine monitoring. The SRIR climatology will be extended into the future using AIRS and other high spectral resolution sounders.

THE GENERATION AND APPLICATIONS OF A SPECTRALLY RESOLVED INFRARED RADIANCE CLIMATOLOGY DERIVED FROM THE ATMOSPHERIC INFRARED SOUNDER.

By

Mitchell D. Goldberg

Dissertation submitted to the Faculty of the Graduate School of the
University of Maryland, College Park, in partial fulfillment
of the requirements for the degree of
Doctor of Philosophy
2009

Advisory Committee:
Professor Eugenia Kalnay, Co-Chair
Professor Zhanqing Li, Co-Chair
Professor Rachel Pinker
Professor Kayo Ide
Professor Shunlin Liang, Dean's representative

Dedication

To my wife Ruth, my children Stephanie and Joshua for your love and support. To my father Kenneth Goldberg; his never-ending love and encouragement kept me on course.

Acknowledgements

First and foremost, I would like to thank my family for their continuous support and love. None of my achievements in my professional career would have been possible without the most important achievement of all: my family.

I am grateful to my committee, led by Professors Kalnay and Li. Their encouragement and guidance resulted in a study which I anticipate will stimulate continued research and new findings. I would also like to thank my employer, the National Ocean and Atmospheric Administration, NOAA, for numerous career opportunities. I am also grateful to the NASA, since most of this work was accomplished through my AIRS science team funding. I would like to thank my AIRS support team at NOAA, particularly Lihang Zhou for help in algorithm coding and analysis.

Table of Contents

List of Tables

List of Figures

Chapter 1: Background and Scope of the Dissertation

1.1 Background and motivation

There is growing consensus that persistent and growing anthropogenic emissions over the past 150 years are causing increases in atmospheric and ocean temperatures, rising sea levels, melting ice caps and glaciers, more frequent severe weather, and regional shifts in precipitation patterns. Changes in these parameters or occurrences are responses to changes in climate forcing terms. Key climate forcing terms include solar irradiance, aerosols, and greenhouse gases of carbon dioxide (CO_2), methane (CH_4), ozone (O_3), and Nitric Acid (N_2O). Climate forcing terms are external variables that control climate. Response terms are variables responding to climate forcing and include temperature, precipitation, wind, and sea level. Feedback terms are variables which not only respond to climate forcing but can also modify climate forcing. These variables include clouds, vegetation, snow and ice cover and earth radiation budget. As reported in the Intergovernmental Panel on Climate Change Fourth Assessment Report [*IPCC*, 2007], "Warming of the climate system is unequivocal, as is now evident from observations of increases in global average air and ocean temperatures, widespread melting of snow and ice, and rising global average sea level". Fig.1.1 is from the IPCC report and clearly illustrates the increase of greenhouse gas emissions. Global atmospheric concentrations of CO_2, CH_4 and N_2O are increasing rapidly and far exceed pre-industrial values determined from ice cores spanning many thousands of years. The major contributor to global increases in

CO_2 concentrations is the combustion of fossil fuel, with land-use change providing another significant but smaller contribution. The observed increase in CH_4 concentration has contributions from both agriculture and fossil fuel. The increase in N_2O concentration is due to agriculture. Increase of greenhouse gases has a positive radiative forcing influence, which warms the climate. Fig. 1.2, shows that the increase in radiative forcing due to CO_2, CH_4 and N_2O from 1750 to 2005 was +2.3 W/m^2, with a 5% and 95% uncertainty range of [+2.1 to +2.5] W/m^2. The CO_2 radiative forcing increased by 20% from 1995 to 2005, the largest change for any decade in at least the last 200 years. Reduction in stratospheric ozone caused by CFCs has resulted in a positive radiative forcing of 0.35 [0.25 to 0.65] W/m^2 in the troposphere and a slight negative forcing of -0.05 [-0.15 to 0.05] W/m^2 in the stratosphere. Aerosols, on the other hand, have a net negative radiative forcing. Anthropogenic contributions to aerosols (primarily sulphate, organic carbon, black carbon, nitrate and dust) together produce a cooling effect, with a total direct radiative forcing since 1750 of -0.5 [-0.9 to -0.1] W/m^2 and an indirect cloud albedo forcing of -0.7 [-1.8 to -0.3] W/m^2. The total net radiative forcing is 1.6 [0.6 to 2.4] W/m^2.

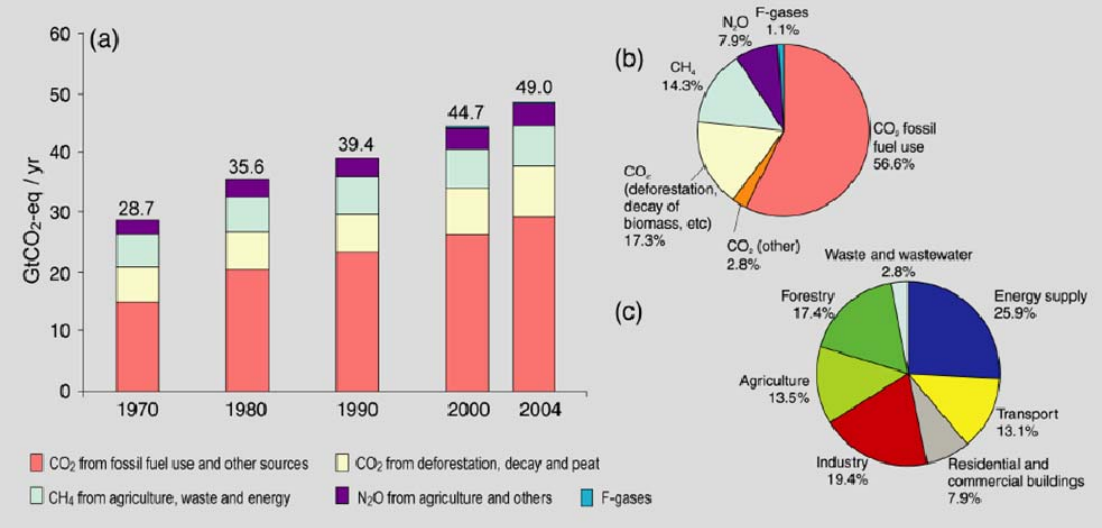

Fig. 1.1: From IPCC 4th Assessment Report, Global annual emissions of anthropogenic GHGs from 1970 to 2004.5 (b) Share of different anthropogenic GHGs in total emissions in 2004. (c) Share of different sectors in total anthropogenic GHG emissions in 2004

.

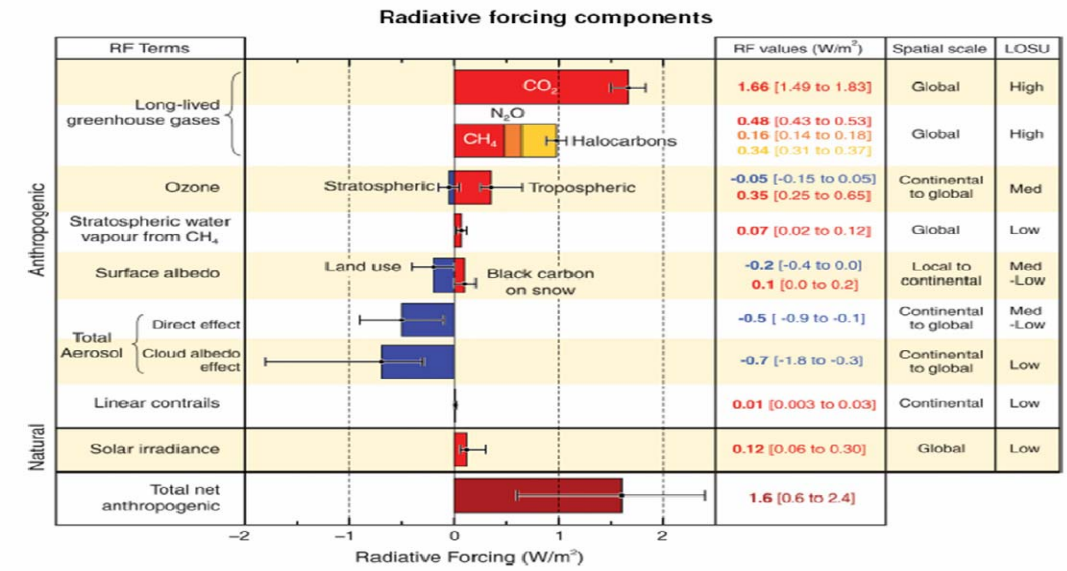

Fig. 1.2: From IPCC 4th Assessment Report, Global-average radiative forcing (RF) in 2005 (best estimates and 5-95% uncertainty ranges) with respect to 1750 for CO_2, CH_4, N_2O and other important agents and mechanisms, together with the typical geographical extent (spatial scale) of the forcing and the assessed level of scientific understanding (LOSU). Aerosols from explosive volcanic eruptions contribute an additional episodic cooling term for a few years following an eruption.

The response to increasing forcings is an increase in global temperatures at a rate of about 0.2 C per decade over the past 30 years, with regional change as much as 2 degrees per decade, which has been observed over Alaska. Fig. 1.3 displays the change in surface temperature, sea level, and snow cover since 1850, relative to the 30 year 1961- 1990 climatological average. Note the acceleration in surface temperature warming during the past twenty years, the decrease in snow cover during this period, and the consistent increase in sea level since 1930.

Climate models are projecting continuation of rising surface temperature, with an increase between 2 and 5 C by 2100. This large range has a dependency on different scenarios for future greenhouse gas emissions, with the 5% and 95% uncertainty range corresponding to 1 to 6.5 C, respectively.

Observing and documenting temperature change are very important to ensure future projections are valid. Climate model projections of global surface temperature in the first IPCC report in 1990 ranged between about 0.15 and 0.3°C per decade from 1990 to 2005, which now can be compared with observed values of about 0.2°C per decade. The agreement between the 1990 projections and the actual change over the 15 year period since 1990 has increased the confidence in decadal projections. However, to understand the root causes of climate change and to achieve more reliable longer range projections, we need to observe and document, in addition to temperature, changes in the forcing, feedback and response variables discussed above. There are many different observing strategies including collecting meteorological data from weather stations, trace gases measurements from airborne

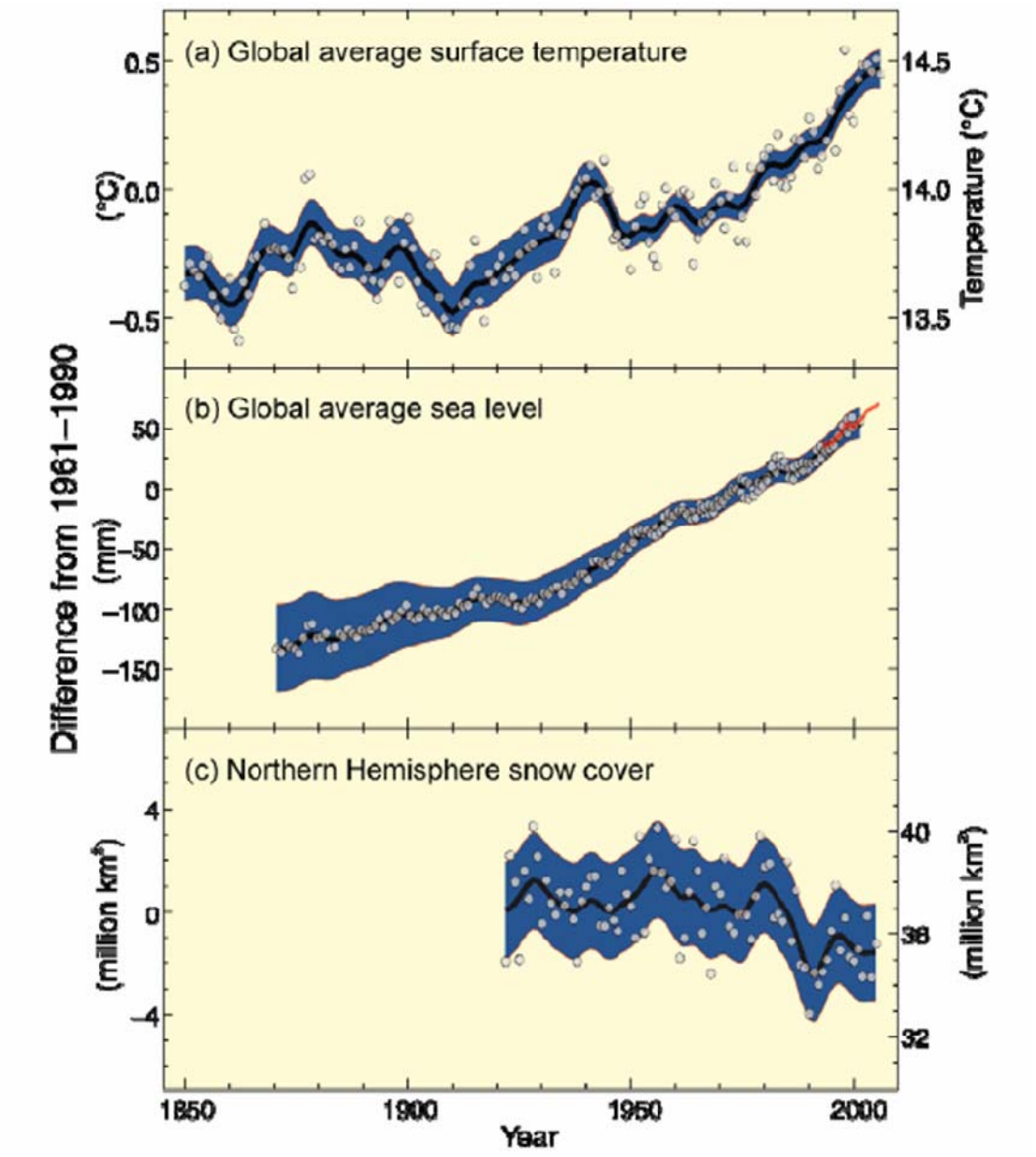

Fig. 1.3. From IPCC 4th Assessment Report, Observed changes in (a) global average surface temperature; (b) global average sea level from tide gauge (blue) and satellite (red) data and (c) Northern Hemisphere snow cover for March-April. All differences are relative to corresponding averages for the period 1961-1990. Smoothed curves represent decadal averaged values while circles show yearly values. The shaded areas are the uncertainty intervals estimated from a comprehensive analysis of known uncertainties (a and b) and from the time series (c).

and ground-based instruments, and satellite remote sensing. In situ observations from ground and aircraft usually have the best accuracy, but the major shortfall is not being able to make daily global contiguous measurements. Satellite remote sensing on the other hand has very good global coverage but often lacks high vertical resolution. Fortunately for many climate applications, data are averaged over monthly time scales and instantaneous observations with restricted vertical resolution are not a limiting factor. For example, deep-layer mean temperatures of 2- 4 km are sufficient for monitoring temperature change because the impact of climate forcing should be well mixed in the vertical at monthly and annual time scales [*Spencer and Christy*, 1992; *Goldberg and Fleming*, 1995; *Mears et al.*; 2003, *Vinnikov and Grody*, 2003; *Zou et al.*, 2006].

The research described in this dissertation applies infrared measurements from the Atmospheric InfraRed Sounder (AIRS) on the NASA AQUA satellite to produce and establish a first ever high quality spectrally resolved radiance climatology for the purpose of detecting and monitoring climate change, to better understand the sources, sinks and distribution of trace gases, and to validate weather and climate models. The concept for using spectrally resolved radiances for validating the realism of climate models was first suggested by *Goody et al.* [1998]. The AIRS, launched in May of 2002, is the first high spectral resolution infrared sounder with nearly complete global coverage on a daily basis [*Aumann* et al., 2003]. High spectral resolution in the infrared provides sensitivity to nearly all forcing, response and feedback terms. Specifically AIRS is sensitive to changes in CO_2, CH_4, carbon monoxide (CO), O_3, N_2O, water vapor (H_2O), aerosols, temperature, clouds, and

surface characteristics. Over the past 30 years, broadband instruments, such ERBE [*Barkstrom*, 1984] and CERES [*Wielicki* et al., 1996] have been used to measure the outgoing longwave radiation (OLR) as a fundamental climate measurement. The high spectral resolution of AIRS will allow for the first time to understand the root cause of changes in OLR, by observing changes in the spectral signature. Simulating AIRS using radiative transfer and atmospheric state variables from numerical weather and climate models will allow us to validate the accuracy of the model by directly comparing simulated with observed data.

1.2 Research and study objectives

The objectives of this study are to generate a multiyear Spectrally Resolved Infrared Radiance (SRIR) dataset from AIRS and to demonstrate the applications of this dataset to describing interannual/interseasonal and global/regional changes in climate. The dataset will also be used to validate and understand differences in the NCEP and ECMWF atmospheric analysis fields. A multiyear SRIR dataset has never been produced before, and it will be derived using scientific techniques which I have developed and adapted to AIRS over the past few years. These techniques have not been published, but have been demonstrated to the AIRS Science Team.

The specific steps in generating the SRIR dataset from AIRS include:

1. The use of principal component analysis to assess the quality of the individual spectrally resolved radiance observations and to reject radiances not meeting a quality threshold (2 sigma of expected instrumental noise)

2. Limb adjustment of the radiances to remove the effect of viewing geometry. This step is crucial in generation of monthly global fields and must be demonstrated to be accurate.
3. Averaging of the limb adjusted observations to a monthly 2 x 0.5 degree latitude/longitude field. Also, retaining the individual observations (original and limb adjusted) in a daily non-averaged grid.

The specific steps in generating the outgoing radiances from model analyses include:

1. Simulate cloud-free AIRS radiances, at the AIRS viewing geometry and nadir, using Stand-Alone Radiative Transfer Algorithm (SARTA), [*Strow et al.*, 2003] from ECMWF and NCEP analyses fields. Create daily and monthly gridded datasets at the same spatial resolution as the SRIR datasets.

Results from this research include: a) demonstration of the high accuracy of the limb adjustment procedure, b) utilization of the SRIR datasets to detect interannual /regional changes in the observed spectra attributable to changes in temperature, moisture and GHG concentrations, and c) validation of model-derived atmospheric states from NCEP and ECMWF analyses. This dataset will be continued into the future using the MeTOP Infrared Atmospheric Sounding Interferometer (IASI) and the NPOESS Cross-track InfraRed Sounder (CrIS).

The scientific goals for this research are:

1. Demonstrate the fidelity of AIRS using the SRIR dataset to capture signals caused by annual and regional changes in atmospheric temperature and atmospheric greenhouse gases, including ozone.
2. Quantify NCEP and ECMWF model errors using AIRS as a benchmark (truth), determine which model agrees better with AIRS, and understand the role of model physics and data assimilation in causing differences between models.

The scientific hypotheses I am testing are:

1. The AIRS SRIR dataset can detect spatial and temporal changes in atmospheric temperature and greenhouse gases, including ozone.
2. The AIRS SRIR dataset not only can check which model fields (NCEP or ECMWF) best fit the AIRS data, but can also be used to understand the root causes of the differences (model physics or lack of AIRS data). Data denial can be tested because during the AIRS time period, there were times when both NCEP and ECMWF did not assimilate AIRS data, including times when ECMWF assimilated AIRS and NCEP did not.

1.3: Organization of the dissertation

The paper is organized in the following sections. Section 2 begins with an overview of the AIRS instrument, followed by subsections on infrared remote sensing theory, AIRS science objectives, applications of spectrally resolved radiances, and the research and study objectives of this paper. Section 3 discusses the critical steps need to generate a high quality spectrally resolved radiance climatology. Section 4

discusses the validation of the principal component analysis and the limb adjustment procedure. Section 5 demonstrates applications of the radiance climatology, and Section 6 provides the summary and a discussion of future work.

1.4: Statement of originality

During the course of my doctoral studies, I performed the following:

- Developed a method to adjust AIRS observations to account for viewing geometry and demonstrate the accuracy of the methodology by comparing adjusted AIRS observations with those computed from ECMWF analyses using the AIRS radiative transfer algorithm SARTA.

- Generated a global representative set of empirical orthogonal functions (i.e., eigenvectors) of the AIRS data using principal component analysis (PCA), and demonstrated the ability of the PCA to filter instrumental noise and reproduce the original AIRS brightness temperatures within the instrumental noise level. I developed the PCA methodology used for AIRS. The description of the methodology included in the dissertation is also described in [*Goldberg et al*., 2003].

- Computed the AIRS radiance climatology, which consists of daily and monthly data sets of angle (limb) adjusted brightness temperatures for 2003 – 2006. The radiance climatology is produced for all sky and clear conditions. The clear detection algorithm is the one I produced as a member of the AIRS

science team. It is slightly modified from the algorithm I described in [*Goldberg et al*., 2003].

- Simulated brightness temperatures from ECMWF and NCEP atmospheric analyses for the purpose of determining which model is more accurate. This demonstrated the importance of the AIRS radiance climatology for validating model generated analyses.

- Compared interannual differences of AIRS spectra to demonstrate a capability to detect anomalous events. The event described in the dissertation is a significant reduction of ozone in the Arctic winter in 2005. This demonstrated the importance of the AIRS radiance climatology for detecting anomalous events with the long term goal of extending this dataset well into the future (2020s) using AIRS, IASI, and CrIS.

Chapter 2: Introduction to AIRS, Infrared Radiative Transfer and Applications of Spectrally Resolved Radiances

2.1 AIRS instrument

Infrared sounders on satellites observing the Earth were primarily designed to enable the retrieval of vertical profiles of atmospheric temperature and water vapor for use in numerical weather prediction models. Even though the infrared spectrum contains information on important greenhouse gases, the spectral resolution of the first generation of operational infrared sounders, the National Oceanic Atmospheric Administration's (NOAA) High resolution InfraRed Sounder (HIRS) [*Kidwell,* 1990], was inadequate to measure changes in greenhouse gases. A series of HIRS instruments dating back to 1979 continues to observe the Earth's surface and atmosphere using 19 spectrally broad channels. The high resolution in the acronym HIRS, notable for the time, referred to the spatial resolution near nadir of 18 km. High spectral resolution with near global daily coverage became available with the launch of the NASA Atmospheric InfraRed Sounder (AIRS) in May 2002. AIRS has 2378 channels measuring outgoing radiance between 650 cm-1 and 2675 cm-1 wavenumbers which is equivalent to wavelength, λ, range of 15.38 to 3.74microns. The AIRS is a cryogenic cooled (155 K) array grating spectrometer operating over the entire AIRS infrared (IR) spectral range at a spectral resolution ($\lambda / \Delta \lambda$) of 1200 [*Aumann et al*., 2003]. A grating disperses infrared energy across arrays of high-sensitivity HgCdTe detectors. In contrast the spectral resolution of HIRS is approximately 70. AIRS looks toward the ground through a cross-track rotary scan

mirror which provides +/- 49.5 degrees (from nadir) ground coverage along with views to cold space and to on-board spectral and radiometric calibration sources every scan cycle. The scan cycle repeats every 8/3 seconds. Ninety ground footprints are observed each scan. One spectrum with all 2378 spectral samples is obtained for each footprint. A ground footprint is measured every 22.4 milliseconds. The AIRS spatial resolution is 13.5 km at nadir from the 705.3 km orbit. The AIRS is accompanied by two microwave sounders, the Advanced Microwave Sounding Unit-A (AMSU-A) and Humidity Sounder for Brazil (HSB). The microwave instruments are used to correct for cloud contamination in AIRS footprints. The HSB is essentially the same as the NOAA AMSU-B instrument without the 89 GHz channel. Details of the NOAA HIRS and AMSU-A and –B instruments can be found in [*Kidwell*, 1990]. Unfortunately, HSB malfunctioned in October 2002. The AMSU-A near-nadir footprint size is 42 km, and both AIRS and AMSU-A are co-registered such that there is a 3 x 3 array of AIRS footprints for each AMSU-A footprint. Fig. 2.1 shows the scanning geometry of AIRS and AMSU-A.

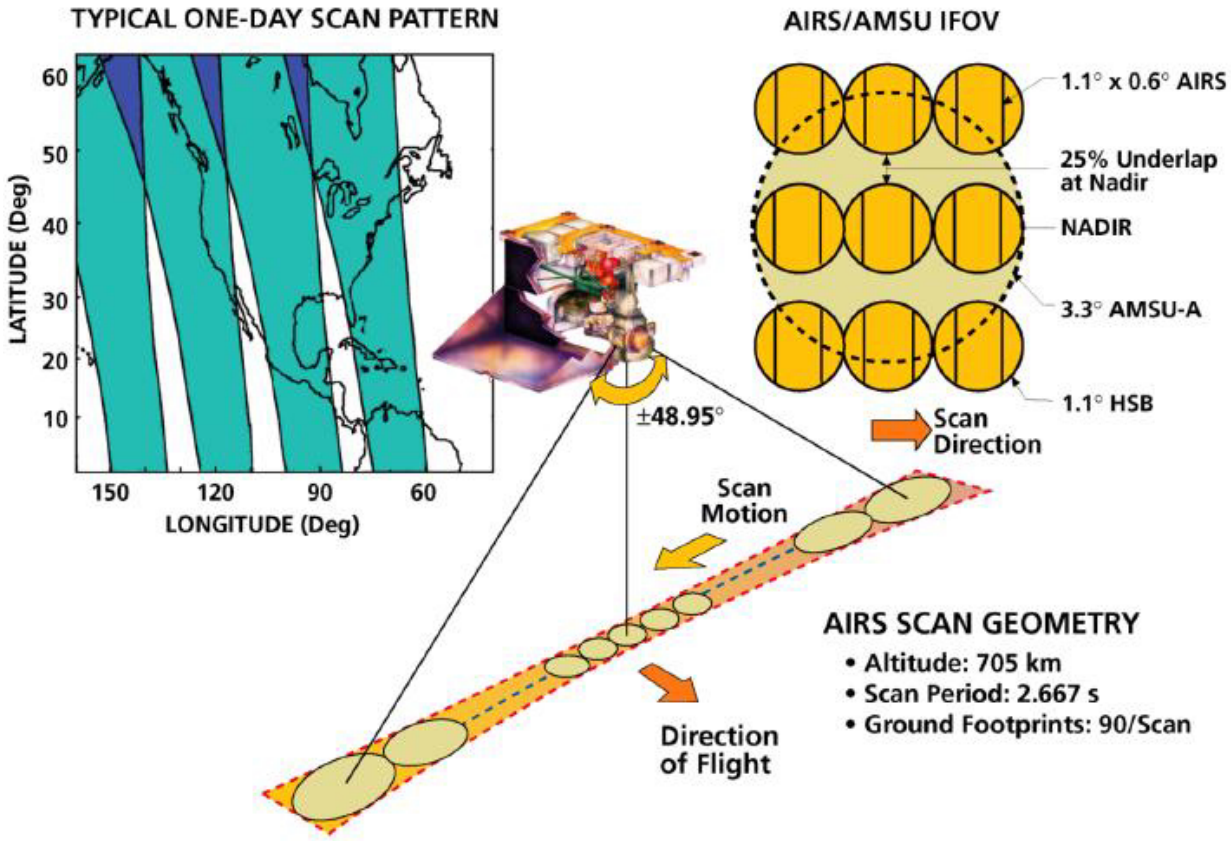

Fig. 2.1: Schematic of the AIRS and AMSU scan geometries

Fig. 2.2 is an example of the AIRS spectral coverage for a clear-sky middle latitude summer atmospheric atmosphere. Information that can be extracted from the measured clear-sky AIRS infrared spectra includes water vapor, temperature, and trace gases such as CO_2, CO, CH_4, and O_3.

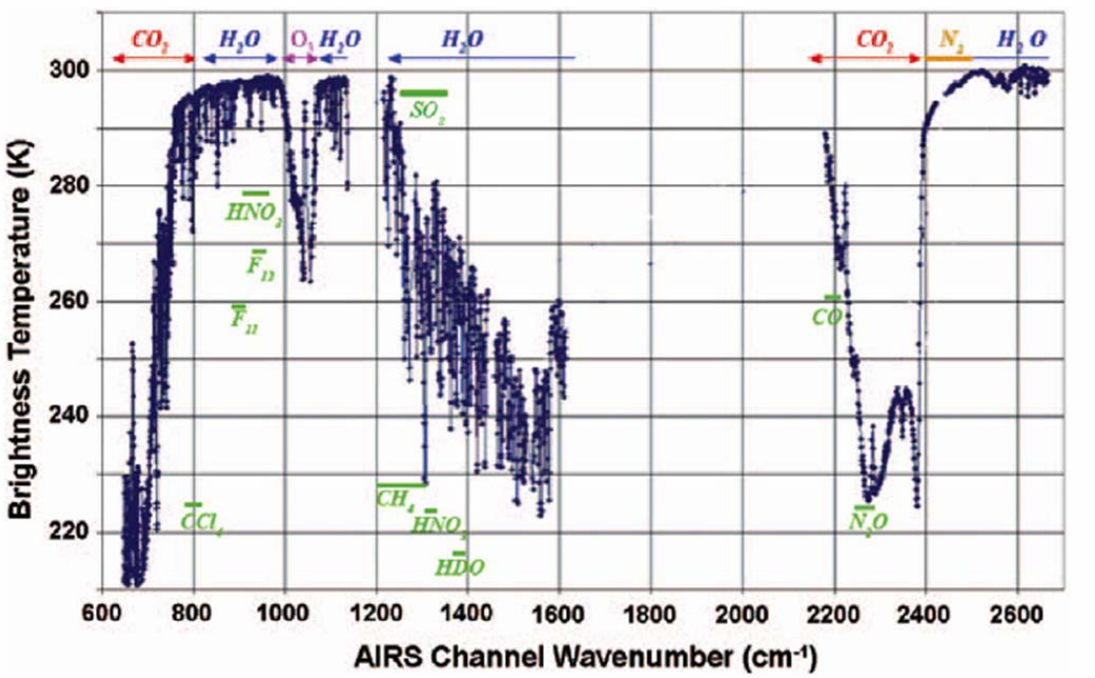

Fig. 2.2: Example of AIRS spectrum for a typical clear-sky middle latitude summer atmospheric condition. Also shown are the key absorbers of infrared radiances.

The radiometric accuracy and stability of AIRS radiances have been confirmed by a number of studies: 1) long-term comparisons of the AIRS 2616 cm-1 window channel, which has a maximum atmospheric contribution of 0.3 K, with daily measurements of sea surface temperature (SST) [*Aumann et al.,* 2006], 2) direct spectral radiance comparisons with aircraft observations [*Tobin et al.*, 2006], and 3) comparisons with brightness temperatures simulated from ECMWF analyses [*Strow et al.*, 2006]. These studies have confirmed that AIRS has exceptional radiometric performance, which includes low instrument noise, spectral response function stability, and long-term radiometric stability. Comparisons with SST and aircraft observations, shows a stability of .01 K per year and an absolute accuracy within 0.1 K, respectively. The instrumental noise of AIRS is shown in Fig. 2.3.

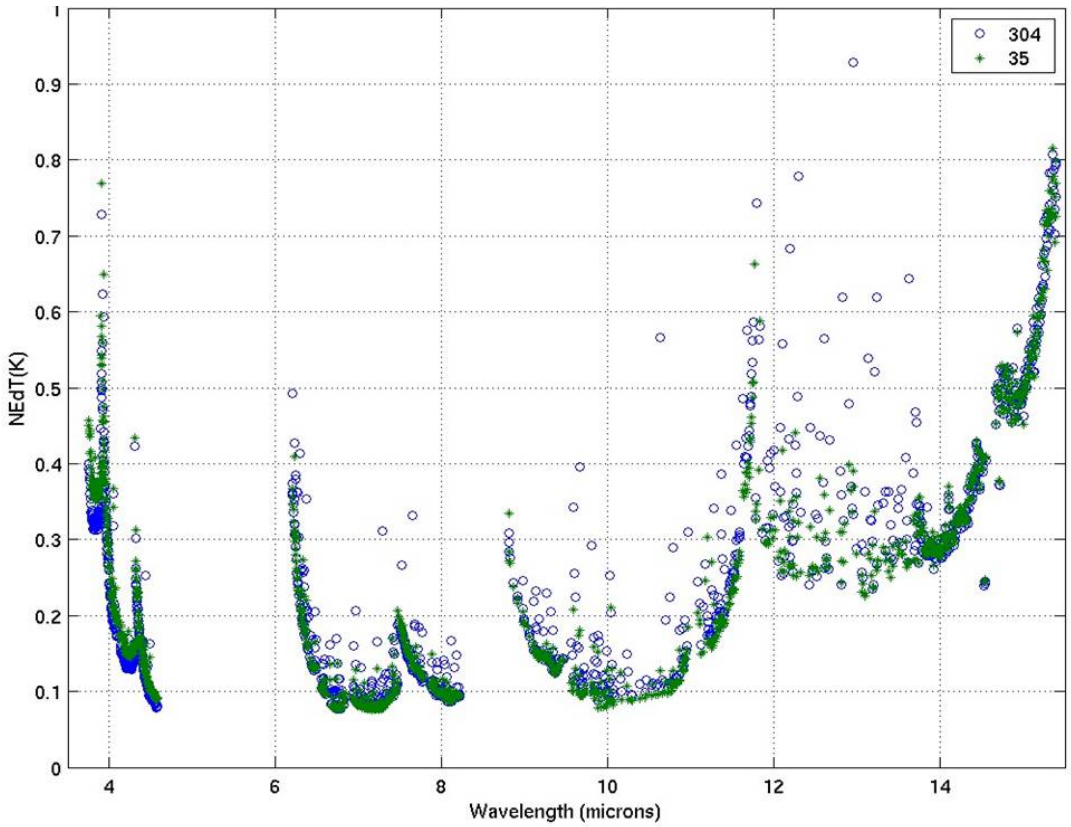

Fig. 2.3: AIRS instrumental noise at an equivalent temperature of 250 K

The AMSU-A consists of two separate modules, A1 and A2. The A1 component has 12 channels between 50 and 58 GHz in the oxygen band and an 89-GHz window channel. The A2 has two window channels at 23.8 and 31.4 GHz. The AMSU-A temperature sounding channels are used in the cloud clearing of AIRS partially cloud contaminated radiances (discussed in section 2.3) to derive cloud-cleared radiances.

2.2 Infrared Radiative Transfer

Infrared instrument in space are designed to measure the earth's outgoing infrared radiation at different wavenumbers υ and view angles θ. The measurements, R(υ,θ), can be expressed as the sum of four components:

$$\begin{aligned} R(\upsilon,\theta) &= R_s(\upsilon,\theta) \quad \text{(surface)} \\ &+ R_a(\upsilon,\theta) \quad \text{(atmospheric)} \\ &+ R_d(\upsilon,\theta) \quad \text{(downwelling)} \\ &+ R_\bullet(\upsilon,\theta) \quad \text{(reflected solar)} \end{aligned} \tag{2.1}$$

The surface component R_s is the emission from the surface radiance, averaged over the footprint, and attenuated by the atmosphere. The emission from the surface is also dependent on the surface emissivity ε and the surface temperature T_s. The surface component is given as

$$R_s(\upsilon,\theta) = \varepsilon(\upsilon,\theta)\, B(\upsilon,T_s)\tau(p_s,\upsilon,\theta) \tag{2.2}$$

Where τ is the transmittance evaluated at the surface pressure P_s , θ and υ, and B is the Planck Blackbody radiance evaluated at υ and T_s. The Planck radiance is given by

$$B(\nu,T) = c_1\nu^3 / [e^{c_2\nu/T} - 1] \tag{2.3}$$

Where $c_1 = 1.191044 \times 10^{-5}$ (mW/m2/ster/cm^{-4}), $c_2 = 1.438769$ (cm deg K), and T is temperature.

The derivation of transmittance will be shown shortly in more detail. The amount of attenuation by the atmospheric is given by $\tau(p_s, \upsilon, \theta)$. To simplify notation, $\tau_s = \tau(P_s, \upsilon, \theta)$ and $\varepsilon = \varepsilon(\upsilon, \theta)$. For measuring surface temperature from

satellites, the ideal case is when the τ_s and ε are both unity, hence the other terms are zero and the outgoing radiance measured by the satellite sensor is equivalent to the Planck blackbody temperature of the surface. There are frequencies, called window regions that approach this ideal situation. In the infrared region, windows occur between 800 to 1000 cm^{-1}, 1100- 1250 cm^{-1}, 2100-2150 cm^{-1}, and 2400 – 3000 cm^{-1}. The atmospheric contribution generally ranges between 0.5 and 2 Kelvin (K) for traditional window channels, but is larger for the shortwave infrared due to contamination by reflected solar radiation. Infrared surface emissivities are generally close to unity (> 0.95) except for deserts.

The atmospheric component R_a is the emission from the atmosphere. In the infrared region, where scattering of radiation is negligible, the radiation is simultaneously absorbed and emitted. Both absorption (k) and emission coefficients are assumed to be equal. Transmission through an absorbing medium (gas) for a given frequency is governed by the number of intervening absorbing molecules (path length u) and their absorbing power (k) at that wavelength. Beer's law indicates that transmittance decays exponentially with increasing path length, u(p)

$$\tau (p \rightarrow o) = e^{-k(\upsilon)\, u(p)} \qquad (2.4)$$

The path length is given by $u(p) = 1/g \int q(p)\, dp$, where g is gravity, q is the mixing ratio of the absorbing gas, and integral limits is from p_s to pressure at the top of the atmosphere (p=0). So if $\tau = 0.9$ at 500 mb, this means 90% of the outgoing radiation is coming from 500 mb and higher pressures; only 10% from the remaining upper atmosphere.

The atmospheric component is given by

$$R_a(\upsilon,\theta) = \int B(\upsilon,T(P))[d\tau(p, \upsilon, \theta)/ dp]\, dp \qquad (2.5)$$

where the integral limits is from p_s to pressure at the top of the atmosphere (p=0). The expression in the brackets is the vertical change of atmospheric transmittance with respect to the vertical change in atmospheric pressure, and is often called the weighting function (WF). Fig. 2.4 shows the weighting function for a lower stratospheric channel. The total area of the weighting function is unity. This weighting function shows that the largest contribution of the outgoing radiance is from approximately 90 mb. Note the shape of the weighting function; the contribution from 400 mb to the surface in negligible and the contribution above 10 mb is no larger than 5%. Observations from multiple channels can be combined using inversion techniques [*Rodgers*, 2000] to derive an atmospheric temperature profile (retrieval) that yields the observed radiance spectrum within the instrumental noise, when the profile is inserted in the radiative transfer solution of eq. (2.1). With one channel the retrieval is the observed brightness temperature which can be thought of as deep-layer mean temperature. The layer is defined by the weighting function. Numerous overlapping weighting functions are needed to derive an accurate vertically resolved temperature profile.

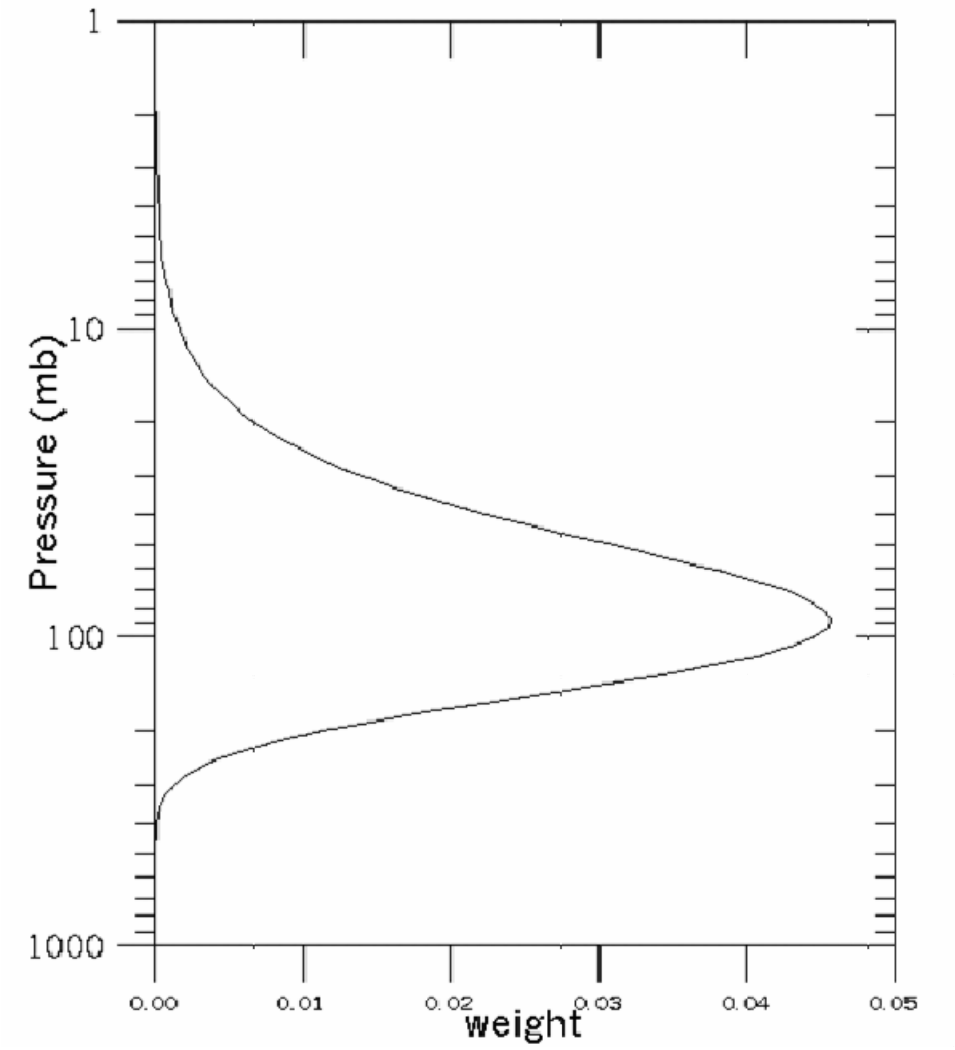

Fig. 2.4: Example of an atmospheric weighting function for a channel peaking near 90 mb.

The third term is the downwelling atmospheric radiation reflected by the surface and transmitted to space and is given by

$$R_d(\upsilon,\theta) = (1-\varepsilon)\,\tau_s\,[R_s(\upsilon,\theta) + R_a(\upsilon,\theta)] \qquad (2.6)$$

Typically this term is very small, since in the infrared the surface emissivity is generally near unity. It becomes negligible for atmospheric channels with relatively small surface contributions.

The last term is the downwelling radiation from the sun, reflected by the surface and transmitted to space, and is given by:

$$R_{\bullet}(\upsilon,\theta) = \rho H(\upsilon) \tau_s^2 \qquad (2.7)$$

The reflected solar component requires computation of the transmittance along the bi-directional path from the sun to the surface, and back to the spacecraft. *H* is the solar radiance outside the Earth's atmosphere. The solar surface reflectivity, ρ, is a function of surface type, zenith angle, solar zenith angle, azimuth angle, and wavenumber. This solar term is only significant for frequencies greater than 2400 cm^{-1}. Generally, channels affected by solar contaminated are not used during the day.

2.3 AIRS Science Objectives

The objective of the AIRS mission is to provide high precision and highly accurate spectrally resolved radiances for operational numerical weather forecasting and climate research. The much higher spectral resolving power of AIRS, with respect to heritage operational infrared sounders such as HIRS, is crucial for retrieving temperature and moisture soundings with vertical resolutions approaching 1 km, instead of the 3 to 5 km obtained from the heritage instrument. Assimilation of AIRS in weather prediction models have resulted in forecast improvements [*LeMarshall et al.,* 2006]. The higher vertical resolution is possible because AIRS can resolve individual absorption lines with high precision (low instrumental noise) resulting in sharper atmospheric weighting functions. In addition to sharper weighting functions, there are now many more channels. As noted earlier, AIRS has 2378 channels, the HIRS only 19. Low channel noise, large number of channels, and high spectral resolution results in higher vertical resolution of derived geophysical

parameters. The AIRS spectral coverage allows for the retrieval of temperature, water vapor, ozone, methane, carbon dioxide, carbon monoxide, and nitrous oxide from clear-sky observations. Fig. 2.5 shows a comparison of water vapor weighting functions from HIRS and AIRS.

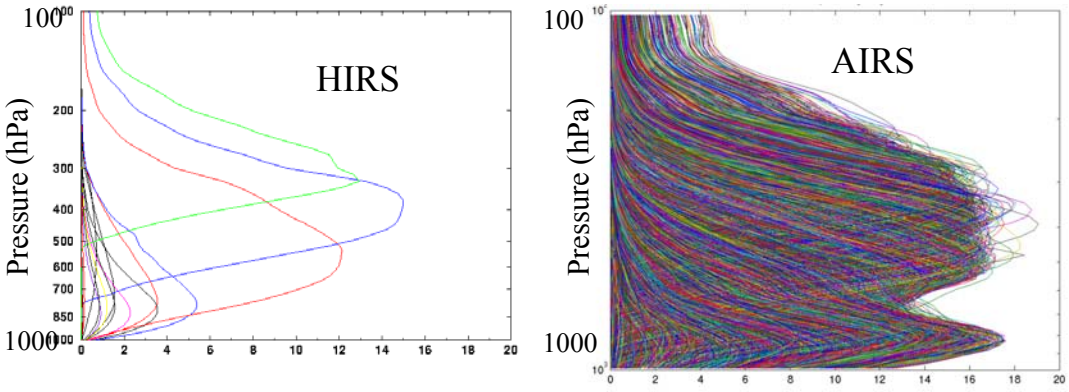

Fig. 2.5: HIRS and AIRS representative water vapor weighting functions

The AIRS/AMSU retrieval process includes an AMSU initial guess, cloud clearing, an Empirical Orthogonal Functions (EOF) regression guess [*Goldberg et al.* 2003], and a physical retrieval [*Susskind et al*. 2003]. The cloud clearing algorithm is a critical step since it increases the global percentage of clear-equivalent scenes from 5% to more than 50%. The cloud clearing algorithm is described in [*Susskind et al.,* 2003] Cloud-clearing begins with an AMSU physical retrieval [*Rosenkranz,* 2003] of atmospheric temperature, moisture (liquid and vapor), microwave spectral emissivity, and skin temperature. The AMSU retrieval, based on channels not sensitive to clouds, is used to compute an estimate of the AIRS radiances for the clear component of the scene. Cloud clearing assumes that the only difference between a set of AIRS footprints is the amount of clouds, therefore, the clear radiance estimate

can be used to retrieve a set of extrapolation parameters from a set of AIRS partially cloudy contaminated footprints. A set of 3 x 3 AIRS footprints, coaligned with the AMSU footprint, as was shown in Fig. 2.1, is used. Scenes are rejected when the cloud clearing assumptions fail; this generally occurs when a poor clear state estimate is used or the scenes are too cloudy. The extrapolation parameters for accepted scenes are then used to compute the cloud cleared radiances for any channel that is sensitive to clouds. Channels that are not sensitive to clouds are averaged over the nine footprints.

Fig. 2.6 shows the comparison of temperature and water vapor retrieval uncertainties, which I derived from the AIRS and the Advanced TIROS-N Operational Sounder (ATOVS) which in addition to HIRS also includes the Advanced Microwave Sounding Unit (AMSU). Note the large reduction in error for both temperature and water vapor. The vast number of relatively sharp AIRS water vapor channels (Fig. 2.5) results in a notable reduction in water vapor retrieval uncertainty. The retrieval algorithm is based on linear regression. I used an ensemble of 10,000 atmospheric temperature and water vapor profiles from radiosondes. I simulated AIRS, AIRS and AMSU brightness temperatures. I applied principal component analysis, described in much greater detail in Chapter 3, to the AIRS ensemble of spectra. The eigenvectors from the PCA are projected onto the spectra to produce principal component scores (PCS). Principal component regression simply uses principal component scores for predictors in least squares regression. For AIRS we use 60 principal component scores for predictors and solve for atmospheric temperature, moisture, ozone profiles and surface temperature and surface emissivity.

With 2000+ channels, many of the channels are similar to each other, making the

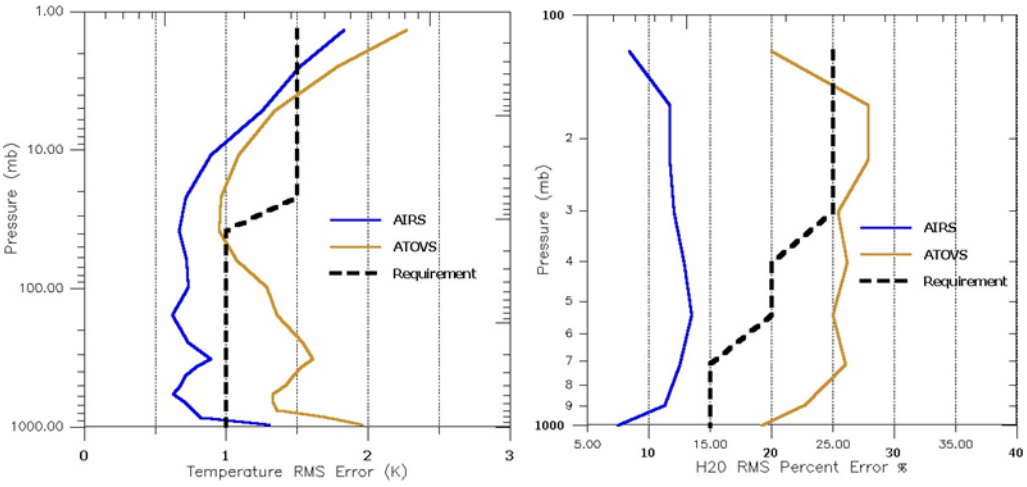

Fig. 2.6: Comparison of AIRS and ATOVS Root Mean Square Errors for temperature and water vapor using radiosonde soundings as truth.

covariance matrix nearly collinear. A significant advantage for using 60 principal component scores instead of all 2000+ channels is that the inverse of the predictor matrix is more stable and less collinear. Another advantage is that the regression solution is computationally fast. In matrix notation the form of the regression coefficients C, dimensioned *m* number of parameters by the *k* number of principal component scores, is

$$\mathbf{C} = \mathbf{XP^{*T}(P^{*}P^{*T})^{-1}} \qquad (2.8)$$

where **X** is a training dependent predict and ensemble matrix, of dimension *m* by sample size *s*. **P*,** the training predictor ensemble matrix of PCS, has dimension *k* by *S*. On independent data the *m*-dimension solution vector is obtained from the matrix multiplication of C **p***, where **p*** is the independent vector of principal component scores of length *k*. The ATOVS coefficients were derived without using PCA, since the total number of channels was only 34 (19 HIRS plus 15 AMSU).

The AIRS provides traditional retrievals of atmospheric temperature, water vapor, ozone, cloud amount and cloud height, as well as new research products of greenhouse gas and aerosols. Fig. 2.7 shows the sensitivity of the AIRS radiances to a 0.5% change in CO_2, CH_4, CO, O_3, and H_2O a given trace gases profile. The sensitivity in brightness temperature is relatively small, generally within 0.06 K. As shown in Fig 2.8, between 1984 and 2004 20 years, CO_2 concentrations have increased by about 10%. The equivalent radiance signal in brightness temperature during this period, particularly near 725 cm-1, should have been approximately 1 K. From 2002 to 2006, the change of brightness temperature in AIRS channels most sensitive to CO_2 was found to be about 0.2 K (Strow, private communication).

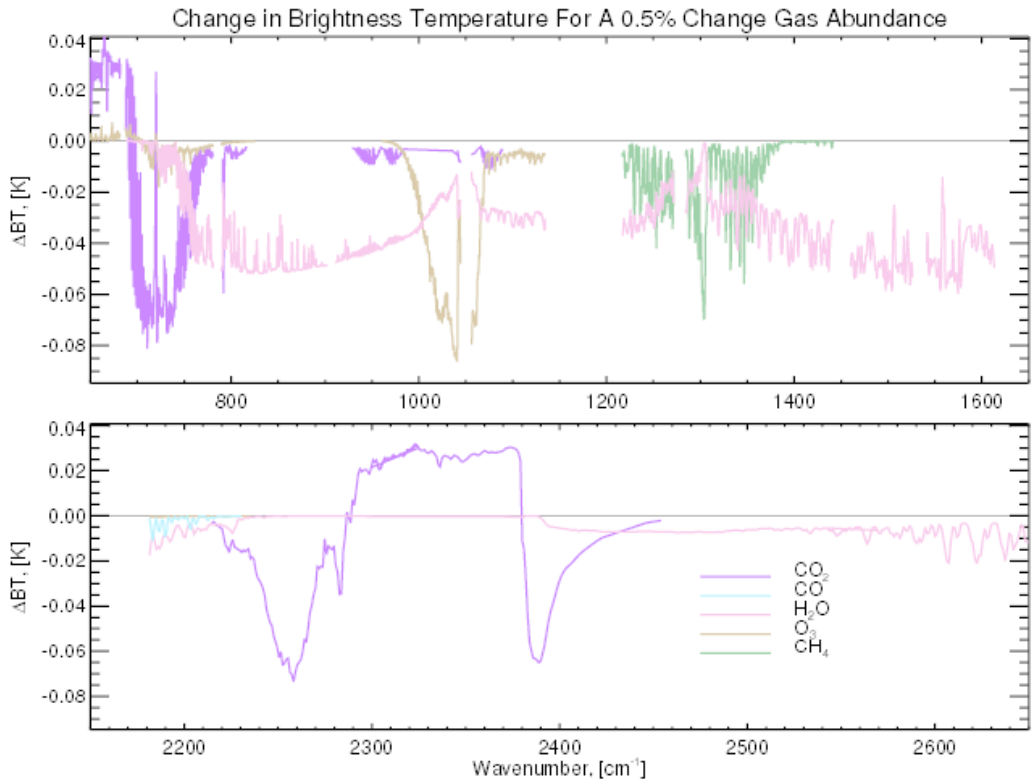

Fig. 2.7: Sensitivity of AIRS radiances due to a 0.5% increase in a given trace gas profile.

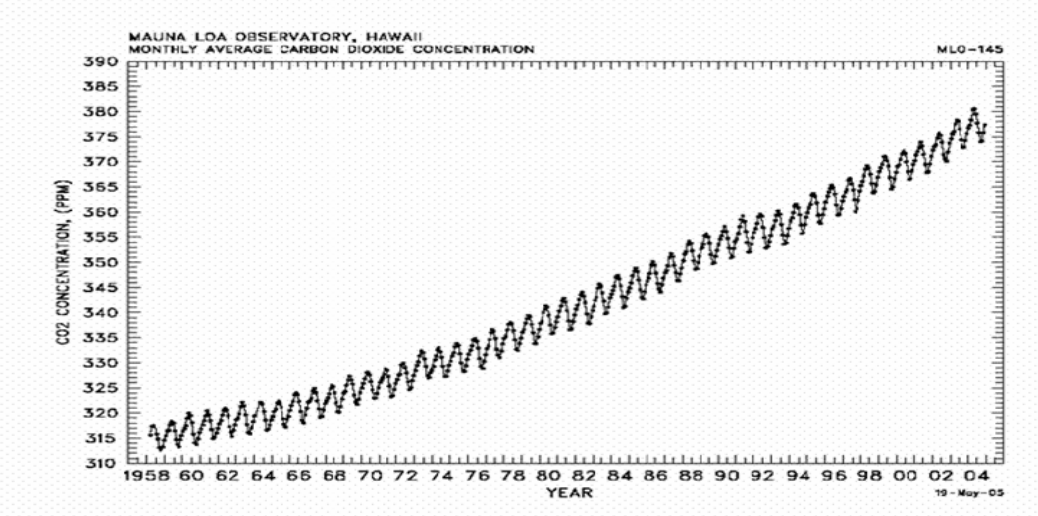

Fig. 2.8: CO_2 concentration at Mauna Loa as a function of time

Deriving accurate greenhouse gas measurements requires not only high spectral resolution and excellent noise performance, but also accurate background states for temperature and water vapor *(Chahine et al.*, [2006]). As shown in Fig 2.7, AIRS channels sensitive to CO_2, particularly near 725 cm-1, are also sensitive to H_2O. *Engelen and McNally,* [2005] use the ECMWF model analysis to provide the background state of temperature and water vapor. The core AIRS algorithm derives the background state, including ozone, by avoiding channels that are overly sensitive to the other trace gases, primarily CO_2, CO, and CH_4. [*Maddy et al*., 2008]. The trace gases are then derived by iterating the physical retrieval with the trace gas channel set. CO_2 is primarily retrieved from AIRS spectral radiances in the 712-750

cm-1 region. However, since temperature and CO_2 are strongly coupled, retrievals must be done carefully. The temperature profile is first solved with a CO_2 error covariance term, which makes the temperature retrieval very insensitive to the CO_2 background climatology. The temperature profile is solved with CO2 in the wings of the CO_2 lines. After water vapor and ozone are retrieved, the total column CO_2 is solved using the CO_2 line centers. Comparisons with NOAA's Earth System Research Laboratory (ERSL) aircraft flask measurements of carbon dioxide yield a standard deviation with collocated AIRS CO_2 of approximately 1.8 parts per million (ppm) or about 0.5% [*Maddy et al*., 2008]. Tropospheric carbon monoxide CO abundance is retrieved from the 2180-2230 cm-1 region of the IR spectrum. CO is the direct product from the combustion of fossil fuel and biomass burning and that it has a role as a smog and tropospheric ozone precursor. As shown in Fig. 2.9, extremely high CO concentrations result from biomass burning in central South America, Africa, and Indonesia, with significant transport to the South Atlantic and Indian Oceans. Validation by *McMillan et al.* [2005] against aircraft observations indicates that AIRS CO retrievals have an accuracy of about 15%.

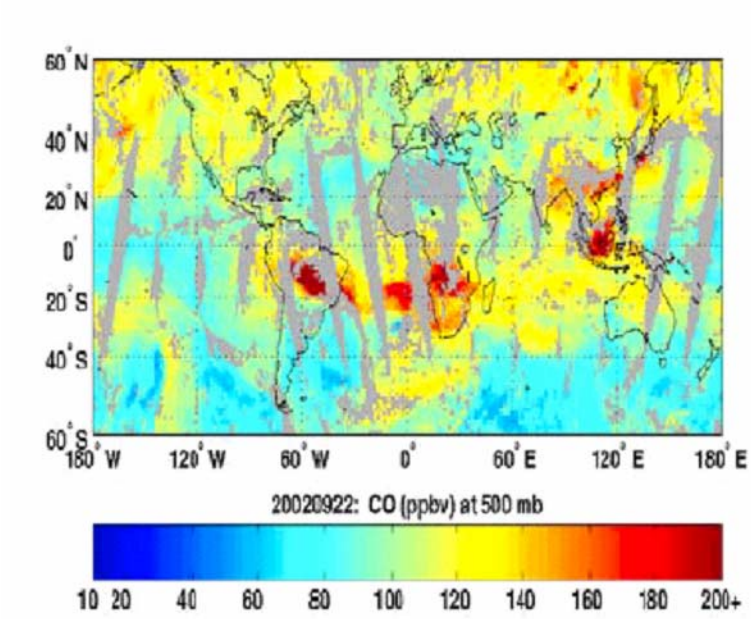

Fig. 2.9: AIRS CO for September 29, 2002 shows biomass burning in South America, Africa and Indonesia

AIRS measures approximately 200 channels in the absorption band of CH_4, centered near 1305 cm-1, of which 71 channels are used to retrieve CH_4. The retrieval algorithm of CH_4 is described in [Xiong et al., 2008]. ERSL aircraft flask measurements also include CH_4; comparisons with AIRS CH_4 result in a standard deviation of 1.5%.

AIRS can also detect atmospheric aerosols. The absorption of silicate aerosols peaks in the 900-1100 cm-1 region while both ice and aerosols show minimal absorption around at 1232 cm-1 [*Volz*, 1973],. The brightness temperature difference between AIRS radiances at 961 and 1232 cm–1 (*DeSouza-Machado et al.* 2006) has been used to provide global maps of brightness temperature sensitivity to aerosols. Aerosols are detected when the negative differences are less than -0.25 K, and large events are noted when the negative differences are less than -2.0 K. AIRS

spectra have been used to observe the total column of sulfur dioxide (SO_2) injected into the atmosphere during a volcanic event, by a simple difference of two channels which have similar measurements when there is no SO2. The AIRS channels used for detecting SO_2 are at 1258.90 cm-1 and at 1354.10 cm-1. Both channels have similarly sensitivity to water vapor, but only the 1354.10 cm-1 channel is sensitive to large amounts of SO_2.

2.4 Applications of spectrally resolved radiances

Observations from satellite instruments have been used to estimate climate change and variability. One of the most widely used satellite instruments for monitoring tropospheric temperature change is the Microwave Sounding Unit (MSU). *Spencer and Christy* [1993] pioneered the first temperature time series from MSU channel 2. This channel's weighting function peaks near 600 mb, similar in shape to Fig. 2.4. The series of MSU instruments operated from 1979 to 2006, and today these types of measurements are continued by the Advanced Microwave Sounding Unit (AMSU). Twelve different MSU instruments over the course of nearly 20 years were used to generate the time series. The unique attribute of the MSU is its very stable spectral response function (SRF), the wavelength interval over which the radiation is measured. The MSU's SRFs are boxcar functions over the bandpass (values of unity within the bandpass, zeros outside). Identical bandpasses were designed for each MSU were used. However there were still systematic biases between coincident measurements from different instruments, due to time variant errors in the instrument's warm target used in the calibration process. A number of investigators,

[*Christy et al.*, 2000, *Mears et al.*, 2003, *Vinnokov and Grody*, 2003; and *Zou et al.*, 2006] applied different techniques to correct for the warm target anomaly. Each approach resulted in different trend estimates ranging from 0.05 C per decade to 0.20 C per decade. The MSU cannot be considered as a climate benchmark instrument, since benchmark (i.e. irrefutable) measurements cannot be obtained. In other words, the results will always be questionable. The HIRS instrument, which flew on the same satellites as the MSU, is not often cited for monitoring climate change. The problem in generating time series from the HIRS instruments is their varying instrument dependent SRFs, shown in Fig. 2.10. Hence the information content from the different instruments varies, which adds complexity in constructing a stable time series. Furthermore, dominant component of the bias is due to real differences between the SRFs. These cause differences in weighting function shapes, leading to profile dependent differences in brightness temperatures that are much more difficult to correct for.

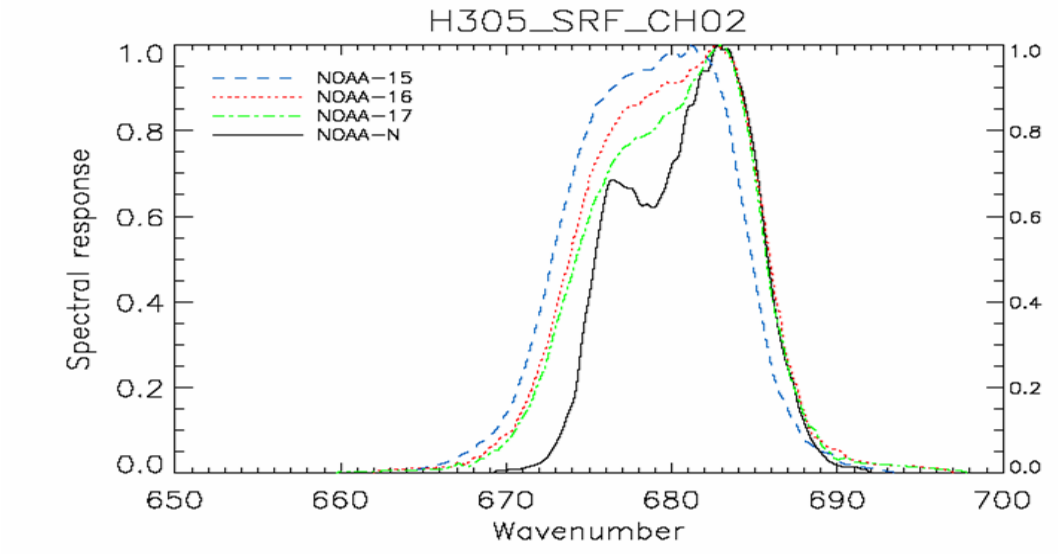

Fig. 2.10: Four different HIRS channel 2 spectral response functions associated with different satellites – NOAA-15,-16,-17, and –N.

Even a perfect MSU time series has limited applications for understanding climate change. The MSU can detect trends, but the trend is for a vertically integrated temperature profile weighted by the MSU weighting function. One does not know the vertical distribution of the trend within the integration layer which is about 10 km thick. Spectrally resolved infrared radiances provide the opportunity not only to detect climate change but also to understand the processes contributing to climate change. Fig. 2.11 shows, at high spectral resolution, the atmospheric absorption spectrum and comparative black body curves. If the earth was devoid of an atmosphere, the outgoing radiance for a surface temperature of 300 K would be the top curve in the figure. Fortunately, the Earth has a very rich atmosphere with many important constituents including CO_2, CH_4, H_2O, CO, N_2O and O_3. The infrared region is affected by these trace gases, and the spectrum shown in the figure is due to the absorption outgoing infrared radiation by these gases. The surface temperature used in computing the radiances is 295 K. For example the large valley in the curve between 9 and 10 um is due to ozone; as ozone increases the amount of absorption increases. Fig. 2.11 shows the radiance spectrum, but this can easily be converted to the brightness temperature of Fig. 2.12 by using the inverse of Planck's equation. In this figure, we can easily see the window channels which have brightness temperatures close to the surface temperature of 295 K. Even in these window regions there is some absorption, primarily due to water vapor. We can see large absorption due to water vapor near the center of the spectrum. Between 600 and 800 cm^{-1} and 2200 and 2400 cm^{-1}, the absorption is primarily due to CO_2.

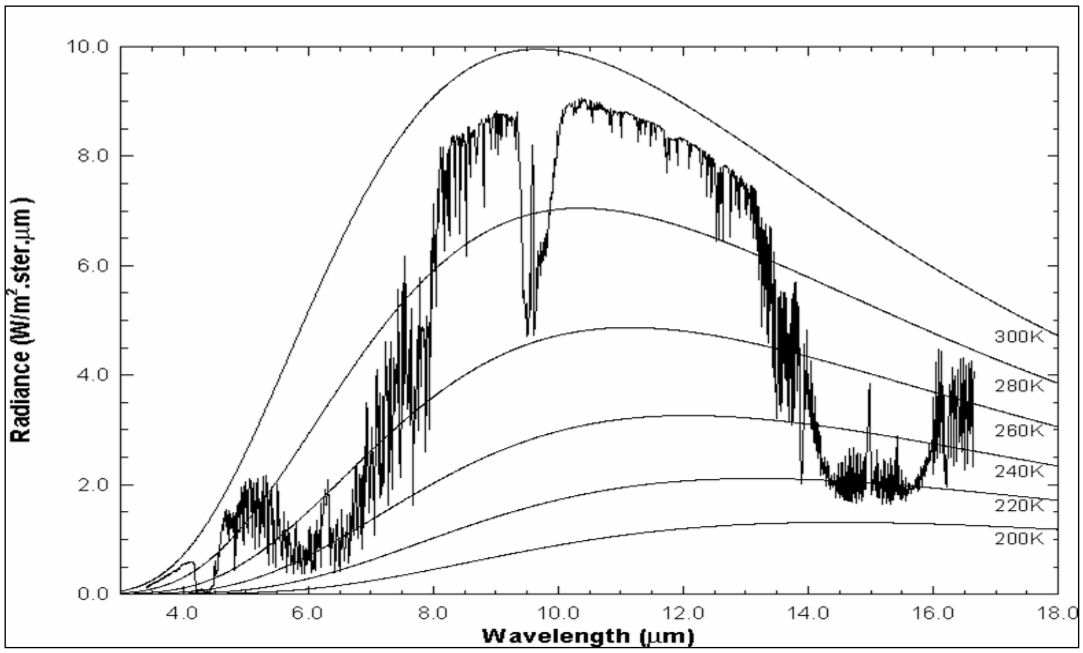

Fig. 2.11: High resolution atmospheric absorption spectrum and comparative blackbody curves

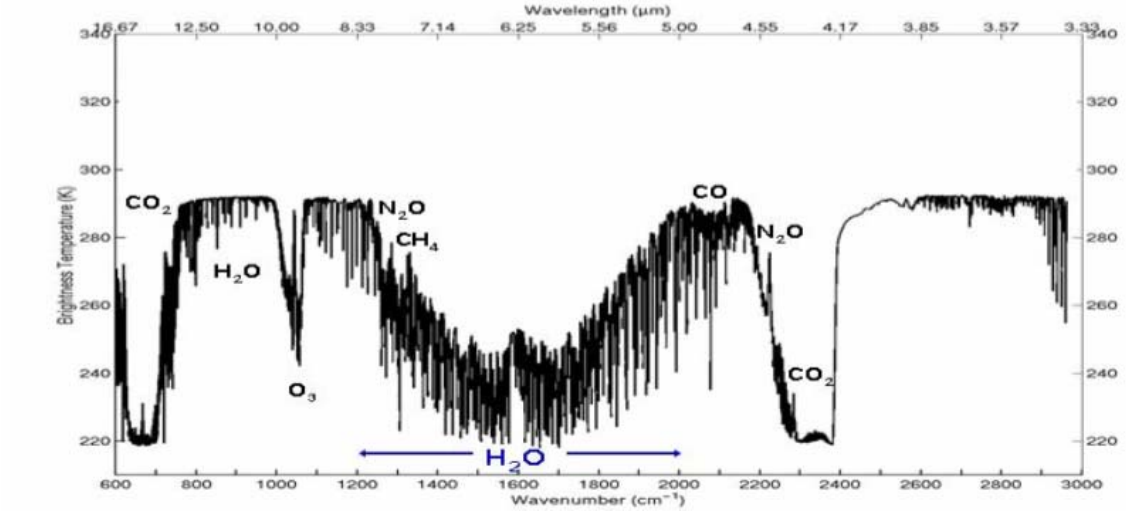

Fig. 2.12: Infrared spectrum in brightness temperature for summer midlatitude atmosphere

The brightness temperatures are related to the height in the atmosphere. For example the low brightness temperatures in the water vapor region (centered at 1600 cm^{-1}) correspond to upper tropospheric water vapor absorption, while the higher brightness temperatures are associated with middle and lower tropospheric water vapor absorption. The decrease of brightness temperature from 800 cm^{-1} to 667 cm^{-1} is associated with observing temperature higher and higher into the atmosphere. The increase of brightness temperatures near 667 cm^{-1} is due to observing temperature in the warmer stratosphere.

The advantage of high spectral resolution infrared observations is that we can start to understand the contributions to changes in climate. For example, outgoing longwave radiation (which is the spectral integration of the infrared region) is often used to monitor climate change, but it has limited use because of difficulties in determining the cause of the change. Is it due to changes in clouds, temperature, water vapor, carbon compounds, ozone, etc? However with spectrally resolved radiance we will be able to start dissecting and understanding the root causes of observed changes. We can also use spectrally resolved radiances to validate weather and climate models, by simply comparing the observed spectra with those calculated from the model's geophysical parameters.

Chapter 3: Generating the High Quality Spectrally Resolved Infrared Radiance (SRIR) Dataset

3.1 Overview

The SRIR datasets are generated by the following steps: 1) The AIRS observations are screened for outliers, 2) the observations are converted to brightness temperatures and mapped into ascending and descending daily brightness temperature (BT) gridded datasets, 3) the observations within the gridded datasets are converted to principal component scores and stored in principal component (PC) gridded datasets, 4) the PC grids are adjusted for viewing angle (limb darkening) and stored in angle adjusted PC (AAPC) gridded datasets, 5) angle adjusted brightness temperatures are computed from the AAPC datasets and stored in the angle adjusted brightness temperature (AABT) gridded datasets and 6) the BT and AABT daily datasets are screened for clear sky values and averaged to produce monthly clear sky and all sky datasets. Each daily grid box contains only the first AIRS field of view (all channels) to observe that box that day for ascending and descending orbits. Ascending and descending refers to orbiting direction of the satellite. As the satellite ascends (~southeast to northwest direction), due to its inclination angle, it does so during the daytime side of the Earth. Likewise when it descends it does so during the nighttime side. The AQUA satellite crosses the equator at 13:30 local time when it ascends, and 12 hours later when it descends. By keeping the data separated into ascending and descending, the radiance climatology can be used to look at daytime and nighttime differences and trends.

The SRIR climatology consists of monthly brightness temperature datasets of two types – at the original viewing angle and adjusted for viewing angle to a nadir view - for the period 2003 – 2006 for:

1. Ascending (day), clear sky
2. Ascending, all sky
3. Descending (night), clear sky
4. Descending, all sky datasets

The spatial resolution is 2.0 degree latitude by 0.5 degree longitude. The monthly averaging of the original viewing angle is only for diagnostic purposes.

In a separate process, geophysical parameters from the NCEP and ECMWF atmospheric model analyses are interpolated to the same AIRS gridpoints inserted into SARTA to simulate daily clear sky brightness temperature grids. The simulated datasets are used to demonstrate how the SRIR datasets can be applied to the validation of weather and climate models. This chapter describes the algorithms and steps needed to generate the SRIR AIRS climatology.

3.2 Data Screening

Some of the AIRS HgTeCd detectors suffer from a phenomenon described as "popping" in which the detector has a non-Gaussian noise event that can be many times larger than the normal instrumental noise. The occurrence of "popping" for any arbitrary channel is about once every 10,000,000 measurements. I have developed a technique using principal component analysis (PCA) to screen for such erroneous AIRS data and to independently assess AIRS instrument performance. I also used

PCA to develop the AIRS Science Team statistical regression algorithm used for deriving atmospheric temperature, moisture, ozone and surface temperature and emissivity, and to angle adjust AIRS data. PCA, also referred to as eigenvector decomposition, is generally used to approximate data vectors having many elements (e.g. AIRS observations of 2000+ channels) with a new set of data vectors having fewer elements, while retaining most of the variability and information of the original data. The new data vectors are called principal component score vectors, and because they consist of the components of the original data vector in an orthogonal coordinate system, the elements of a given principal component score vector are independent of each other (unlike the original spectrum). Principal component analysis has been used in sounding applications as described in *Wark and Fleming*, [1966]; *Smith and Woolf*, [1976] , and for high spectral resolution infrared sounders by *Huang and Antonelli,* [2001], and *Goldberg et al.* [2003]. Elements of a principal component score vector are projections of the spectrum onto each of the orthogonal basis vectors, which are the eigenvectors (principal components) of the radiance covariance matrix. The total number, *n*, of eigenvectors is equal to the total number of channels. However, it will be shown that a much smaller set of *k* eigenvectors (< 100), ordered from largest to smallest eigenvalues, is sufficient to explain most of the variance in the original spectra. The covariance matrix is derived from an ensemble of AIRS normalized spectra, i.e. radiance divided by the instrument noise. The matrix of eigenvectors, **E,** is related to the covariance matrix, **S**, by:

$$\mathbf{S} = \mathbf{E}\,\Lambda\,\mathbf{E}^{T} \tag{3.1}$$

where **S**, **E** and Λ are all dimensioned *n* x *n*, and Λ is a diagonal matrix of eigenvalues. The principal component scores vector **p** is computed from:

$$\mathbf{p} = \mathbf{E}^{T}\,\mathbf{r} \tag{3.2}$$

where **r** is the vector of centered (departure from the mean) normalized radiances. The next equation is used to reconstruct the radiances from a truncated set of *k* eigenvectors E***** and a vector of principal component scores **p***. (The symbol * indicated that the matrix or the result of a matrix operation is due to truncated set of vectors.)

$$\mathbf{r^*} = \mathbf{E^*p^*} \tag{3.3}$$

The normalized reconstructed radiance vector is **r***, E***** has dimension *n* x *k*, and the vector **p*** has length *k*. To obtain the un-scaled radiance, one must add the ensemble mean normalized radiance used in generating the covariance matrix and multiply the sum by the noise used in constructing the normalized radiances.

The square root of the eigenvalues is equivalent to the standard deviation of the principal component scores of the dependent ensemble. Since we are using normalized radiances, the square root of the eigenvalues can be interpreted as signal to noise. Principal component scores can be thought of as super channels since each one is a linear combination of all channels. The first score contains the largest signal

to noise ratio, which as shown in Table 3.1 is very large. When the eigenvalues fall below unity, the noise has larger contribution than the signal. By using a truncated set of eigenvectors much of the noise in the original measurement can be removed.

Table 3.1 First Seventy Two Square Root of the Covariance Matrix Eigenvalues

1 7497.60	19 14.68	37 3.38	55 1.25
2 1670.40	20 13.49	38 3.11	56 1.19
3 945.52	21 12.28	39 2.82	57 1.16
4 496.01	22 11.32	40 2.53	58 1.15
5 284.01	23 10.70	41 2.41	59 1.09
6 266.30	24 9.08	42 2.39	60 1.05
7 156.95	25 8.24	43 2.34	61 1.02
8 139.67	26 7.85	44 2.24	62 0.98
9 88.27	27 6.77	45 2.03	63 0.90
10 72.83	28 5.98	46 1.86	64 0.86
11 60.03	29 5.83	47 1.78	65 0.81
12 53.42	30 5.39	48 1.71	66 0.80
13 45.01	31 5.34	49 1.65	67 0.78
14 39.72	32 4.98	50 1.61	68 0.77
15 34.54	33 4.34	51 1.54	69 0.73
16 26.57	34 4.09	52 1.52	70 0.72
17 22.62	35 3.62	53 1.35	71 0.70
18 17.60	36 3.48	54 1.34	72 0.66

An overall measure of how well the principal component scores can reconstruct the original data is provided by the reconstruction score (RS) that is defined as

$$RS = \left[1/N \sum_{i=1}^{N} (O_i - R_i)^2 \right]^{1/2} \qquad (3.4)$$

where O and R are the noise scaled observed and reconstructed radiances, respectively, for the i^{th} channel and N is the total number of channels used in the principal component analysis. A reconstruction score of less than one indicates that

the root measure square (rms) difference over the number of reconstructed channels is within the noise level. Large reconstruction scores also can be used to identify suspicious data. Fig. 3.1a-b shows the RS as a function of eigenvector; Fig. 3.1b is an expanded view of Fig. 3.1a. Here we see that unity is reached near the 60th eigenvector. One can either examine the eigenvalues or RS to estimate the number of principal component scores needed to reconstruct the radiances to the noise-level. However another important consideration for determining the appropriate number of eigenvectors is to examine the spatial patterns of the coefficients of the eigenvectors (i.e. the principal component score). Fig. 3.2 a-d show global maps of the 60th, 100th, 125th and 150th PCS. Even though the information obtained from Fig 3.1 a-b would suggest 60 PCS is adequate, the plots provide a different assessment. The eigenvector domain representing noise should associate with PCS spatial patterns with no apparent spatial patterns. We see in Fig. 3.2 a-d, the spatial patterns do not become negligible until the 150th PCS. Therefore one should use at least 150 PCS, and I selected 200 PCS to be conservative.

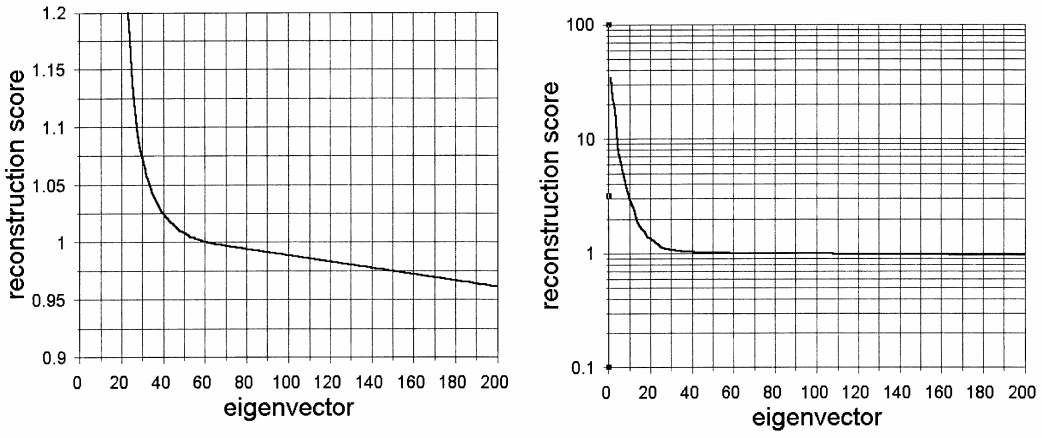

Fig. 3.1a-b: Reconstruction score as a function of the number of eigenvectors

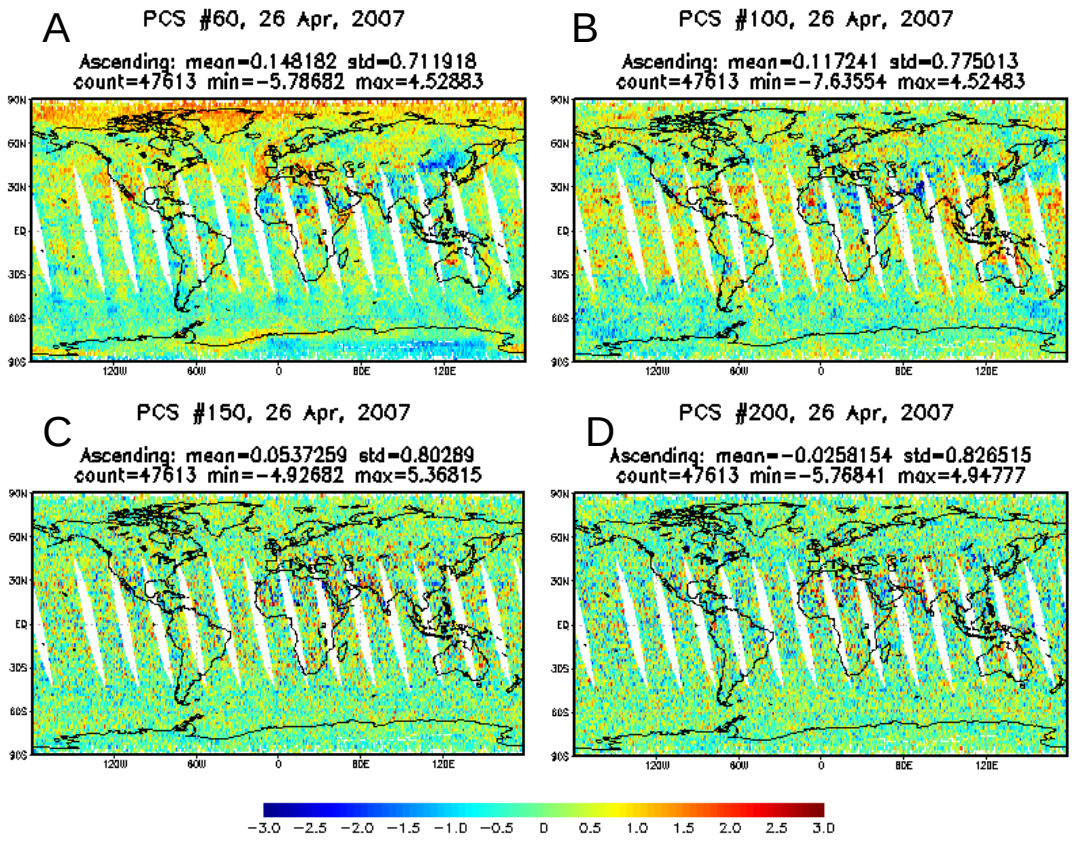

Fig. 3.2a-d Global maps of principal component scores for the 60th (A), 100th (B), 150th (C) and 200th (D) eigenvectors.

Reconstructed radiances are compared with original radiances to determine the quality of the original radiances. If the difference between the original radiance and the recomputed radiances is greater than twice the expected instrumental noise, the observed radiance is not selected. Fig. 3.3 shows the result of this screening method to remove outliers. The red curve is the expected instrumental noise, the green is the rms of the observed minus reconstructed radiances for a single day. Large departures from the red curve denote channels with significant anomalies.

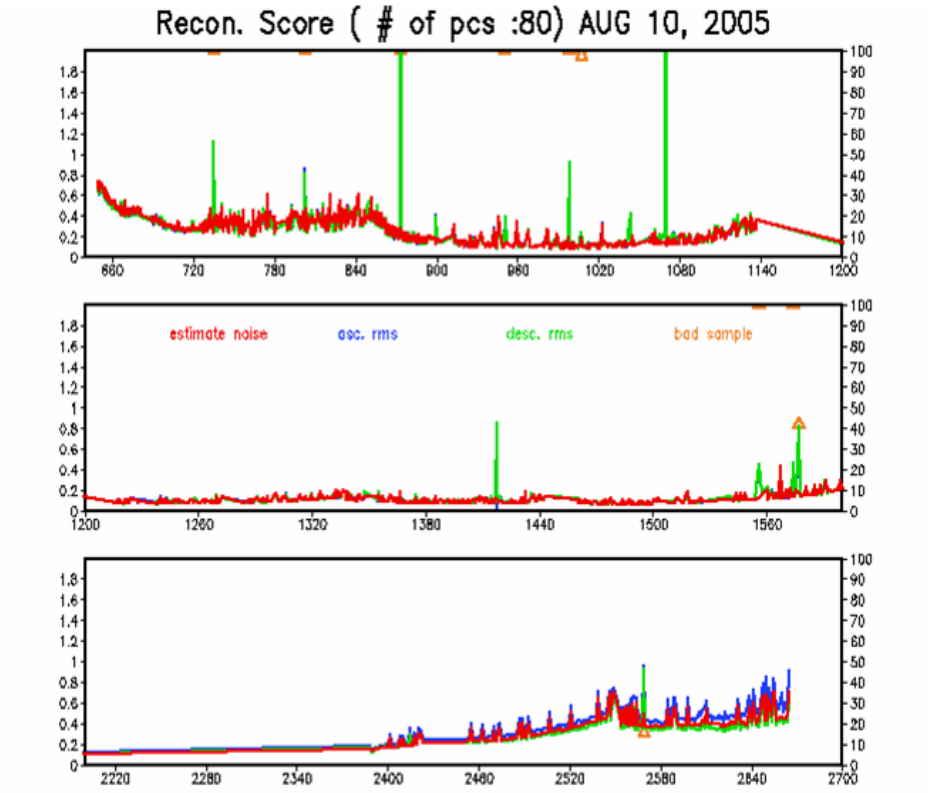

Fig. 3.3: Root Mean Square (rms) of reconstructed radiance (green curve) compared with the instrument calibration noise (red curve) as a function of channel in wavenumbers cm^{-1}.

Another important application of PCA is data compression. For example one can distribute to users 200 principal component scores instead of 2378 channels, and directly use the principal component scores in a retrieval algorithm instead of the individual channels [*Goldberg et al.*, 2003]. In this research project, the principal component scores will be used as predictors for the angle adjustment of the AIRS radiances.

3.3 Mapping

The data are gridded into a 2 x 0.5 degree latitude/longitude projection, separately for ascending and descending orbits. I originally was going to use a 1 x 1

latitude/longitude projection. I selected the 2 x 0.5 grid cell size because I wanted to have contiguous horizontal grid boxes populated from the same scan line to better study and correct for the effect of viewing geometry. The inclination angle of AIRS results in a latitude displacement of greater than 1 degree over a scanline. A 2 degree latitude dimension, particularly between +- 50 degrees latitude allowed for individual scanlines to populate contiguous horizontal grid boxes.

3.4 Angle Adjustment

Since AIRS is a cross-track scanning sensor, the radiances from the different view angles need to be limb adjusted to a fixed angle (e.g. nadir). As the instrument scans from nadir, the absorbing path also increases which results in an increase in height of the peak of the weighting function. The AIRS observations must be angle adjusted in order to average them; otherwise the averaging procedure would average radiances representing different absorbing path lengths. The basis of limb adjustment is that the brightness temperature for a given channel near nadir has a weighting function that is similar to the weighting function of a nearby channel at a different view angle [*Goldberg et al.,* 2001]. Limb adjustment provides the optimal combination of channels to yield a channel radiance that appears to be independent of scan position and only dependent on airmass. Fig. 3.4 shows a comparison of the original and limb-adjusted brightness temperatures for AMSU channel 5 on AQUA. Only the limb-adjusted data can be averaged to derive a radiance climatology.

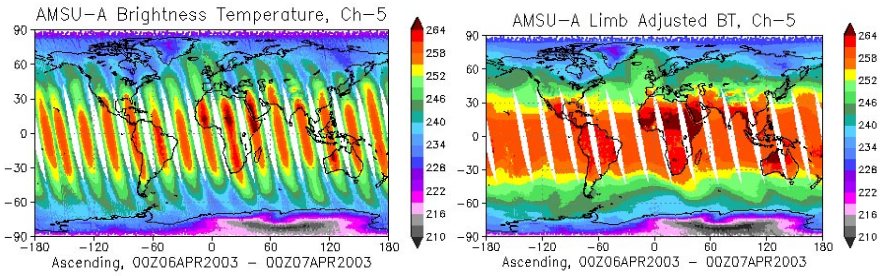

Fig. 3.4: Observed and limb adjusted brightness temperatures for AMSU channel 5

The AIRS limb adjustment methodology is based on the AMSU approach with the exception that the limb adjustment is performed by principal component analysis. Specifically we limb adjust the first 200 principal component scores and then reconstruct the limb adjusted radiances from the limb adjusted principal component score. The predictors for limb adjusting a given principal component score for an off-nadir position to a nadir value is the given principal component score plus the first six principal component scores. Linear regression is used to generate the predictor coefficients. The left panel of Fig. 3.5 shows an image of the original AIRS radiances and the limb adjusted radiances for an ozone channel. Note the limb effect in the lower image. On the right panel of Fig. 3.5, we show the monthly averaged field. Again the lower image is the original data without any limb adjustment. Note the signal is not nearly as intense as the upper image, because the limb effect was not accounted for.

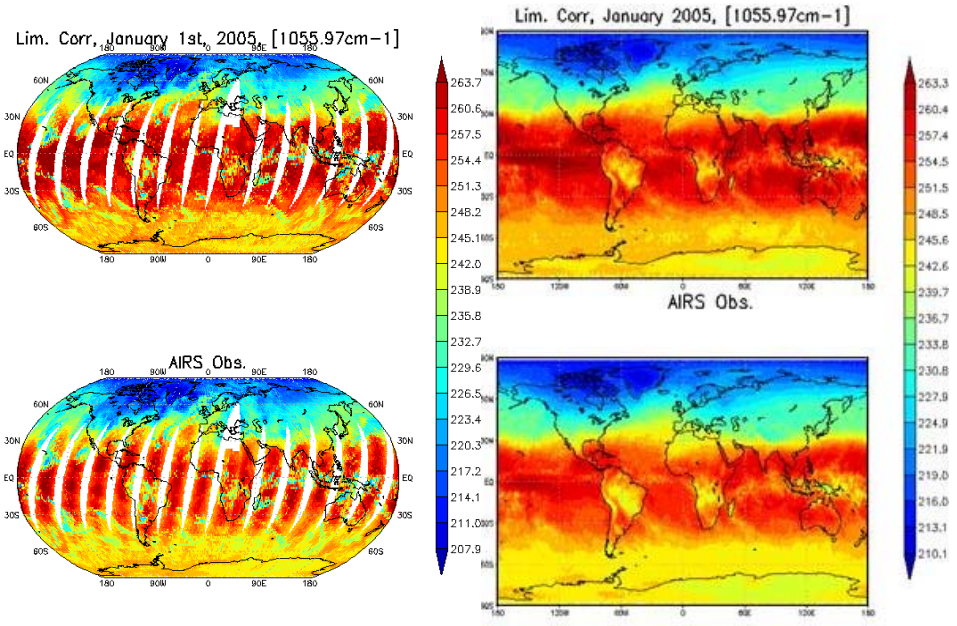

Fig. 3.5: Limb corrected (upper left) and original observed (lower left) AIRS radiance; monthly averaged limb corrected (upper right) and original (lower right) AIRS radiance

The SRIR datasets will allow the generation of difference fields for various time periods and regions. Fig. 3.6 shows the expected change in radiances due to changes in the state field. For example, in this figure one can see that a 15% increase in ozone results in a brightness temperature reduction of approximately 2 K, and a 15% increase in water vapor causes a reduction of approximately 1.25 K.

3.5 Radiance Simulations

The AIRS radiances are simulated using the AIRS radiative transfer forward model, SARTA. Required input is the temperature, water vapor and ozone profile at 100 atmospheric levels. Climatological values are used for CO_2, CH_4, and CO. All other gases are assumed fixed. SARTA has been validated by comparing the observed AIRS spectra with those simulated from near temporal and spatial time

coincidence high accurate in-situ observations from the Department of Energy (DOE) Atmospheric Radiation Monitoring (ARM) sites in the Tropical Western Pacific (TWP).

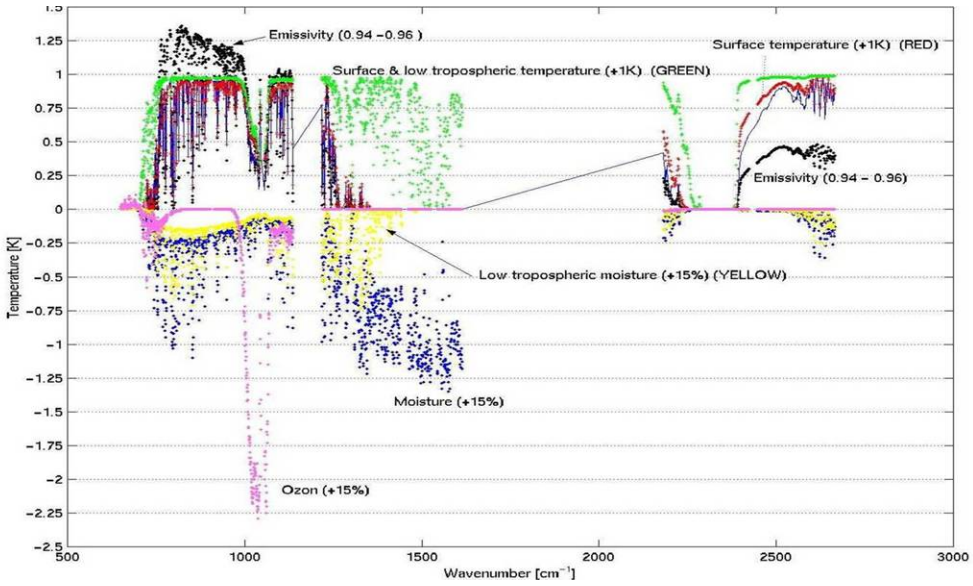

Fig. 3.6: Response in brightness temperatures due to a change in atmospheric and surface parameters

Fig. 3.7 shows the time averaged bias between observed AIRS and those computed from TWP under clear-sky conditions. Notice the bias is sufficiently small to allow the validation of different descriptions of the atmospheric state. Fig. 3.7 also shows biases between simulated AIRS radiances from the ECMWF model analyses and the observed AIRS data for two different versions of SARTA. The 2004 version is derived using modified absorption coefficients based on TWP data. Note the bias for the water vapor region of the spectrum (1300 to 1600 cm^{-1}) is significantly smaller for the ARM TWP sites and the 2004 version of SARTA has smaller residuals than the earlier version. For channels predominately sensitive to

temperature (e.g. 700 – 800 cm^{-1} and 2200- 2300 cm^{-1}) the differences of the biases are much smaller. In other words, the model derived temperature fields are more accurate than the corresponding moisture fields. Also moisture is much more variable in space and time than temperature, and generally result in larger differences between measured and computed brightness temperatures for water vapor channels because of the inexactness of the spatial and temporal collocations.

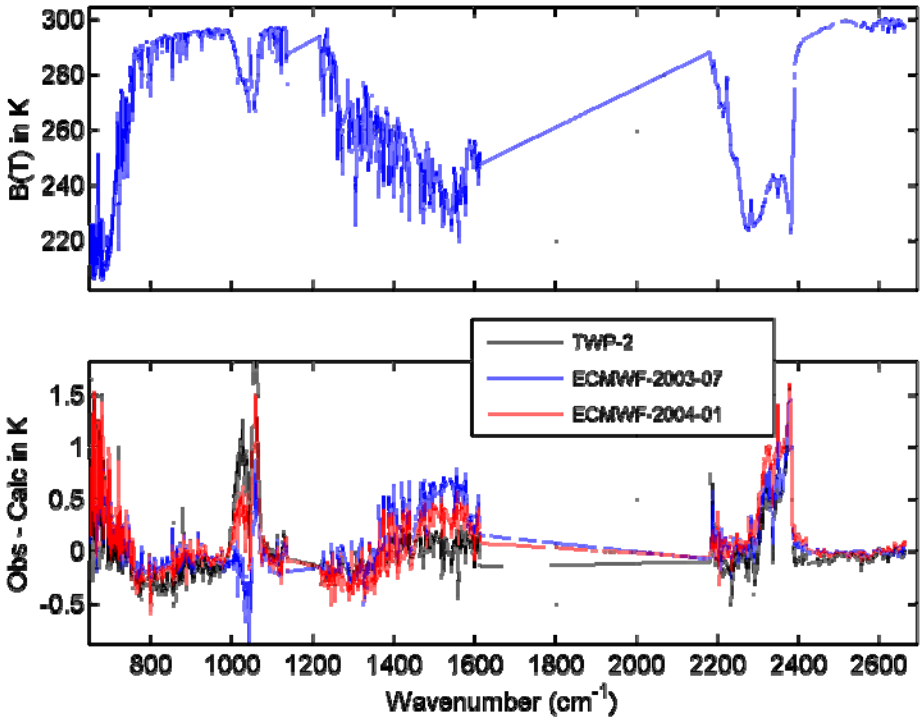

Fig. 3.7: Upper panel: Brightness temperatures observed by AIRS at the tropical western pacific ARM site (TWP-2) Lower panel: Brightness temperature residuals between observed and calculated brightness temperatures from the TWP-2 site and from ECMWF.

3.6 Data used in the Generation of Eigenvectors and Limb Adjustment Coefficients.

It is very important for the eigenvectors to represent all AIRS radiance spectra, so that a given linear combination of the truncated eigenvectors will reproduce the near noise free AIRS radiance spectra. I used a 6 month period of data starting on January 15, 2003 to generate the eigenvectors.

This ensemble was constructed by first generating eigenvectors for "day 1" of the six month period; these eigenvectors are applied over the six months of data. Any reconstruction score found to exceed 1.2 was added to the original ensemble. The eigenvectors are then recomputed using the updated ensemble.

To generate the limb adjustment coefficients, PC scores as a function of scan angle beam position (90 per scan line) are averaged for 2 degree latitude bands for ocean and non ocean cases (for the same six month period) Such averaging results in a matrix dimensioned 200 x 180 by 90. The 200 elements represent the first 200 PC scores, 180 elements are the total number of latitude bands (90 bands x 2 (ocean/non ocean)), and 90 is the number of beam positions. Averaging over such a long period of time reduces any scan angle variation due to air mass and surface features. Linear regression is used to generate a matrix of limb adjustment coefficients which is dimensioned 7 predictors by 90 beam positions. The seven predictors are the first six PC scores and the PC score to be limb adjusted. The averaged first four PC scores are shown in Fig. 3.8 Each plot shows the PC score as a function of scan angle (x-axis) which is given only for the center AIRS footprint within the AMSU footprint

(i.e., 1-30, instead of 1-90) and by latitude (y-axis) which ranges from 1 – 90 latitude bins). The principal component scores are normalized by the square root of their eigenvalue. Note that the fourth PC score has a strong view angle dependency and is an important predictor for limb adjustment.

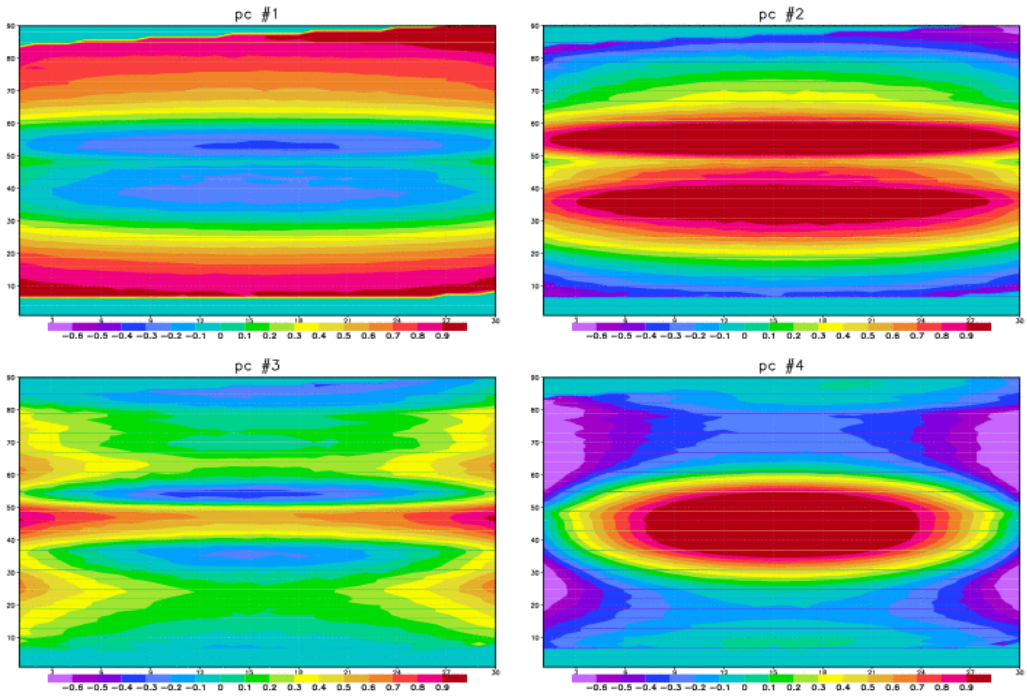

Fig. 3.8: First four principal component scores normalized by the square root of their eigenvalue (color scale range +- 1.0) and averaged over latitude bins (y-axis) and view angles (x-axis)

3.7 Cloud Detection

Applications of the radiance climatology will require the use of clear spectra, and therefore an algorithm to discriminate clear from cloud contaminated scenes is needed. An algorithm consisting of five different tests was developed to find mostly clear observations. Only the fifth test makes use of ancillary non-satellite

information. The first test makes use of the Advanced Microwave Sounding Unit (AMSU) thermal channels. Since microwave brightness temperatures are not sensitive to non-precipitating clouds, the AMSU observations are used to predict a single AIRS channel at 2390 cm^{-1} wavenumber. The 2390 cm^{-1} channel can be predicted from AMSU-A with an accuracy of about 1 K. The weighting function for this particular AIRS channel has a peak value near 850 mb. The 2390 cm^{-1} channel is ideal because it is predominately affected by temperature and contamination from water vapor and other trace gases is negligible. Simulations have shown that this channel is only marginally affected by solar contamination for clear conditions. Ideally, a channel peaking lower in the troposphere would be better for detecting very low altitude clouds. However, predicting near-surface AIRS channels would require the use of AMSU-A window channels. The large variability of the AMSU-A window channels due to variations in cloud liquid water and surface emissivity result in a very poor prediction (> 5 K) of near-surface AIRS channels. Test 1 compares the predicted and observed 2390 cm^{-1} channel brightness temperatures; if the observed is colder by 3K then the AIRS footprint is not cloud-free. For overcast conditions during the day, solar contamination can result in a warm brightness temperature. To avoid false detection of clear footprints due to solar contamination of the 2390 cm^{-1} channel in presence of clouds, Test 2 was added to compare the difference of longwave and shortwave infrared window brightness temperatures at 2558.23 (solar sensitive) and 937.81 cm^{-1} (solar insensitive). If the difference is greater than 10 K, the footprint is not cloud-free. Experiments have found that footprints with very low level clouds are often not detected. This of course was expected since the 2390 cm^{-1}

channel peaks near 850 mb. To improve the detection of very low clouds, Test 3, the coherence test, computes the standard deviation of the 3x3 array of the 2390 cm^{-1} channel radiance within the AMSU-A footprint. Radiance is used instead of brightness temperature because the noise is temperature dependent. If the standard deviation is greater than 3 times the noise, then the footprint is not cloud-free. This test can produce false positives in regions of high and variable terrain. Test 4 is used over ocean, the test simply checks if brightness temperature at a single longwave window channel at 965.43 cm^{-1} is warmer than 270 K. If it is less than 270 K, it is almost certain that clouds are present since the freezing temperature of sea water is near 271 K. Test 5 makes use of the NCEP model surface temperature. The surface temperature is predicted from four AIRS window channels at 918, 965, 1228 and 1236 cm^{-1}. Using simulated brightness temperatures, the surface temperature can be predicted within 0.2 K. However in practice, the surface temperature from the model is considerably more accurate over ocean than land, so different thresholds are used. For ocean, the predicted sea surface temperature must be no colder than 1K of the NCEP SST value. Over land, because the NCEP surface temperature can have large errors, the test is used as a sanity check with the threshold set to 10 K.

Coefficients predicting the AIRS 2390 cm^{-1} brightness temperature from AMSU channels 4, 5 and 6 brightness temperatures, and the surface temperature from the four AIRS window channels, are all derived from simulated AIRS and AMSU brightness temperatures. The brightness temperatures were simulated from the NCEP analyses. The AIRS 2390 cm^{-1} test uses AMSU channels 4, 5 and 6, the cosine (COS) of the solar zenith angle (SZA), and cosine of the scan angle (SA).

AMSU channels 4, 5 and 6 weighting function peak at 800, 600 and 400 mb, respectively. The regression solution is:

$$\text{Predicted AIRS (2390 cm}^{-1}) = 18.653 - 0.169 * \text{AMSU4} + 1.975 * \text{AMSU5} - 0.865 * \text{AMSU6} + 4.529 * \cos(\text{SZA}) + 0.608 * (1 - \cos(\text{SA})) \quad (3.5)$$

The regression solution for predicting surface temperature is:

$$\text{Predicted Surface Temperature} = 8.28206 - 0.97957 * \text{AIRS}(918\ \text{cm}^{-1}) + 0.60529 * \text{AIRS}(965\ \text{cm}^{-1}) + 1.74444 * \text{AIRS}(1228\text{cm}^{-1}) - 0.40379 * \text{AIRS}(1236\ \text{cm}^{-1}) \quad (3.6)$$

For cloudy conditions with mean cloud fractional amount of 0.45 (where 1 = complete overcast) and a standard deviation of 0.33, the percentage of the entire population detected as clear is only about 5% [*Goldberg et al.*, 2003]. The clear detection test over ocean is quite accurate with an overall cloud residual contamination of only 0.6%, while land cases have a residual contamination of 2.5% due to greater uncertainties in surface emissivity and greater surface inhomogeniety.

Chapter 4: Validation of the Principal Component Analysis (PCA) and Limb Adjustment Procedures

4.1 Validation

Validation of the AIRS PCA is very straightforward. One simply needs to compare the reconstructed radiances with the original values. Plots similar to Fig. 3.3 are generated each day to ensure the representativeness of the eigenvectors. Fig. 4.1 shows the observed, reconstructed and difference for a randomly selected granule for an AIRS channel centered at 1002.24 cm^{-1} wavenumber. Here we can see the reconstruction is very accurate, the distribution of the differences is Gaussian, with a standard deviation of 0.10 C, which is nearly the same as the 0.10 instrumental noise value.

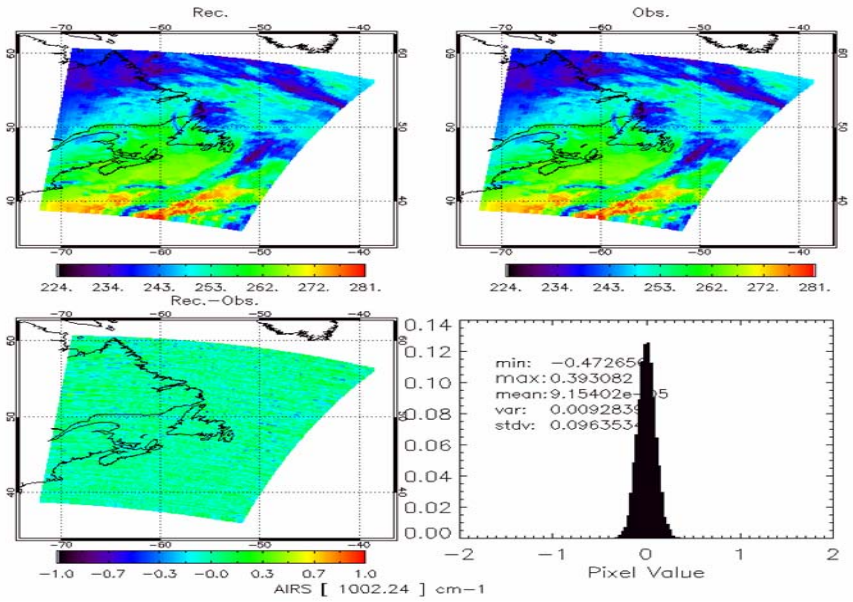

Fig. 4.1 Reconstructed brightness temperatures (upper left), observed brightness temperatures (upper right), reconstructed minus observed (lower left) and the distribution of the differences (lower right) for AIRS channel centered at 1002.24 cm^{-1}

The limb adjustment is first validated by comparing the deviations of the uncorrected and limb adjusted radiances from nadir values as a function of angle for a large spatial and temporal domain. Fig. 4.2 shows the mean deviation from nadir averaged over the month of September 2005 for a latitude range between +- 40 degrees. This comparison was done for the approximately 250 AIRS channel subset assimilated operationally by NCEP and ECMWF. Each solid curve shows the deviation in brightness temperature from the nadir value for groups of channels with similar weighting functions. The first two channel groups are sensitive to the stratosphere. As the scan angle increases, the atmospheric path increases, causing greater absorption and a rise in height of each channel's weighting function. In the stratosphere, with temperature increasing with height, this results in an increase of brightness temperatures with increasing scan angle. The deviations after the limb adjustment (dashed curves) are less then 0.25 K for all angles.

A more detailed validation is accomplished by comparing deviations between observed brightness temperatures with those simulated from ECMWF analysis fields, and limb adjusted brightness temperatures with those simulated from ECMWF analysis fields assuming a view angle of zero. This is a very important step in the validation process for the algorithm. By comparing the statistics of differences between measured and computed brightness temperatures for the original and limb adjusted brightness temperatures we will be able to clearly assess if there is a degradation of information by the limb adjustment procedure. If the statistics

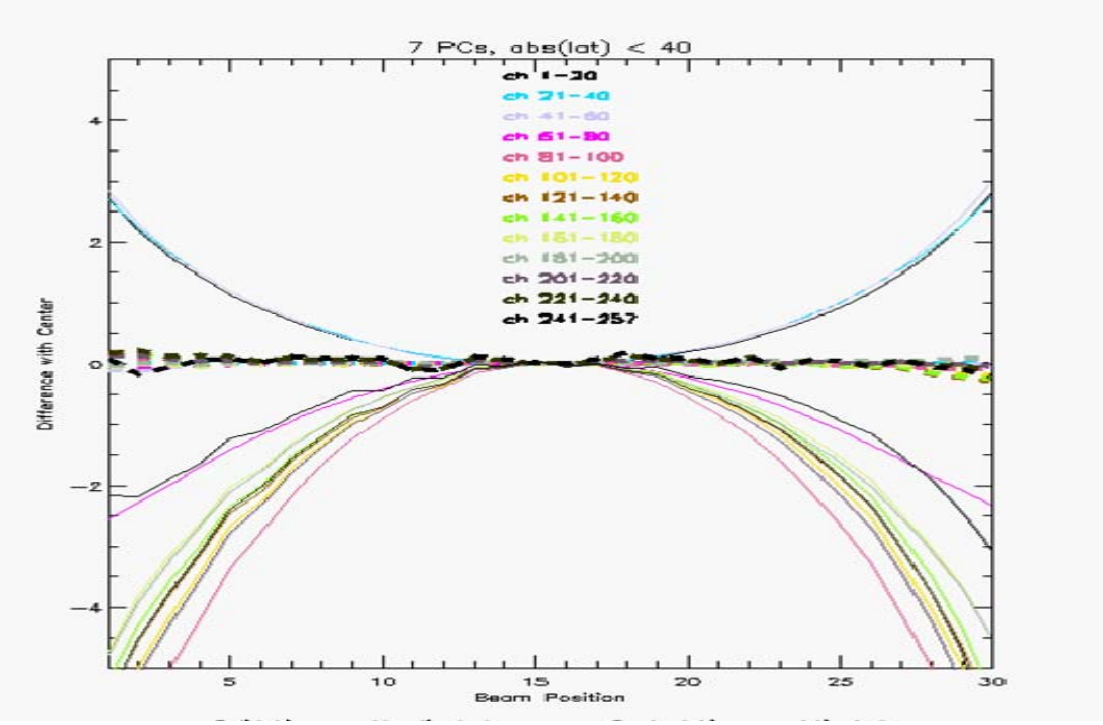

Fig. 4.2: Deviations of averaged original (colored curves) and limb adjusted (heavy dashed curve) brightness temperatures from nadir as a function of beam position.

for the two populations are nearly the same, then we can assume there is no degradation. Fig. 4.3 through Fig. 4.9 show these comparisons for AIRS channels at the following wavenumbers, in cm^{-1} (the peak of their weighting functions for a representative summer midlatitude atmospheric state are given in parentheses), 666.766 (40 mb), 681.457, (90 mb), 704.436 (350 mb), 723.029 (700 mb), 801.099 (850 mb), 1519.07 (315 mb) and 1598.49 (490 mb), respectively. The last two channels are water vapor channels, while the other channels are primarily sensitive to atmospheric temperature. Each figure includes the bias, rms, and the minimum and maximum of the deviations. The unadjusted and limb adjusted statistical parameters are nearly the same. The relatively larger cold bias in the 801.099 cm^{-1} channel is due to low level cloud contamination. It should be noted that the weighting function

peak pressure is a function of airmass. Table 4.1 gives the weighting function peak pressure of the single AIRS channels which have been or will be discussed in this dissertation for three different sets of atmospheric states. Notice that the peak of the two water vapor channels has the largest range. All weighting peak pressures referred to in this dissertation are for the summer midlatitude atmospheric state; their weighting functions are shown in Fig. 4.10. The three atmospheric states are given in Fig. 4.11.

These results show that there is no degradation of information due to the limb adjustment and validate the method developed for limb adjustment.

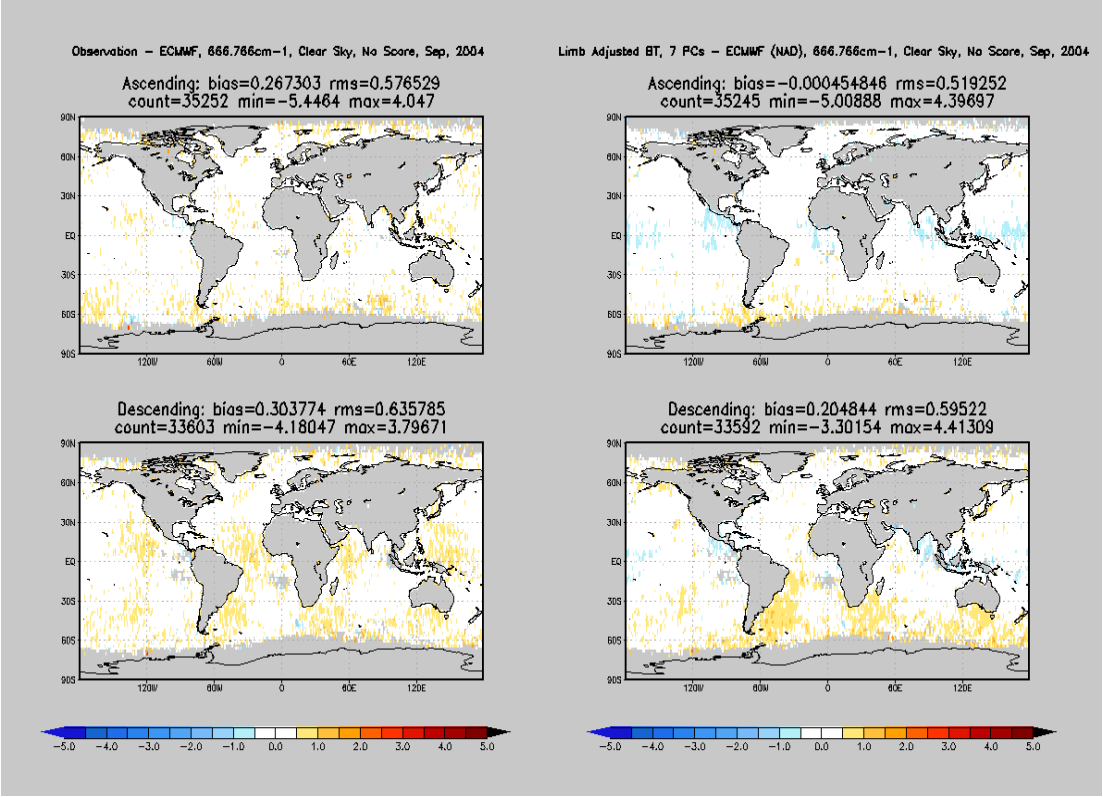

Fig. 4.3: The difference between observed and calculated brightness temperature using the ECMWF model analysis at the original AIRS viewing geometry separated for ascending and descending data (left upper and lower), and the difference between limb adjusted brightness temperatures and nadir calculated (scan angle = zero) using the ECMWF model analysis (right upper and lower) for AIRS channel centered at 666.766 cm^{-1} and with atmospheric weighting function peak near 40 mb.

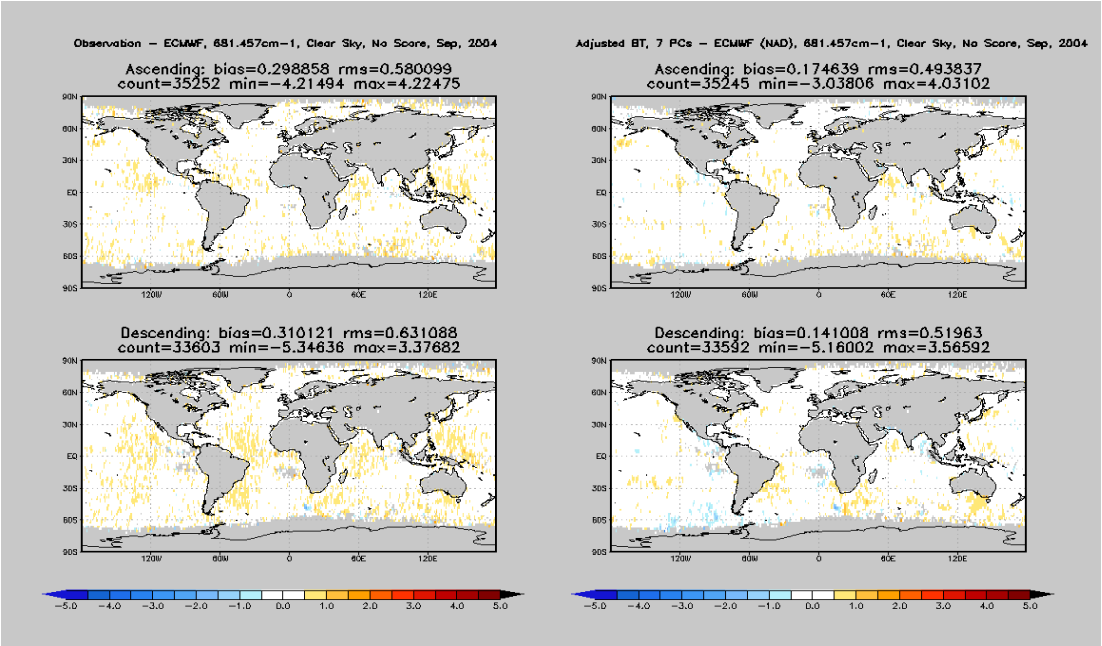

Fig. 4.4: Same as Fig. 4.3 except for AIRS channel centered at 681.457 cm^{-1} and with atmospheric weighting function peak near 90 mb.

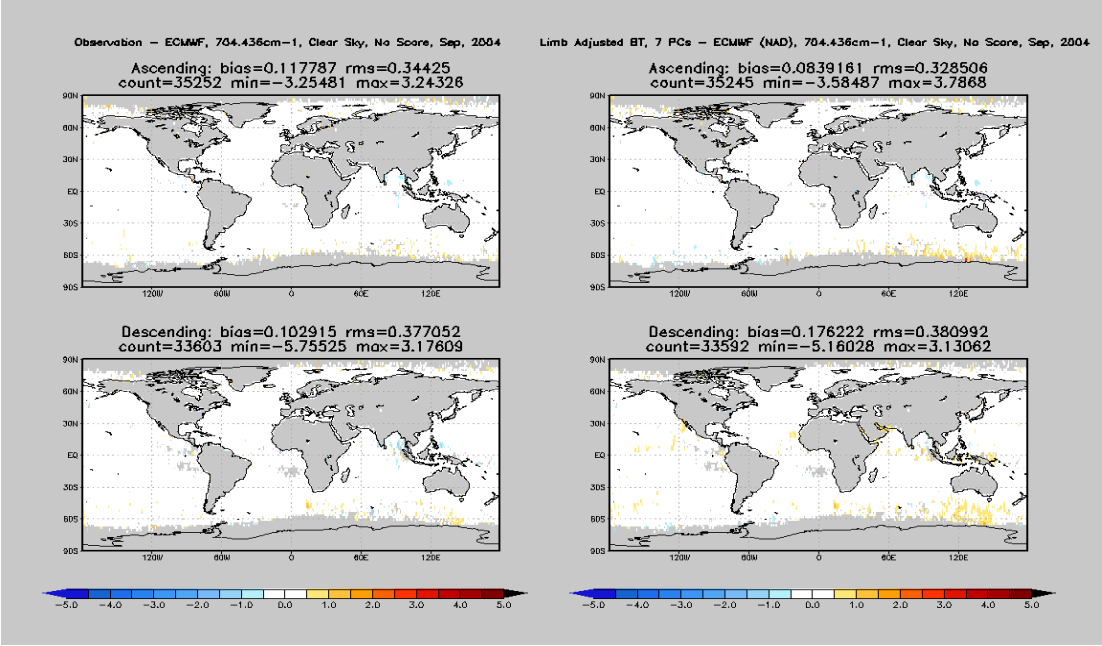

Fig. 4.5: Same as Fig. 4.3 except for AIRS channel centered at 704 .436 cm^{-1} and with atmospheric weighting function peak near 350 mb.

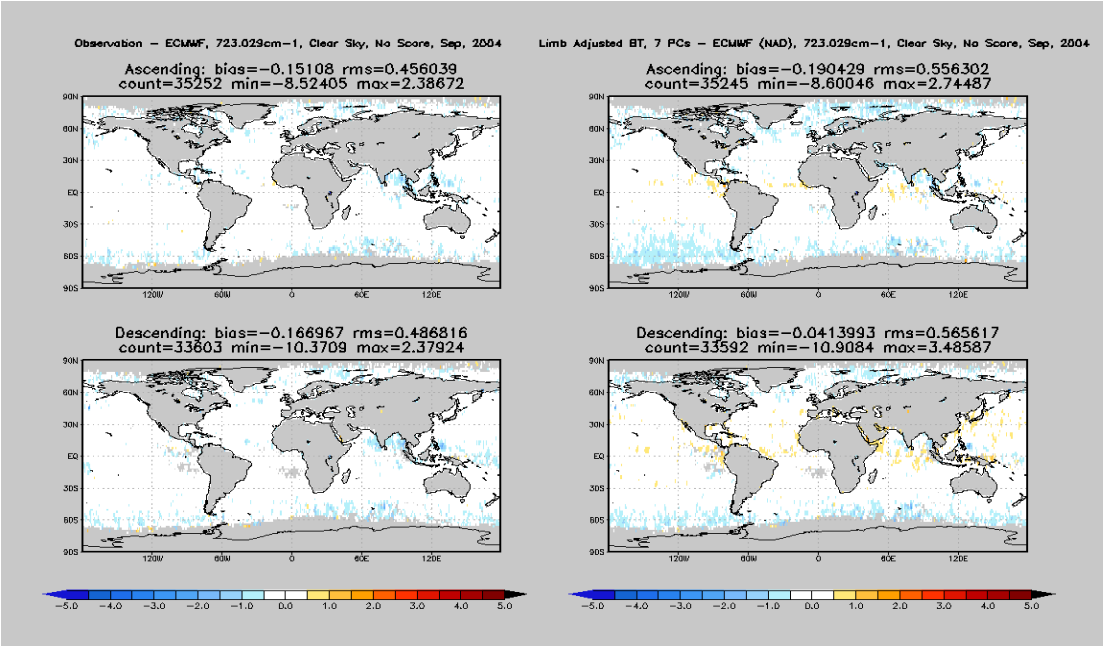

Fig. 4.6: Same as Fig. 4.3 except for AIRS channel centered at 723.029 cm^{-1} and with atmospheric weighting function peak near 700 mb.

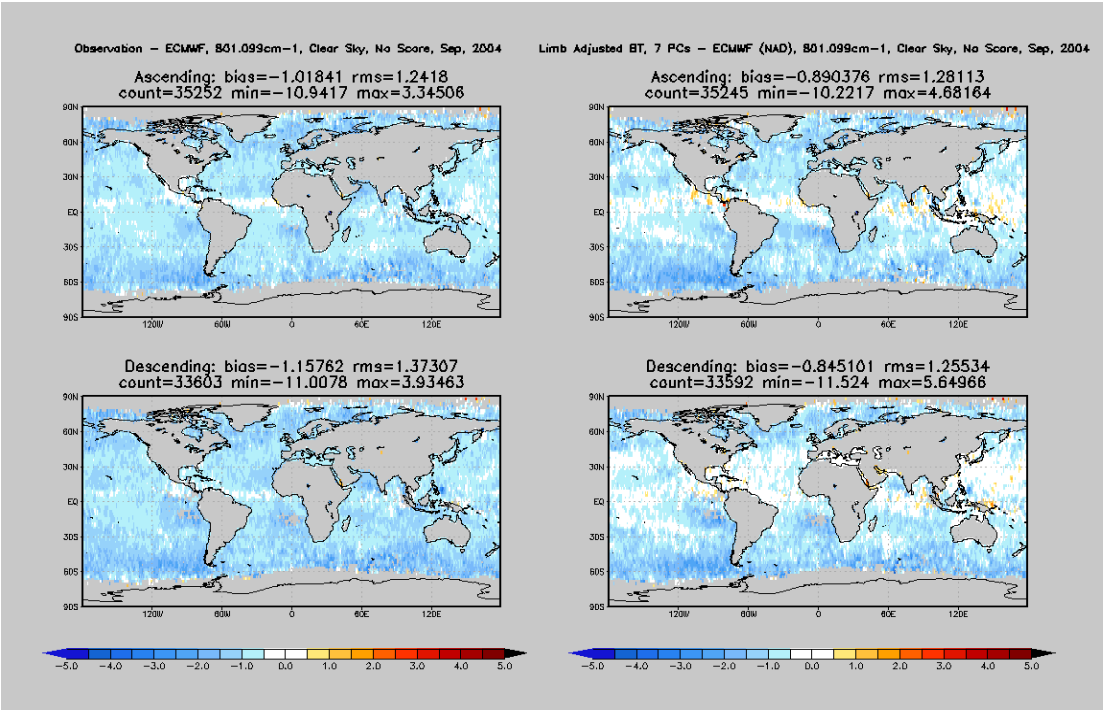

Fig. 4.7: Same as Fig. 4.3 except for AIRS channel centered at 801.099 cm^{-1} and with atmospheric weighting function peak near 850 mb.

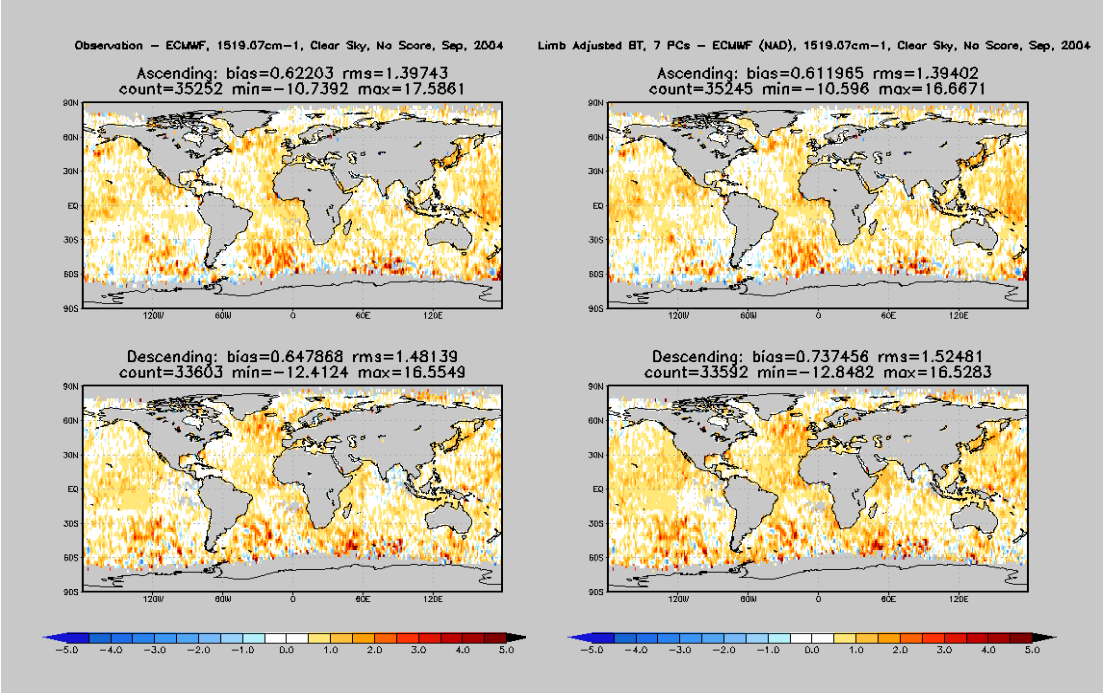

Fig. 4.8: Same as Fig. 4.3 except for AIRS channel centered at 1519.07 cm^{-1} and with atmospheric weighting function peak near 315 mb.

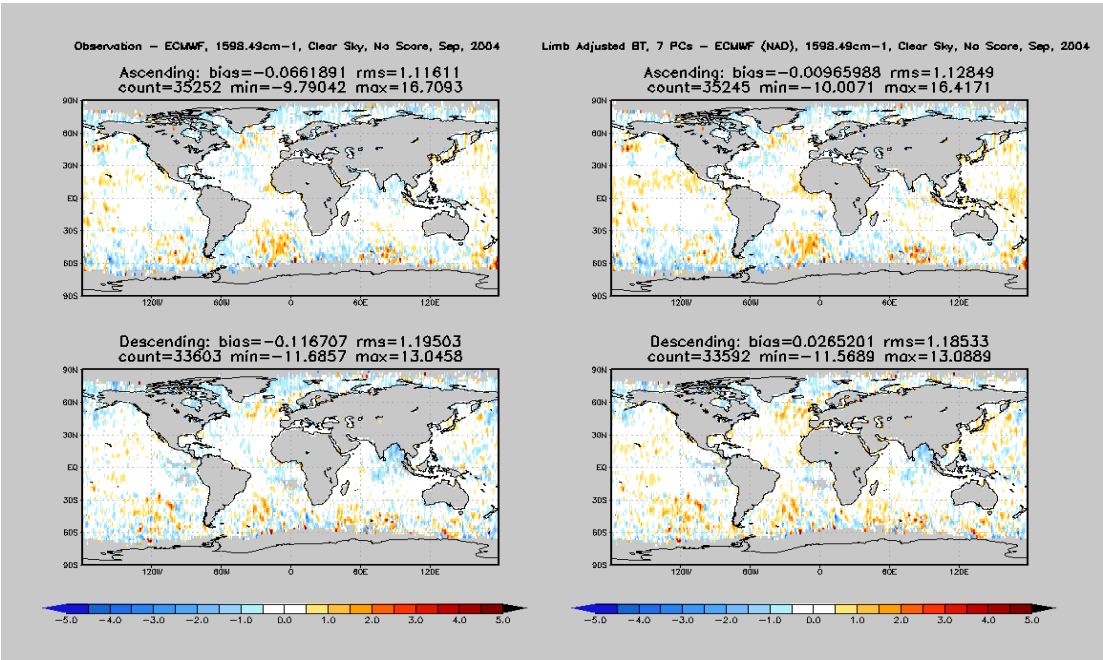

Fig. 4.9: Same as Fig. 4.3 except for AIRS channel centered at 1598.49cm^{-1} and with atmospheric weighting function peak near 490 mb.

Table 4.1 Weighting function peak pressures of selected channels for three airmass: Polar, Midlatitude and Tropical.

Channel	polar	mid latitude	tropical
667.775 (cm-1)	1.5 (mb)	1.5	1.5
667.27	15	15	10
667.03	30	25	20
666.766	40	40	35
681.457	80	90	70
689.491	150	150	150
704.436	200	350	300
723.029	900	700	600
801.099	1000	850	850
1519.07	400	315	290
1598.49	600	490	400

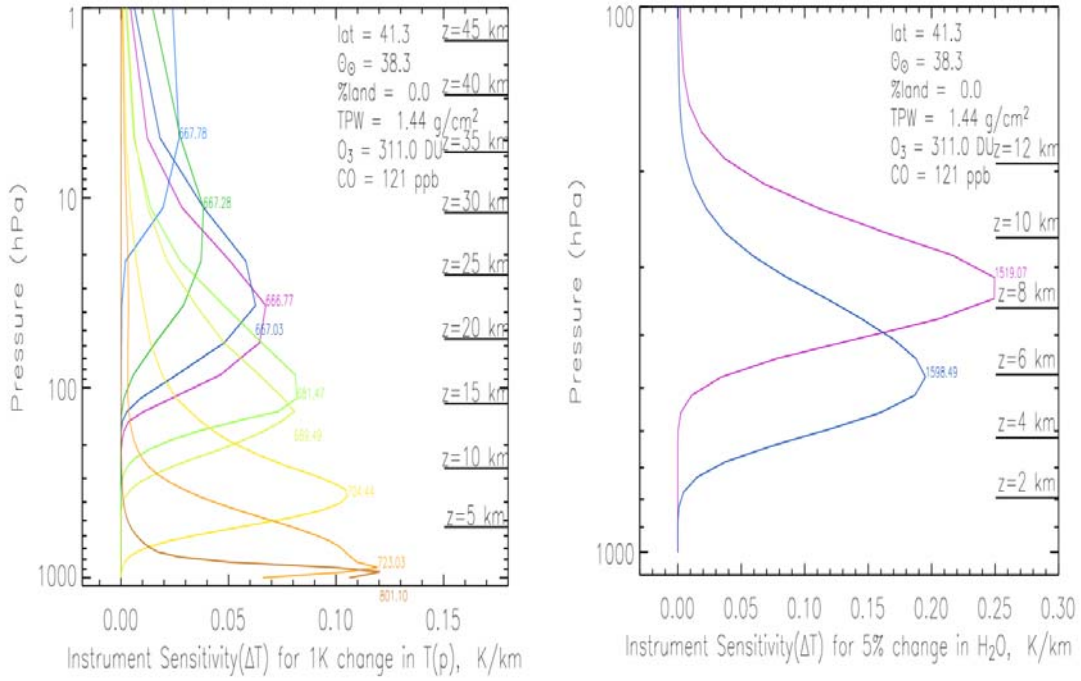

Fig. 4.10: Weighting functions representative of the midlatitude airmass for the AIRS channels listed in Table 4.1.

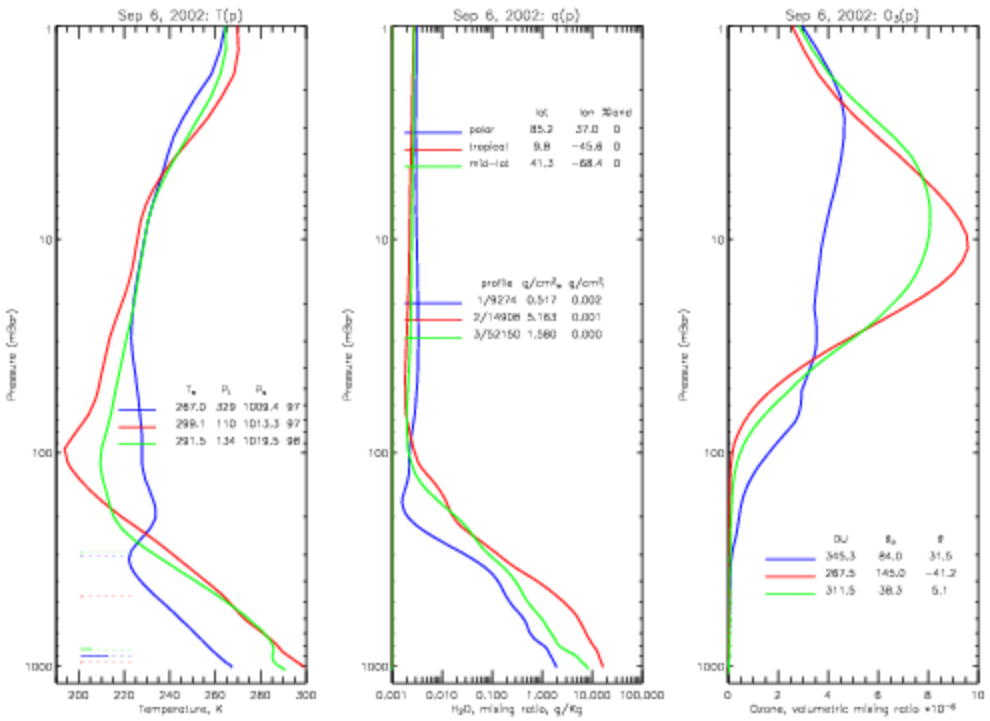

Fig. 4.11: Atmospheric states of temperature, water vapor and ozone representing polar (blue), midlatitude (green) and tropical (red) airmasses.

Chapter 5: Applications

5.1 Introduction

The SRIR climatology includes daily PCS data files which contain the first 200 PCS, along with the AMSU brightness temperatures. The eigenvectors and the limb adjustment coefficients are static. With these coefficients, the daily PCS files can be converted to limb adjusted brightness temperatures. The data also contain the result of the clear test that is used to determine if a particular observation is predominantly free of cloud contamination. The climatology currently covers the period from January 2003 through December 2006. Monthly datasets, ascending and descending, are averaged from the daily limb adjusted brightness temperatures.

Two important applications are now demonstrated. The first is to use the climatology to detect and investigate potential areas of large atmospheric change. The second is to use the climatology to independently validate model analyses, such as those derived from NWP models, climate reanalyses, and climate prediction models. This study will demonstrate the usefulness of the climatology for validating NWP model analyses.

5.2 Climate Change Detection

The SRIR climatology provides very accurate information on the top of the atmosphere infrared radiance at high spectral resolution. The spectral range is from 650 to 2750 cm^{-1} wavenumbers, equivalent to 15.6 to 3.75 micron wavelengths. Fig. 5.1 is an example of images which can be produced for an upper tropospheric water

vapor channel at 1520.87 cm^{-1}. This figure shows the mean clear-sky brightness temperature for January and July 2005, separated into ascending and descending data (day and night). The patterns are different between July and January. The regions with higher brightness temperatures are generally areas with low water vapor. In these areas, the water vapor weighting functions will peak lower in the atmosphere resulting in warmer brightness temperatures.

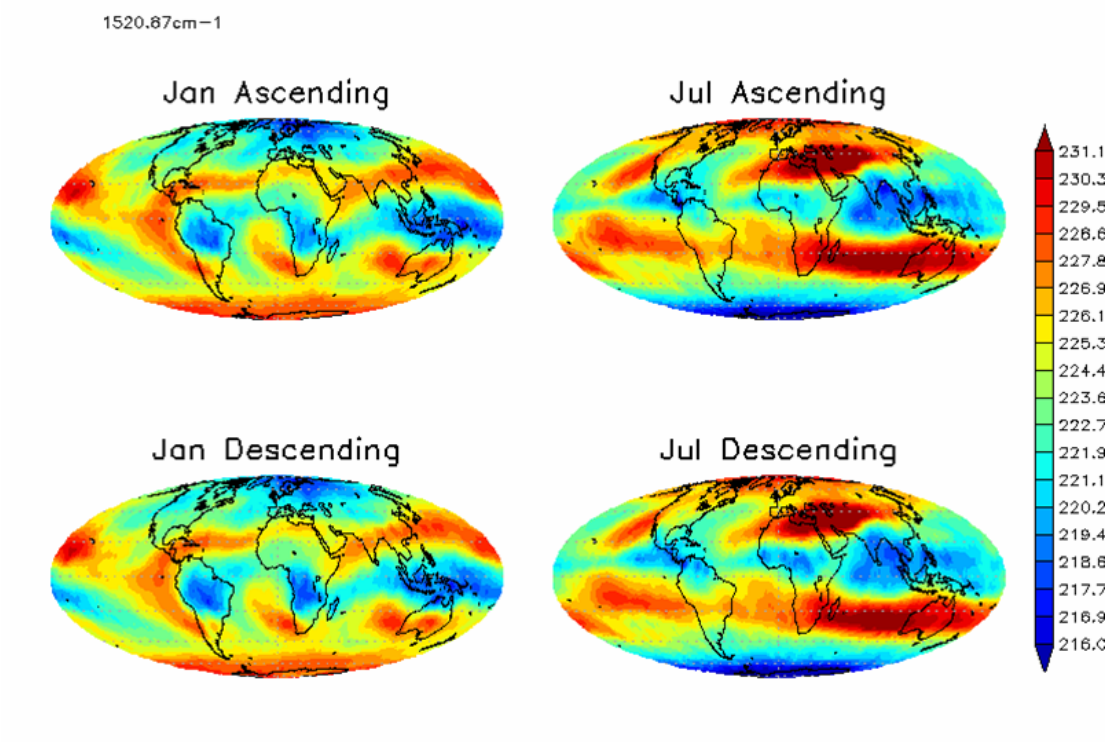

Fig. 5.1 Mean brightness temperature field for January and July 2005 for AIRS water vapor channel centered at 1520.87 cm^{-1}.

Quantitative analysis of differences between different years of spectra can be an indicator of regions experiencing large changes. Since the radiance climatology still covers a relatively short period of time, a search for significant differences was performed by comparing mean spectra from the same month for different years. Fig.

5.2 shows differences of spectra for July 2004, 2005 and 2006, for all sky conditions (clear, partial clouds, overcast) and for ascending data (day time). (Results for night time are nearly identical) In this example the differences are rather small and spectrally featureless, with the exception of the spectral range of 650 to 700 cm^{-1}, which is sensitive to the upper troposphere and stratosphere. The spectral range of 700 to780 cm^{-1} is sensitive to the mid to lower troposphere. The spectral range of 780 to1000 cm^{-1} is primarily sensitive to the surface (with some weak absorption due to water vapor). And the spectral range of 1000 to1100 cm^{-1} is sensitive to ozone, with the peak of the ozone band at 1040 cm^{-1}. The difference between the two curves is the difference between 2005 and 2006, and the difference is nearly zero, with the exception of a few tenths of a degree in the upper troposphere and stratosphere.

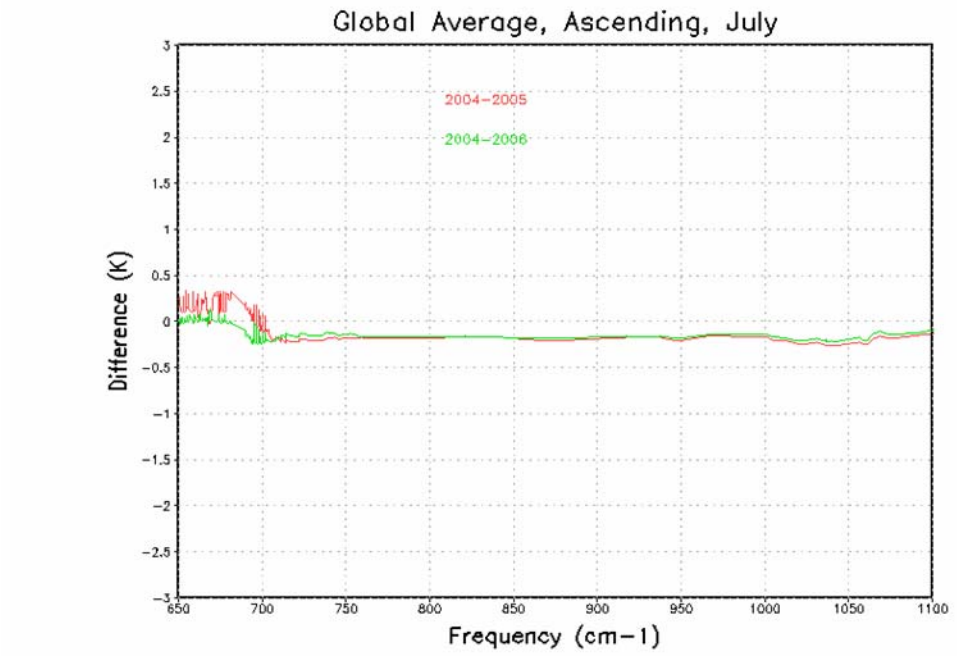

Fig 5.2: Differences of spectra for July 2004, 2005 and 2006, for all sky conditions (clear, partial clouds, overcast) and for ascending data (day time) between 650 and 1100 cm^{-1} wavenumber.

Fig. 5.3 shows differences of spectra for January 2004, 2005 and 2006. In this figure, there are appreciable differences in the lower to mid troposphere and the surface. However the most noticeable feature is the difference between 2005 and 2004 near the center of the ozone band. The difference is approximately 0.6 K, which, based on Fig. 3.6, translates to a difference of about 5% in total ozone. This feature warrants further investigation and will demonstrate the utility of the SRIR climatology.

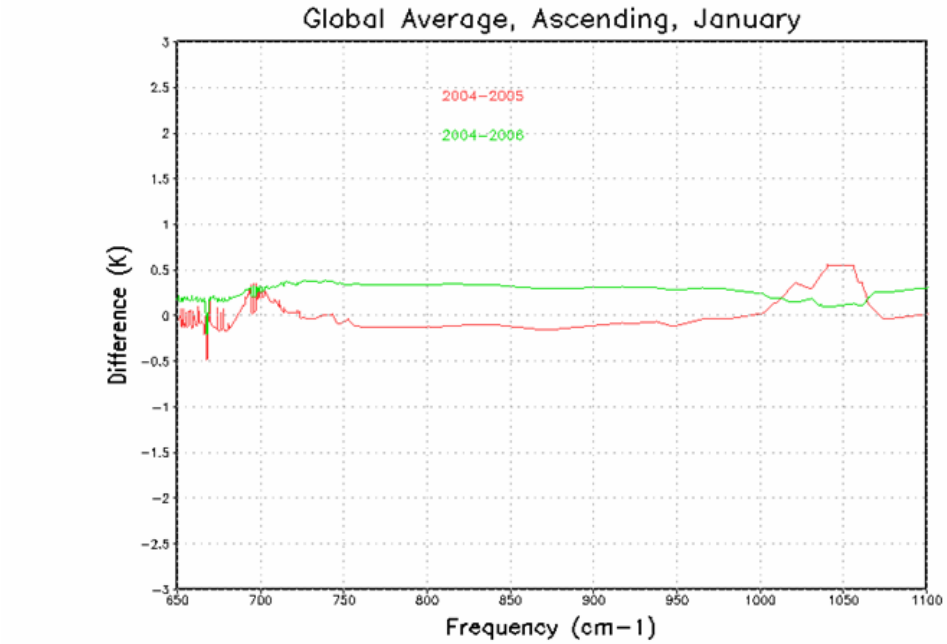

Fig. 5.3: Differences of spectra for January 2004, 2005 and 2006, for all sky conditions (clear, partial clouds, overcast) and for ascending data (day time) between 650 and 1100 cm^{-1} wavenumber.

The first step is to examine the difference fields generated between 2004 and 2006, which is given in Fig. 5.4. The differences are within normal interannual variations. However, in Fig. 5.5, the difference fields between 2005 and 2004 show very large

departures poleward of 60 degrees north latitude. January 2005, north of Canada, is significantly colder by more than 8 K. A study by *Schiermeier* [2005], Fig. 5.7, reported on the largest observed depletion in ozone, of approximately 140 Dobsons (relative to a normal amount of 300), in the Arctic in January 2005 as well as very low stratospheric temperatures. The large reduction in the AIRS brightness temperature is due to two factors: a much colder stratosphere as a result of the reduced ozone and the reduced infrared absorption due to the reduced ozone. Theoretically, a 50% change in ozone can cause AIRS brightness temperatures to change by 8 degrees since a 0.5% change, as was shown in Fig. 2.7, can cause a change of 0.08 K. However, the actual change is dependent on the shape of the temperature profile, since a change in ozone results in the change in the peak and shape of the ozone channel's weighting function. Less ozone broadens the weighting function and reduces its height. So a reduction in ozone results in AIRS observing more of the lower stratosphere. In a nearly isothermal atmosphere, the change in ozone concentration would have very little impact on the brightness temperature, whereas a temperature profile with a large lapse rate will correspond to a significant change in brightness temperature

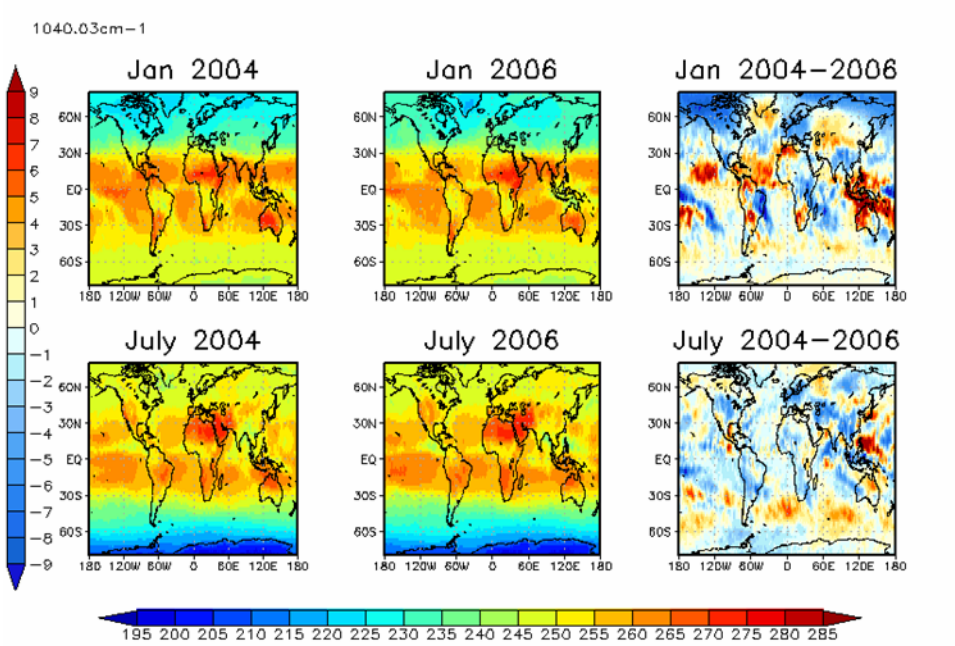

Fig. 5.4: Brightness temperature fields for January, July 2004 and 2006, and their differences for AIRS channel centered at 1040.03 cm^{-1} wavenumber.

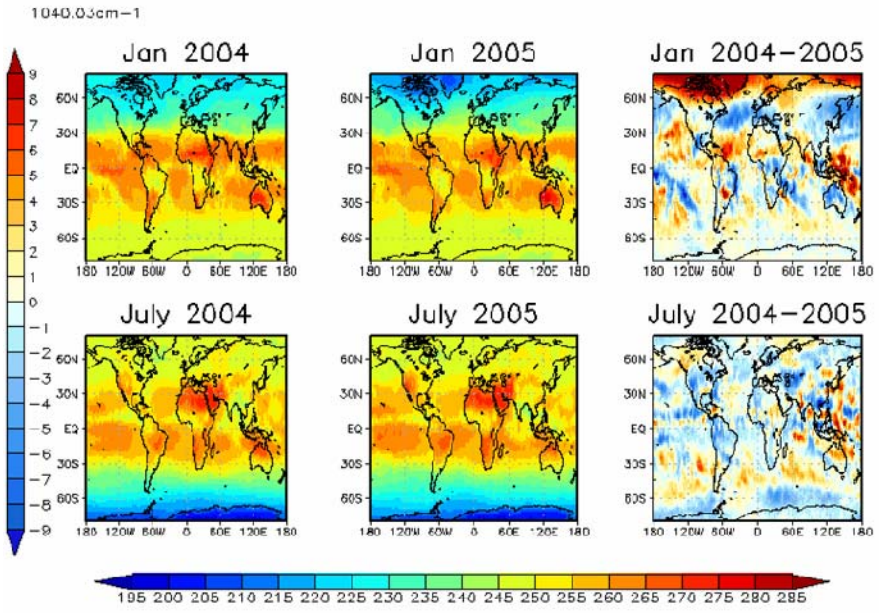

Fig. 5.5: Brightness temperature fields for January, July 2004 and 2005, and their differences for AIRS channel centered at 1040.03 cm^{-1} wavenumber.

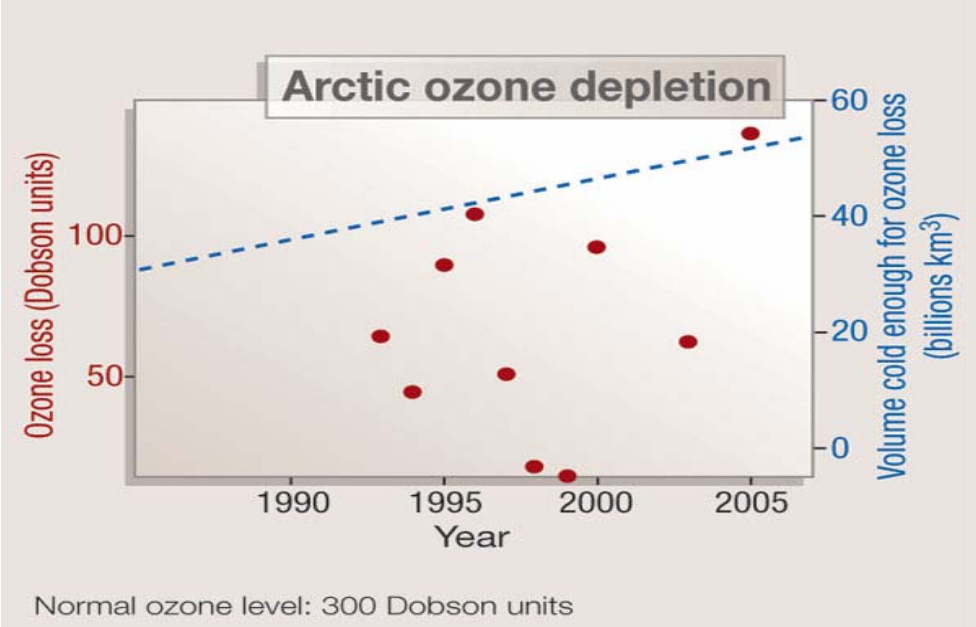

Fig. 5.6: Artic ozone depletion from 1992 to 2005 (from Schiermeier (2005)).

This example shows that the SRIR climatology has significant value for finding and investigating regions of large changes in outgoing longwave radiation at high spectral resolution and then determining which atmospheric constituent contributed to the change.

5.3 Validation of Model Analyses

The most common analysis methods in NWP are optimum interpolation and variational data assimilation. Both methods make corrections to a first guess forecast (typically a 6 hour forecast from the analysis 6 hours earlier) in such a way that the differences between the corrected first guess and the accepted observations at the analysis time are minimized. Therefore information from the forecast, which is based

on assumptions of model physics, is retained in the analysis. Analysis fields are used to initialize the next series of forecasts and are also used as truth for validating forecasts for different time periods. Analysis fields are used for providing the best estimate of the atmosphere. A climate reanalysis provides a historical collection of analyses from which trends and variability in climate can be assessed. Weather prediction centers, as part of their operations, generate analyses and forecast fields. The fields generated from each center are different due to differing data assimilation and forecast systems. Though the analysis is often regarded as truth, there are different "truths" from different NWP centers. Therefore, it is of utmost importance to independently assess the accuracy of different analysis systems. The use of the SRIR climatology will provide this very important capability.

5.4 Comparisons of ECMWF and NCEP analysis fields

ECMWF and NCEP analysis fields are available at 6 hour intervals. Both models provide the atmospheric states of temperature, water vapor, ozone, and surface temperature needed to simulate outgoing clear radiances. Both models also include cloud information, and therefore the SRIR climatology can be used to validate the accuracy of model-derived clouds as part of a future study. The spatial resolution of ECMWF is a 0.5 x 0.5 lat/lon grid, where as NCEP is at a 1 x 1 degree grid. The top model layer boundaries for NCEP is 0.64 sigma to zero (0.64 mb for 1000 mb surface pressure), whereas for ECMWF the top layer is 0.2 to zero. Both data are interpolated, spatially and temporally, to the AIRS location and time. The

NCEP results shown in figures are also labeled GDAS, which is an acronym for the NCEP's Global Data Assimilation System. The SRIR climatology for validating the model analysis has one very important limitation, which is, the 3-5 km vertical resolving capability of the infrared radiances. In other words, differences between two model analyses may be indiscernible by the SRIR climatology if the difference is isolated to a very shallow atmospheric layer. Therefore the comparisons begin with examining difference fields between simulated brightness temperatures from NCEP and ECMWF analysis fields to assess differences at the vertical resolution of the SRIR climatology. Fig. 5.7 through Fig. 5.9 show differences between ECMWF and NCEP simulated brightness temperature fields for a set of channels representative of different atmospheric layers for September 2004. The figure caption includes the channel wavenumber and in parentheses the peak region of atmospheric or surface contribution (for midlatitude airmass).

Fig. 5.7 through 5.9 show channels predominately influenced by temperature. From the lower troposphere to the middle stratosphere the root mean square of the differences between NCEP and ECMWF is no larger than 0.22 K. The overall mean bias is well within 0.1 K. It's not until the upper stratosphere where the differences become significant, as shown in Fig. 5.9. The differences between the two models in the upper stratosphere are mainly due to differences in model physics, vertical layering and the satellite data being assimilated. NCEP, for example, does not assimilate AMSU channel 14 because, even though this channel peaks at about 1.5 mb, the NCEP model top layer, (0.67 sigma to zero), is too coarse for accurate

forward model computations. Whereas ECMWF's top layer, (0.2 sigma to zero), is sufficiently narrow to allow the assimilation of AMSU channel 14.

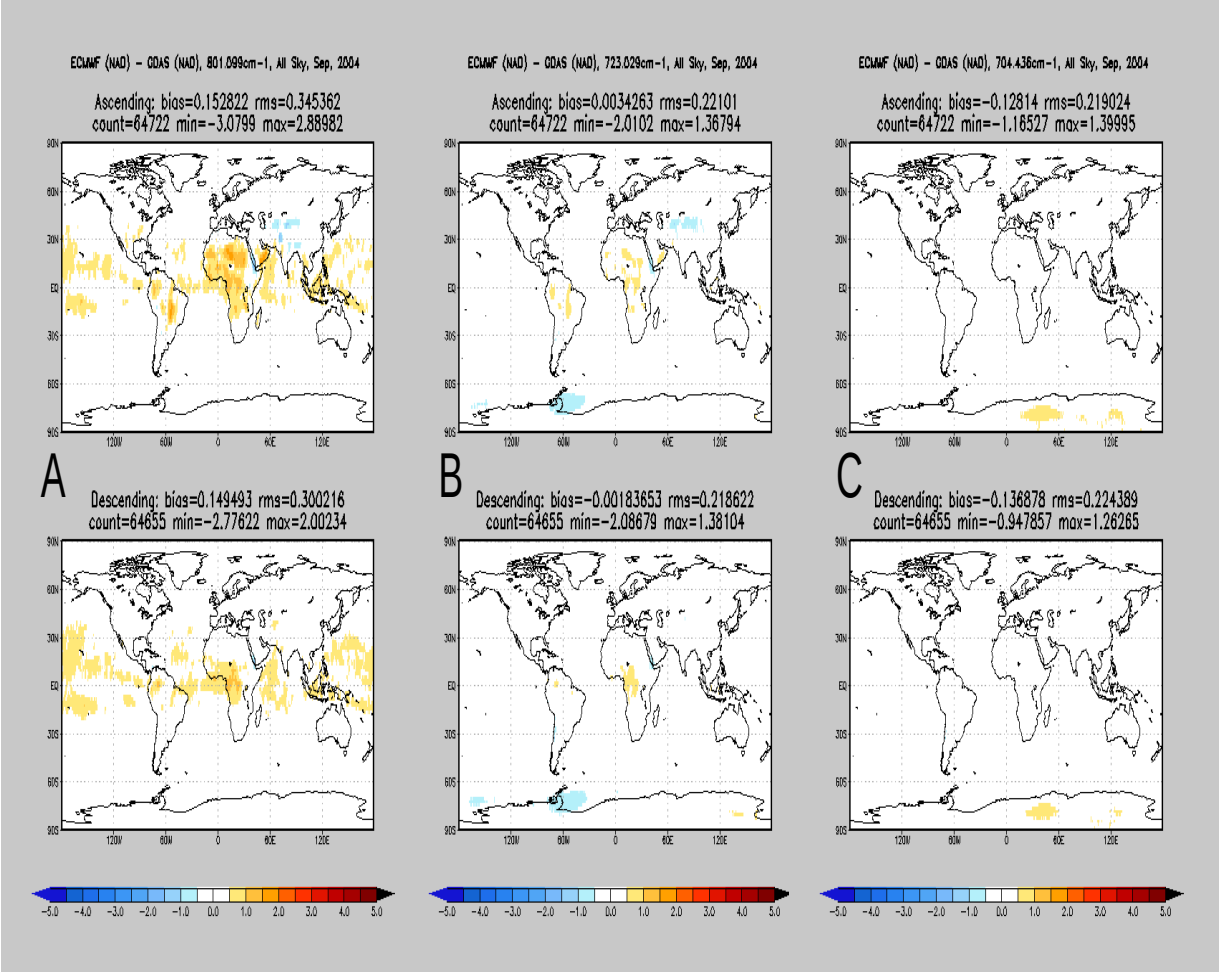

Fig. 5.7: ECMWF minus GDAS simulated brightness temperatures for A: 801.09 cm^{-1} (850 mb), B: 723.029 cm^{-1} (700 mb), and C: 704.436 cm^{-1} (350 mb)

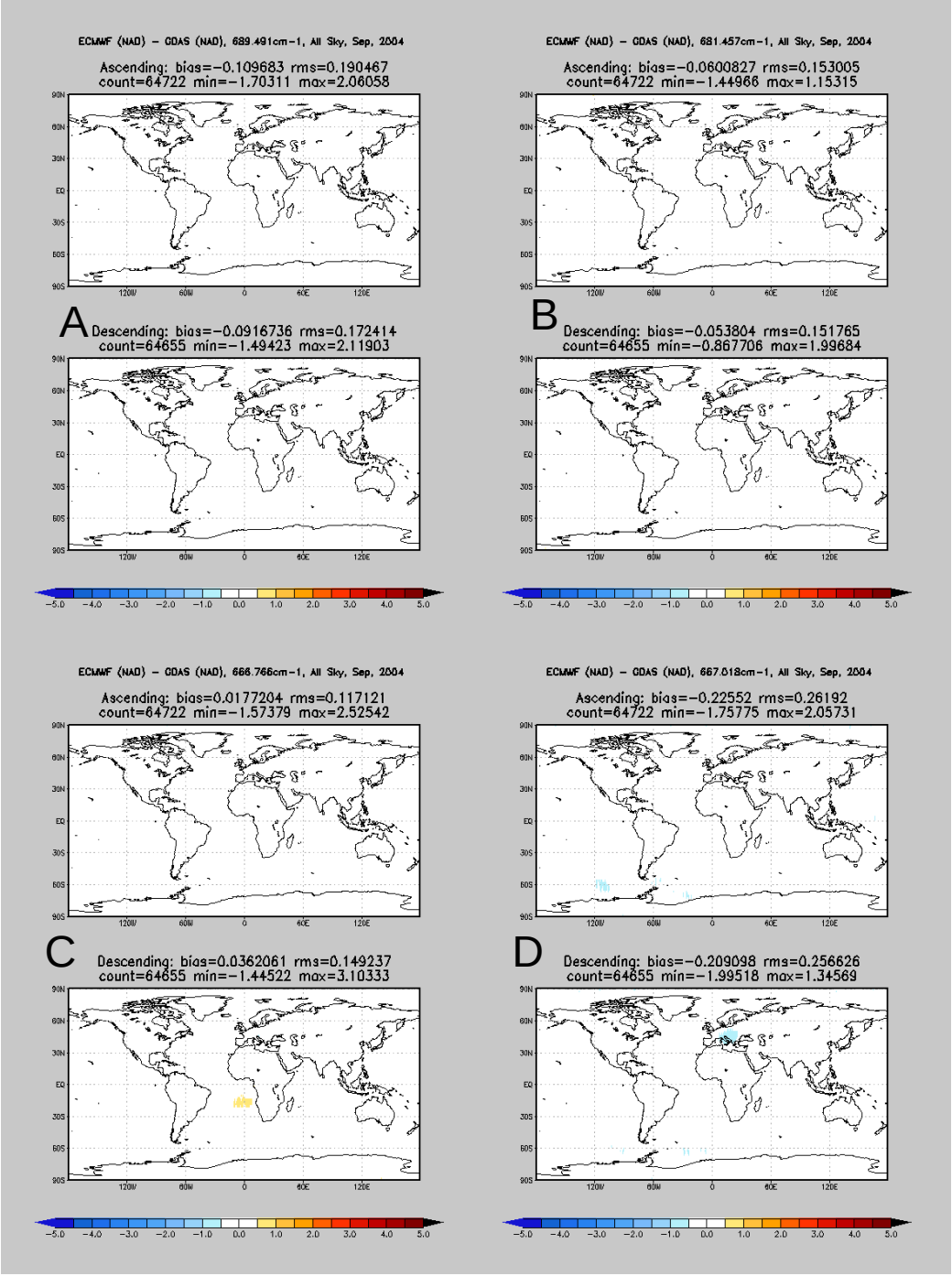

Fig. 5.8: ECMWF minus GDAS simulated brightness temperatures for A: 689.491 cm^{-1} (150 mb), B: 681.457 cm^{-1} (90 mb), C: 666.766 cm^{-1} (40 mb), and D: 667.018 cm^{-1} (25 mb)

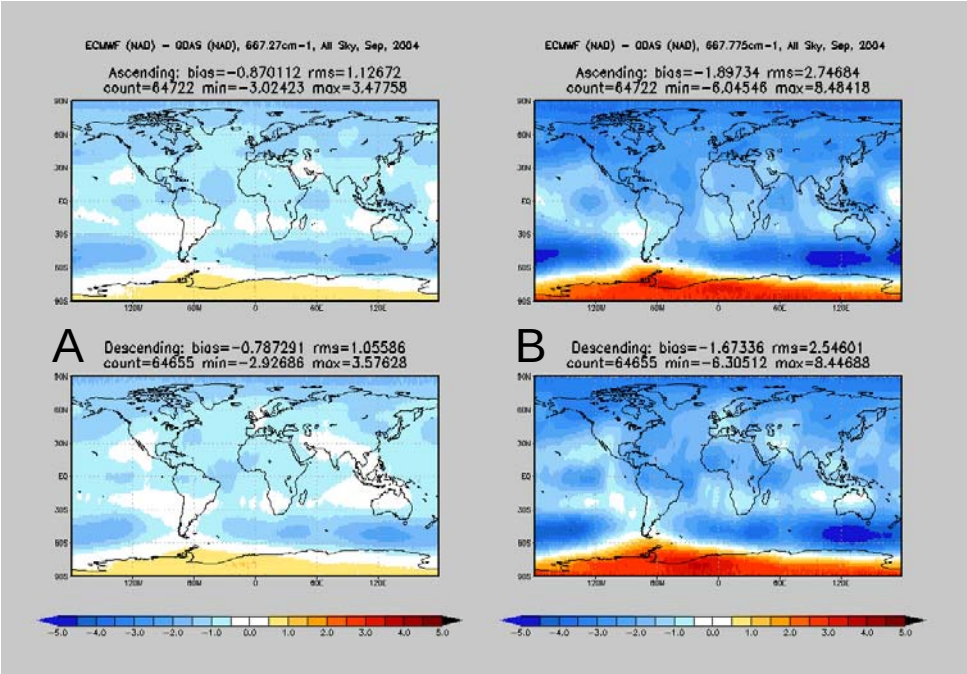

Fig. 5.9: ECMWF minus GDAS simulated brightness temperatures for A: 667.27 cm^{-1} (15 mb) and B: 667.775 cm^{-1} (1.5 mb)

For comparing and validating NCEP and ECMWF water vapor fields, two channels at 1519.07 cm^{-1} and 1598.45 cm^{-1} were selected representing upper and mid tropospheric water vapor, respectfully. The difference fields for those channels are given in Fig. 5.10. The differences for the water vapor channels are significant. As is shown in Fig. 3.6, a 1.25 K difference is about a 15% change in water vapor. In Fig. 5.10, the bias is also 1.25 K for the upper tropospheric water vapor channel.

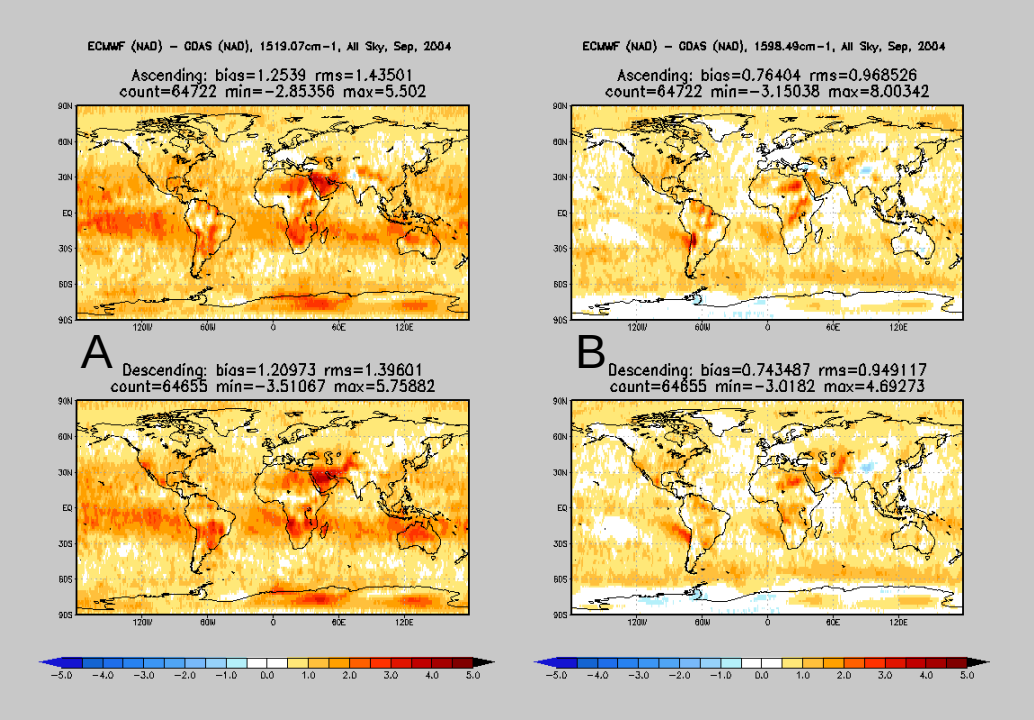

Fig. 5.10: ECMWF minus GDAS simulated brightness temperatures for A: 1519.07 cm^{-1} (315 mb) and B: 1598.45 cm^{-1} (490 mb)

5.5 Validation of the model fields using the AIRS clear-sky radiance climatology

In the previous section, discrepancies between NCEP and ECMWF model analyses were found in the simulated brightness temperatures of the channels sensitive to the temperature fields of the upper stratosphere and the tropospheric water vapor fields. Otherwise the brightness temperature fields for channels sensitive to the troposphere and lower stratosphere were quite similar for NCEP and ECMWF. When compared with measured AIRS brightness temperatures, one can make an assessment of the accuracy of each model. Figure 5.11 show the differences between

limb adjusted AIRS with simulated ECMWF and NCEP brightness temperatures for 667.27 cm^{-1} (15 mb). Fig. 5.12 show the differences for 667.775 cm^{-1} (1.5 mb).

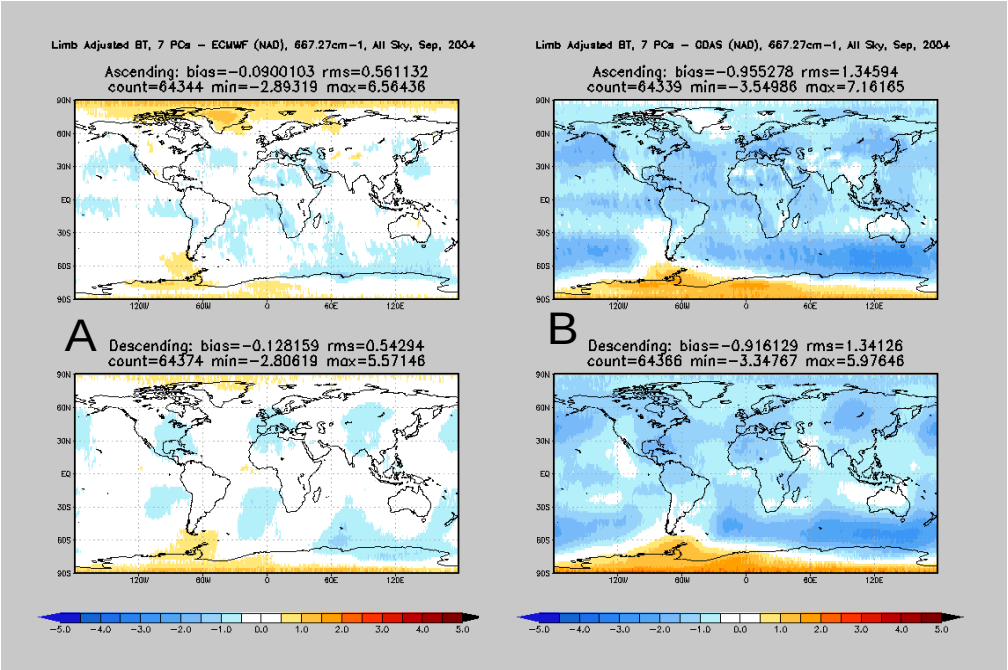

Fig. 5.11: Difference between limb adjusted AIRS and simulated ECMWF brightness temperatures (A) and with NCEP (B) for 667.27 cm^{-1} (15 mb)

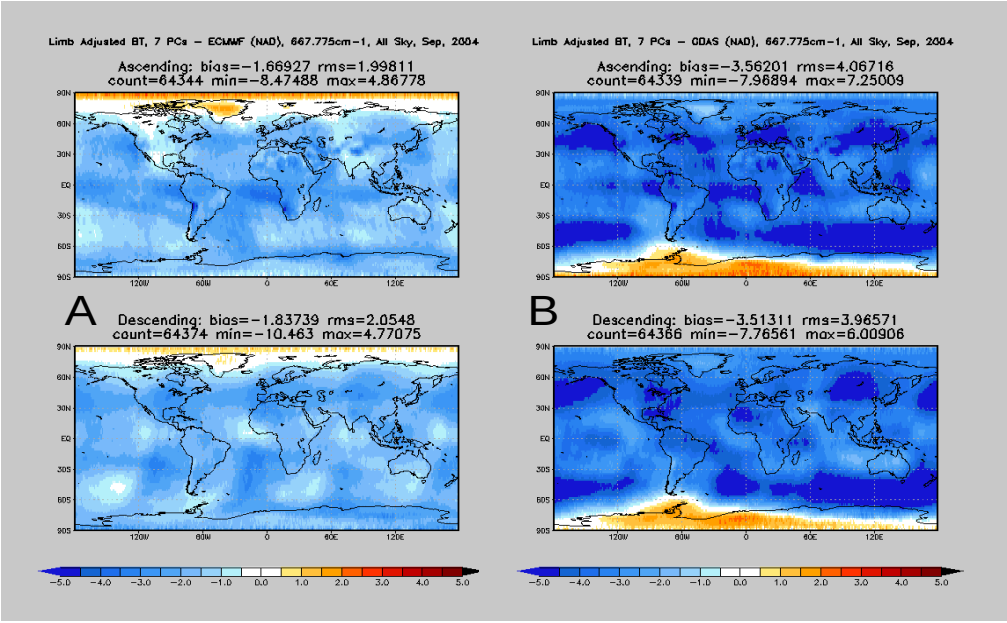

Fig. 5.12: Difference between limb adjusted AIRS and simulated brightness temperatures (A) ECMWF and (B) NCEP for 667.775 cm^{-1} (1.5 mb)

Based on the results given in Figs. 5.11 and 5.12, it is clear that the ECMWF temperature analysis is in better agreement with the AIRS radiance climatology. Note the exceptional agreement for the 667.27 cm^{-1} (15 mb) channel. The bias with ECWMF is only about -0.1 K, whereas with NCEP the bias is about - 1 K. In the case of the 667.775 cm-1 channel, ECMWF bias is about -1.7 K, whereas NCEP is about -3.6 K. At this level, there is not much observed data used to constrain the model. One can conclude that the ECMWF's temperature analysis in the upper stratosphere appears to be more accurate than NCEP's. As mentioned above, differences in the stratosphere are likely due to differences in model height and the data assimilated. However in the troposphere, any differences must be due to other causes. The differences for the water vapor channels, shown in Fig. 5.10, are particularly interesting and warrant further investigation.

Figure 5.13 shows the difference between the ECMWF and NCEP total precipitable water vapor fields and their mean for September 2003 and 2004. Both difference fields show a moist bias of about 1 mm in the NCEP field with respect to the ECMWF field.

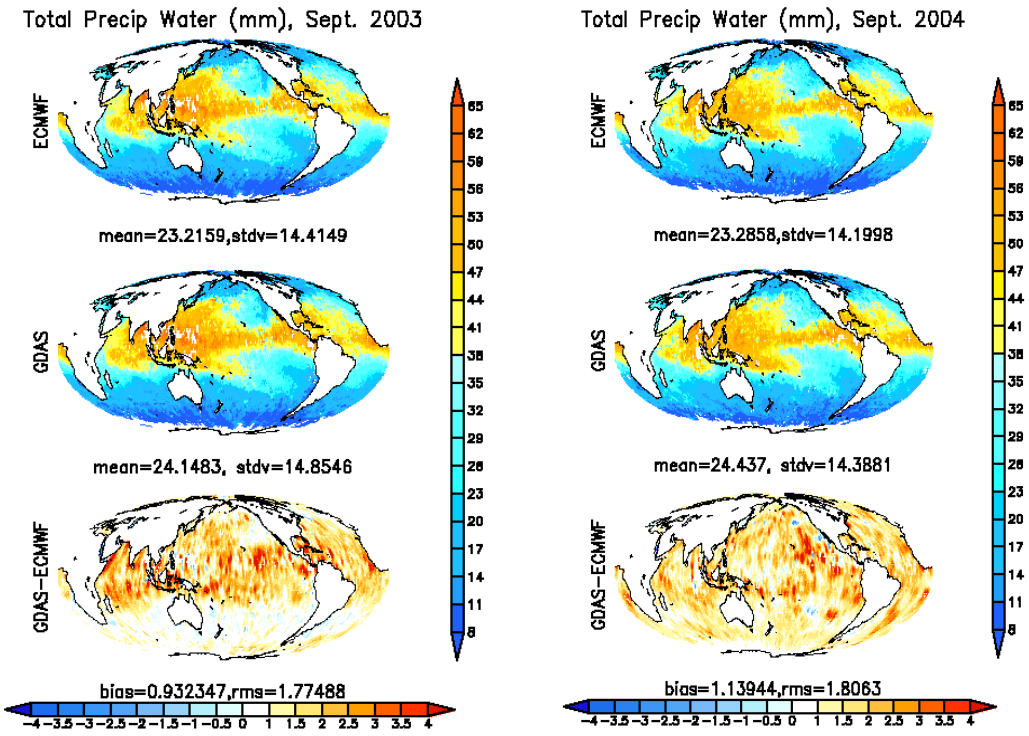

Fig. 5.13: Comparisons of ECMWF and GDAS Total Precipitable Water for September 2003 and 2004.

Figure 5.14 shows the difference between the ECMWF and NCEP total precipitable water vapor fields above 500 mb and their mean for September 2003 and 2004. Both difference fields show a moist bias of about 20% in the NCEP field. To determine which model analysis is most accurate with respect to water vapor, brightness temperatures are simulated using NCEP and ECMWF temperature and moisture analysis fields. Because the clear detection algorithm and the radiative transfer model are more accurate over ocean, and surface emissivity is better known, the brightness temperatures simulations are restricted to ocean areas.

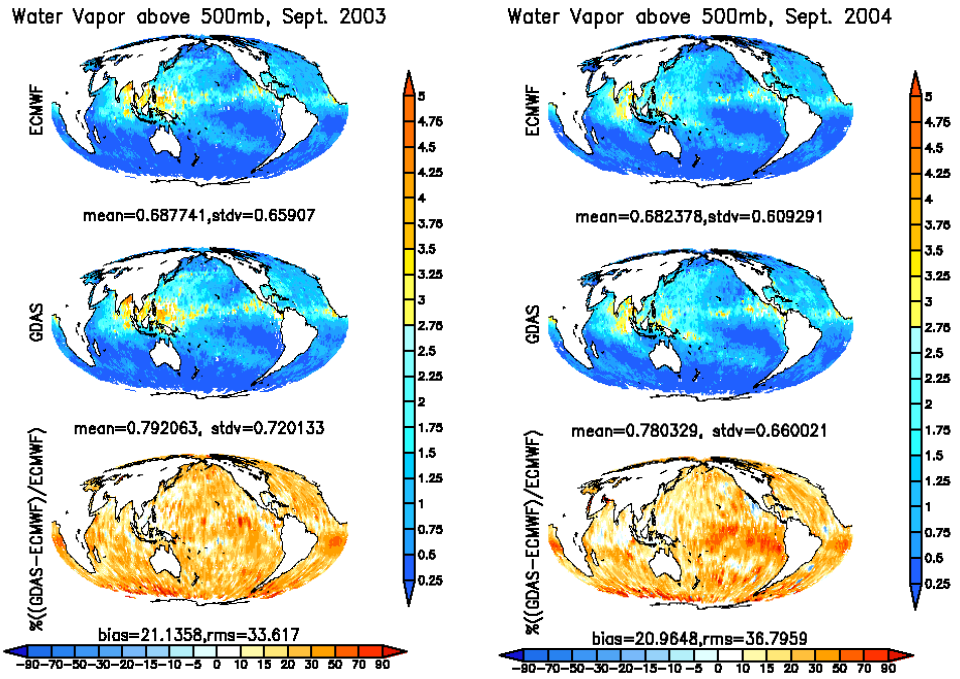

Fig. 5.14: Comparisons of ECMWF and GDAS above 500 mb precipitable water for September 2003 and 2004.

Figure 5.15 shows the ECMWF and NCEP biases (computed minus measured) for the entire AIRS spectral range for September 2003 and 2004. The clear detection algorithm threshold for the test 5 (comparisons with SST) was relaxed to allow for a larger population of clear cases, about 35% instead of just 5%. As a result, there is a positive bias of about 1 K for the window channels (800 -1000 cm^{-1}, 1070 – 1250 cm^{-1} and 2400 – 2650 cm^{-1}) due to low cloud contamination. However, for mid to upper tropospheric water vapor channels (1450 – 1600 cm^{-1}), the relaxed test does not introduce appreciable cloud contamination. Fig. 5.15, shows that the largest ECMWF bias in the water vapor region is about - 0.7 K, whereas for NCEP it is about -2.4 K.

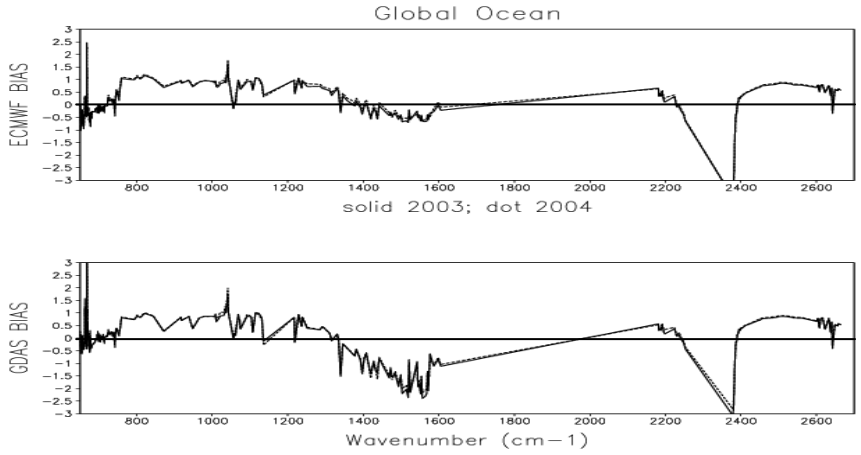

Fig. 5.15: Bias of AIRS measured minus computed from ECMWF (upper) and NCEP GDAS (lower) for September 2003 and 2004

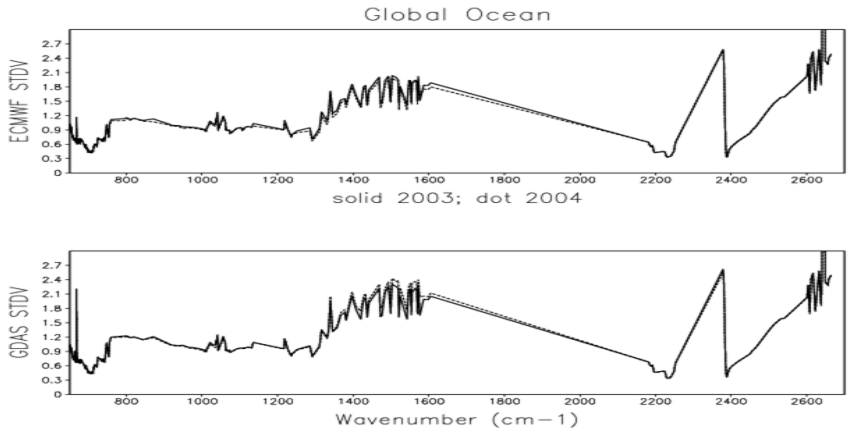

Fig. 5.16: Standard deviation of AIRS measured minus computed from ECMWF (upper) and NCEP GDAS (lower) for September 2003 and 2004

From Fig. 3.6, it can be inferred that a differences of the two biases, which is 1.7 K, results in a change in water vapor of about 20%, which is approximately the same value show in Fig. 5.14. The standard deviations of the computed minus measured differences are plotted in Fig. 5.16, which shows a lower standard deviation with respect to ECMWF. ECWMF started to assimilate AIRS radiances operationally in October, 2003, whereas NCEP operational use of AIRS began in May, 2005.

Inspection of Figs. 5.15 and 5.16 suggests a small impact of AIRS data in the ECMWF analysis, because the difference between September 2003 and 2004 appears to be small. However these figures represent a global average, so a closer examination is needed for the two water vapor channels discussed in section 5.4. Shown in Fig. 5.17 are the observed AIRS minus simulated ECWMF brightness temperatures for the 1519.07 cm^{-1} (315 mb) upper tropospheric water vapor channel, for September 2003, 2004 and 2005. Fig. 5.18 shows the comparable figure using the NCEP analysis. Fig. 5.17 shows relatively smaller biases for all three periods, demonstrating that ECMWF analysis water vapor fields were relatively accurate even before AIRS was assimilated. The rms was reduced by about 0.3 K. Note that the absence of locally large deviations after 2003. In Fig. 5.18, there was a very large reduction in the bias (September 2005) after AIRS was used operationally by NCEP. The bias was reduced by more than 1 K and the rms was reduced by nearly 1 K. Figs. 5.19 and 5.20 show the results for the mid-tropospheric 1598.45 cm^{-1} (490 mb) channel.

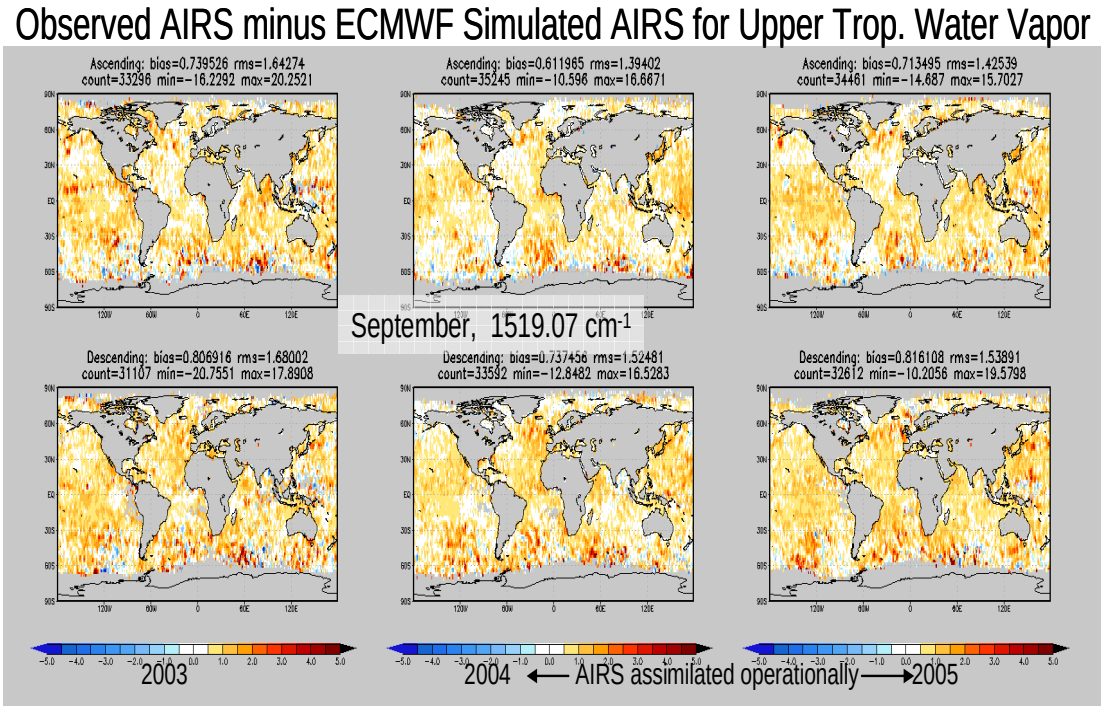

Fig. 5.17: Observed AIRS minus ECMWF simulated AIRS for upper tropospheric water vapor channel at 1519.07 cm^{-1} wavenumber.

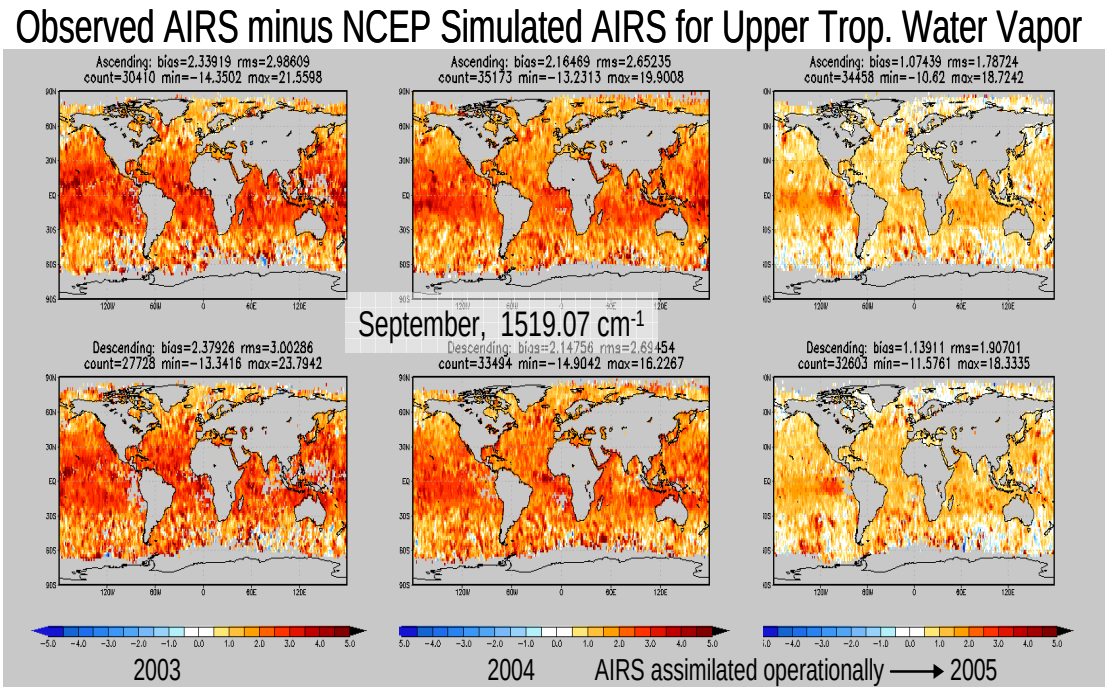

Fig. 5.18: Observed AIRS minus NCEP simulated AIRS for upper tropospheric water vapor channel at 1519.07 cm^{-1} wavenumber.

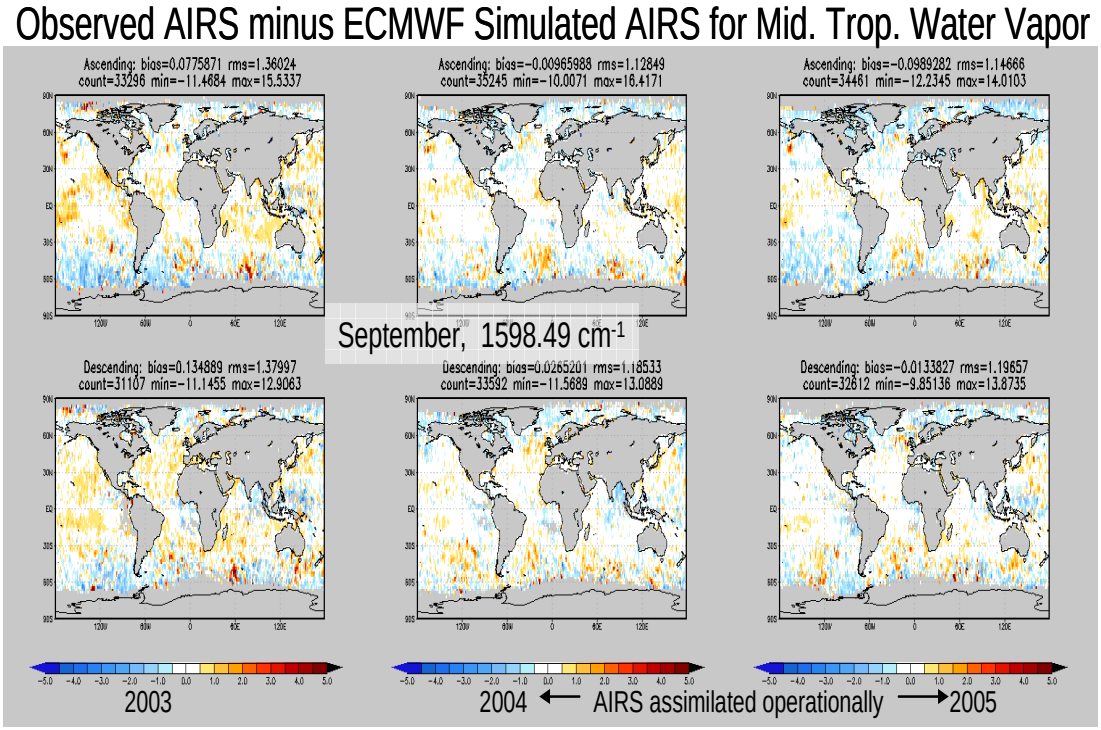

Fig. 5.19: Observed AIRS minus ECMWF simulated AIRS for middle tropospheric water vapor channel at 1598.45 cm^{-1} wavenumber.

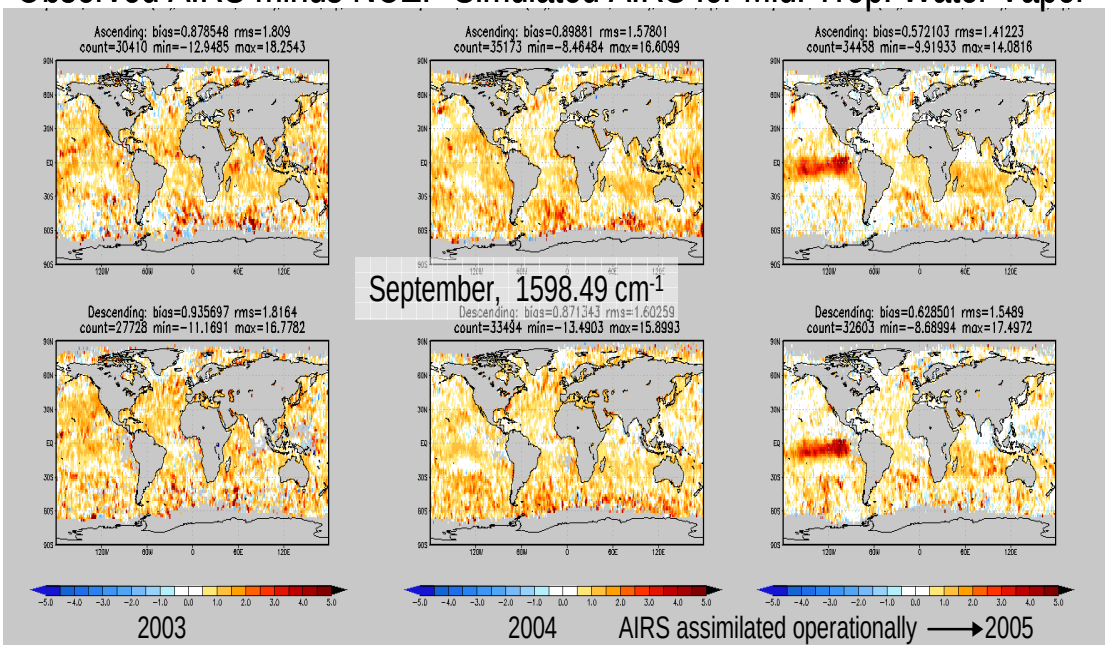

Fig. 5.20: Observed AIRS minus NCEP simulated AIRS for middle tropospheric water vapor channel at 1598.49 cm^{-1} wavenumber.

For the mid tropospheric channel, the ECMWF bias is only about 0.1 K. The bias does not change much over the three different years. However there is a reduction in the rms, from approximately 1.5 K to 1.15 K, after AIRS is assimilated operationally. In the case of NCEP, the bias is larger, about 0.9 K, however it does decrease to about 0.6 K in 2005, after AIRS is assimilated operationally by NCEP. There is a small reduction in the rms. However a large bias in excess of 4 K is found over the eastern Pacific just south of the equator. This is very interesting because the feature is nonexistent in ECWMF, and the cause remains unknown. In summary, the ECMWF analyses are shown to be more consistent with the AIRS radiance climatology. In the next section, the validation focuses on the consistency of interannual differences.

5.6 Interannual Differences

This section will compare interannual differences, (specifically September 2005 minus September 2004), of the model analyses, the original AIRS brightness temperatures and the limb adjusted brightness temperatures (i.e. the AIRS SRIR climatology). These comparisons will demonstrate the fidelity of the limb adjusted radiance climatology and the ECMWF analysis. The similarity of the annual differences derived from the limb adjusted radiance climatology and the ECMWF analysis will verify the accuracies of the ECMWF analysis, the AIRS radiance climatology, and the radiative transfer model. Figure 5.21a shows the interannual difference between September 2005 and 2004 for channel 704.436 cm^{-1}, which is an upper tropospheric temperature peaking near 350 mb. The left panel of the figure is the interannual difference of the unadjusted AIRS brightness temperature separated

into ascending and descending data; the center panel is for ECMWF simulated brightness temperatures for a scan angle of zero (nadir); and the right panel is for the limb adjusted brightness temperature. The patterns in the center and left panels are different as expected, since the left is an average of different viewing geometries (scan angles), and the center is for nadir observations.. The patterns in the center and right panels are nearly identical. Interannual differences from the ECMWF analysis and the AIRS radiance climatology are in excellent agreement. The interannual bias differs about 0.1 K. Note the patterns in the left panel, which are artifacts due to averaging observations from different scan angles and clearly demonstrate the importance of the limb adjustment. Figure 5.21b is very similar to Fig. 5.21a, however, the center panel is ECMWF simulated at the original scan angles. Now the center and left panels are virtually identical. This clearly demonstrates the fidelity of the radiative transfer model to simulate radiances at different scan angles. Figure 5.21c is similar to Fig. 5.21a; however, the center panel now represents annual differences simulated from NCEP analyses. The reason the left and right panels in Fig 5.21c are not exactly the same as those in Fig. 5.21a is my requirement that the same sample size be the same for all three panels of a given figure. In Fig 5.21c, the interannual difference from the NCEP analysis is about 0.2 K larger than the interannual differences from the limb adjusted AIRS brightness temperatures. The differences between the NCEP and ECMWF interannual differences for this particular AIRS temperature channel is relatively small, and this is to be expected since it was shown earlier that the NCEP and ECMWF temperature analyses in the troposphere and lower stratosphere are similar.

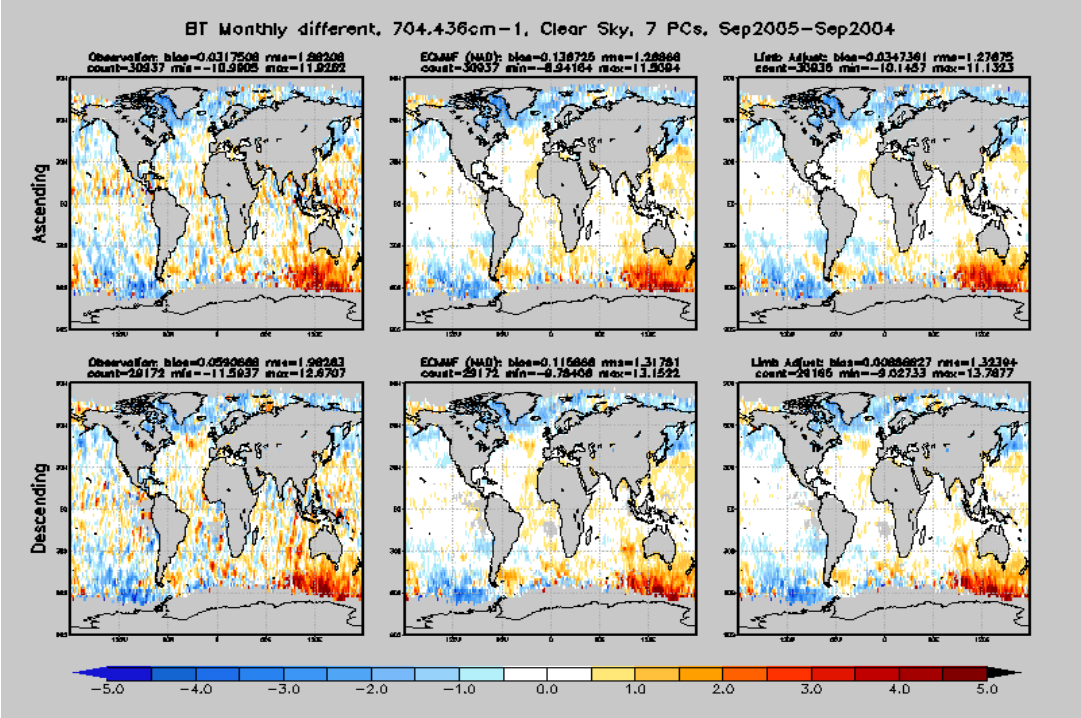

Fig. 5.21a: Annual difference between September 2005 and 2004 for AIRS channel 704.436 cm^{-1} for AIRS observation (left), AIRS simulated from ECMWF for nadir (center), and limb adjusted AIRS (right).

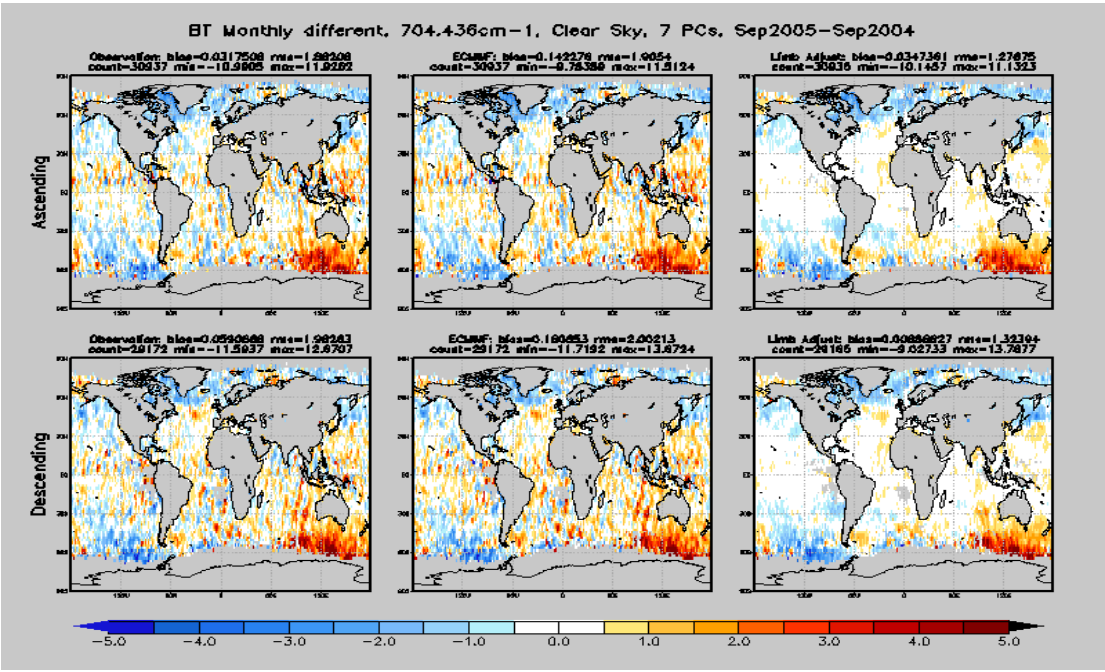

Fig. 5.21b: Annual difference between September 2005 and 2004 for AIRS channel 704.436 cm^{-1} for AIRS observation (left), AIRS simulated from ECMWF (center), and limb adjusted AIRS (right).

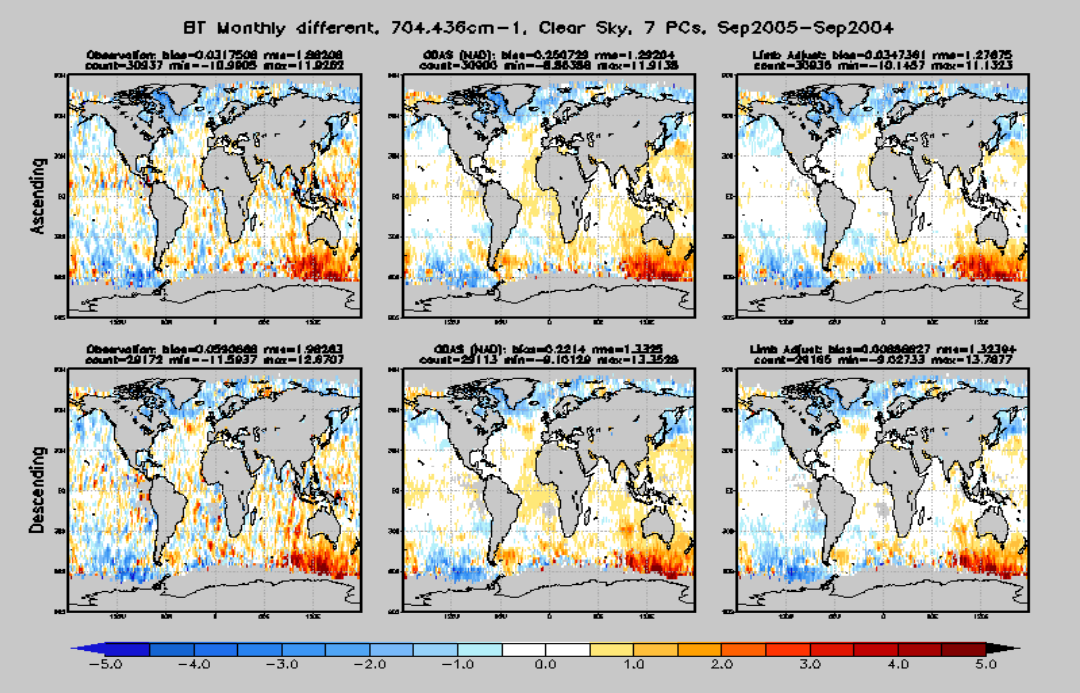

Fig. 5.21c: Annual difference between September 2005 and 2004 for AIRS channel 704.436 cm^{-1} for AIRS observation (left), AIRS simulated from NCEP for nadir (center), and limb adjusted AIRS (right).

Fig 5.22a shows the comparisons of interannual differences with ECMWF for channel 1519.07 cm^{-1}, which is the same upper tropospheric water vapor channel peaking near 315 mb discussed earlier. Note the excellent similarity of the center and right panels. Unlike the temperature channels, water vapor channels from the unadjusted AIRS observations (left panel) are also in good agreement. This is likely due to the fact that even though the path length increases as scan angle increases, the height of the channel weighting functions does not change considerably because water vapor exponentially decays with height. On the other hand for CO_2 temperature channels, CO_2 concentration, which is relatively constant with height, results in much larger absorption with increasing angles, thereby considerably

increasing the height of the weighting function. Visual inspections of the three panels show they are all very similar. However this is not the case when compared with NCEP, which is shown in Fig 5.22b. (Fig. 5.22b is the same as Fig. 5.22a; however the center panel is replaced with NCEP (GDAS).) The NCEP annual differences are very different from the limb adjusted annual differences. (Note similar findings for ECMWF and NCEP annual differences were found for differences between 2004 and 2003).

Figs. 5.23a and 5.23b are similar to Fig.5.22a and 5.22b, however the results are for the middle tropospheric water channel at 1598.07 cm^{-1}, which peaks near 490 mb. Again, ECWMF annual differences are very similar those generated from the AIRS SRIR climatology. With respect to NCEP, the agreement with the AIRS radiance climatology is indeed better than the upper tropospheric water vapor channel. However closer inspection will find discrepancies over the eastern Pacific just south of the equator, which was first noted in Fig. 5.20. Hence, we can conclude that the ECMWF water vapor analysis fields appear to be more accurate and realistic than those of NCEP.

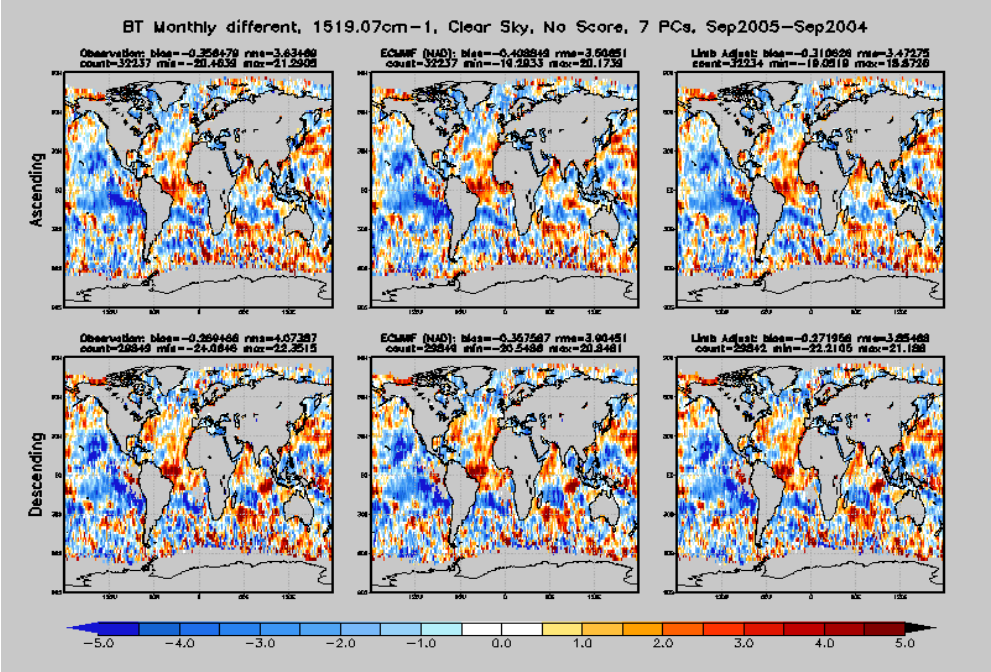

Fig. 5.22a: Annual difference between September 2005 and 2004 for AIRS channel 1519.07 cm^{-1} for AIRS observation (left), AIRS simulated from ECMWF for nadir (center), and limb adjusted AIRS (right).

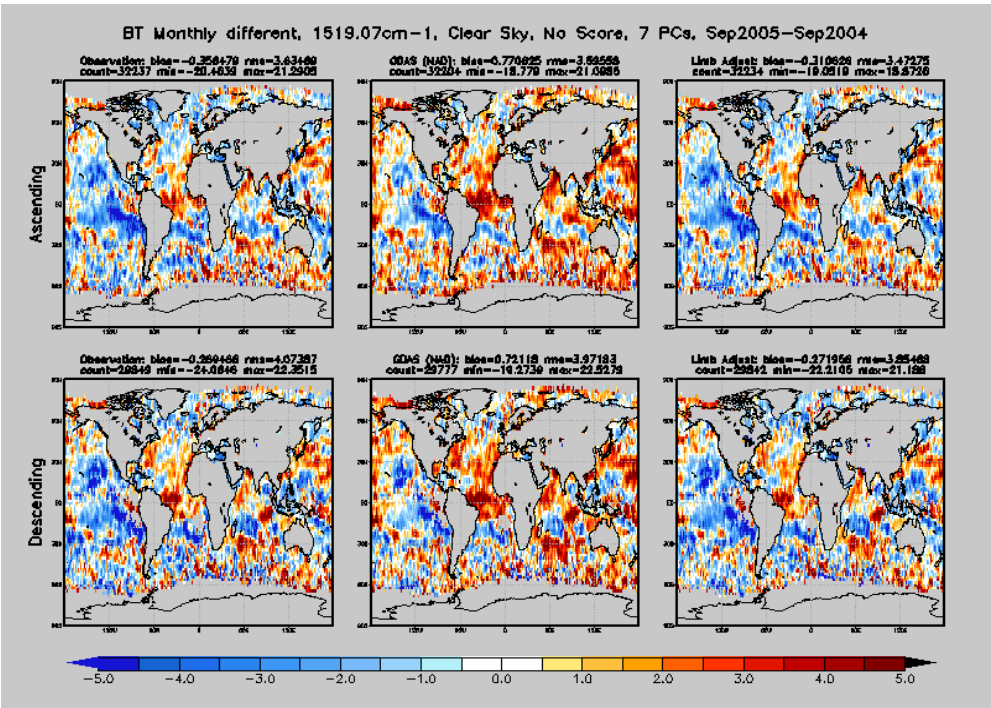

Fig. 5.22b: Annual difference between September 2005 and 2004 for AIRS channel 1519.07 cm^{-1} for AIRS observation (left), AIRS simulated from NCEP for nadir (center), and limb adjusted AIRS (right).

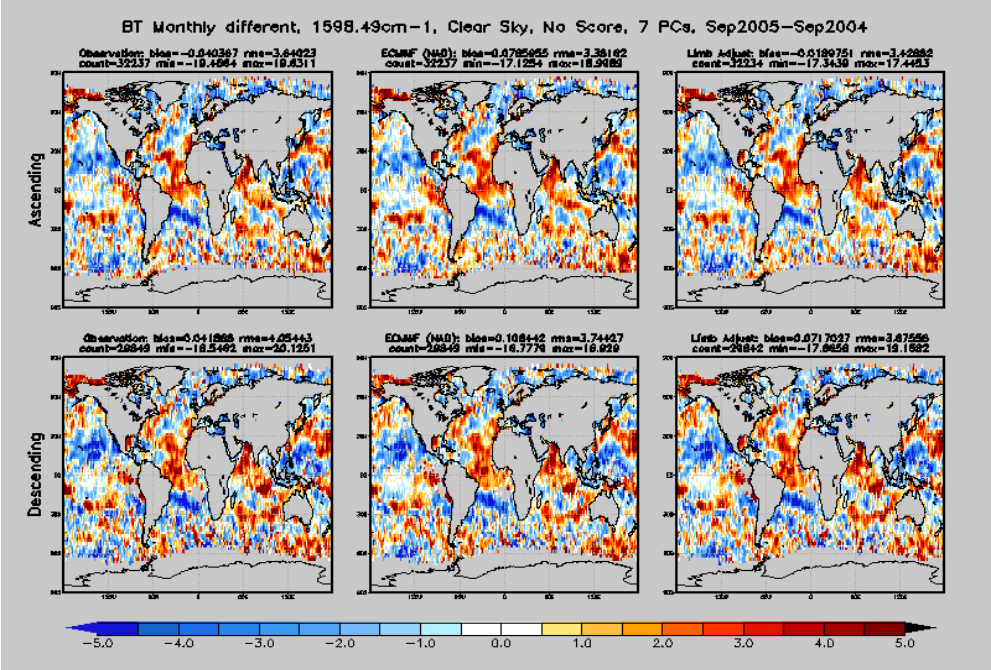

Fig. 5.23a: Annual difference between September 2005 and 2004 for AIRS channel 1598.49 cm^{-1} for AIRS observation (left), AIRS simulated from ECMWF for nadir (center), and limb adjusted AIRS (right).

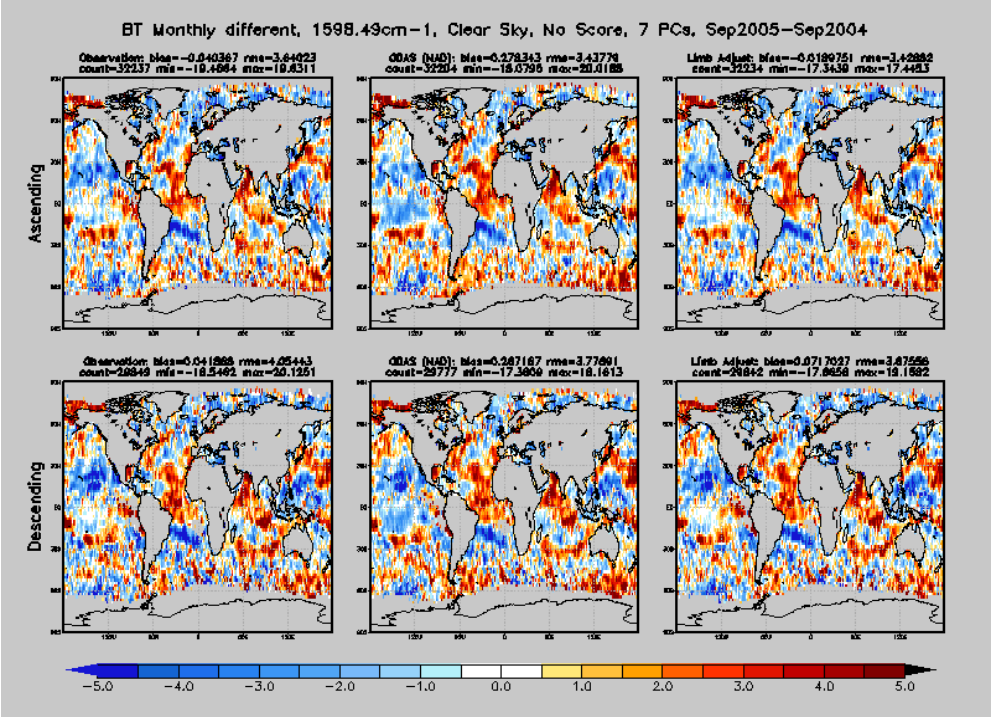

Fig. 5.23b: Annual difference between September 2005 and 2004 for AIRS channel 1598.49 cm^{-1} for AIRS observation (left), AIRS simulated from NCEP for nadir (center), and limb adjusted AIRS (right).

5.7 Summary of NCEP and ECMWF Analysis Validation

The AIRS radiance climatology has been demonstrated to have significant value in validating NWP model analyses. Based on the above results, one can conclude that, for the period of 2003 to 2005, ECMWF's analyses appear to be more accurate than NCEP's and in excellent agreement with AIRS observations, except for the upper stratosphere. Unfortunately, in 2006 the AIRS radiance climatology detected degradation in the ECMWF water vapor analysis, underscoring the importance of the AIRS data for ongoing validation. After an operational upgrade of the ECMWF data assimilation system in September 2006 to use an adaptive radiance bias correction scheme (McNally, private communication), the bias in the upper tropospheric water vapor channel for September 2006, shown in Fig. 5.24, increased significantly to 1.55 K from 0.71 K in September 2005 and is now larger than that of NCEP. Fig. 5.25 shows the biases for the lower tropospheric water channel for September 2006. The bias has increased to 0.43 K (September 2006) from -0.10 K September (2005); however the bias for this channel remains lower than the NCEP bias. Fig. 5.26 show the difference between the ECMWF and NCEP total precipitable water vapor fields, which is now much smaller, above 500 mb and their mean values for September 2005 and 2006

Table 2 is the tabulation of the biases given in Figs. 5.13 through 5.25. Notice how the precipitable water above 500 mb for ECMWF (row d) in 2006 departs significantly from the mean values for 2003 through 2006. The difference between NCEP and ECMWF precipitable water above 500 mb (row f), shown is only a fraction of a percent in 2006; in 2003 and 2004 it was about 21%, decreasing to

11.45% in 2005. Further inspection of Table 2 shows a strong relationship between rows m and f. Row m is the sum of rows i (the difference of the NCEP and ECMWF bias for 1519 cm^{-1}) and l (the difference of the NCEP and ECMWF bias for 1598 cm^{-1}). This should be expected since both channels together are more sensitive to the water vapor above 500 mb, as opposed to the total precipitable water. The relationship between the numerical values in rows f and m can be approximated very accurately with a polynomial expression ($f = 2.38 – 9.96m – 0.92m^2$) with Pearson correlation squared (r^2) of 0.9992.

The interannual differences for the upper tropospheric water vapor channel for both ECMWF and NCEP are given in Figs. 5.27a and 5.27b, respectively. The interannual differences for ECMWF are not nearly as similar to the limb adjusted interannual differences as they were for 2005 minus 2004. Large departures are highlighted by the elongated oval in Fig. 5.27a. Fig. 5.27a shows, for the first time, interannual differences that include the operational assimilation of AIRS data in both years by NCEP. The interannual differences are now closer to the limb adjusted values; however, some areas of large departures still exist as noted by the oval. The interannual differences for the lower tropospheric water vapor channel for both ECMWF and NCEP are given in Figs. 5.28a and 5.28b, respectively. Here the interannual differences of both models are similar to those obtained from the limb adjusted brightness temperatures.

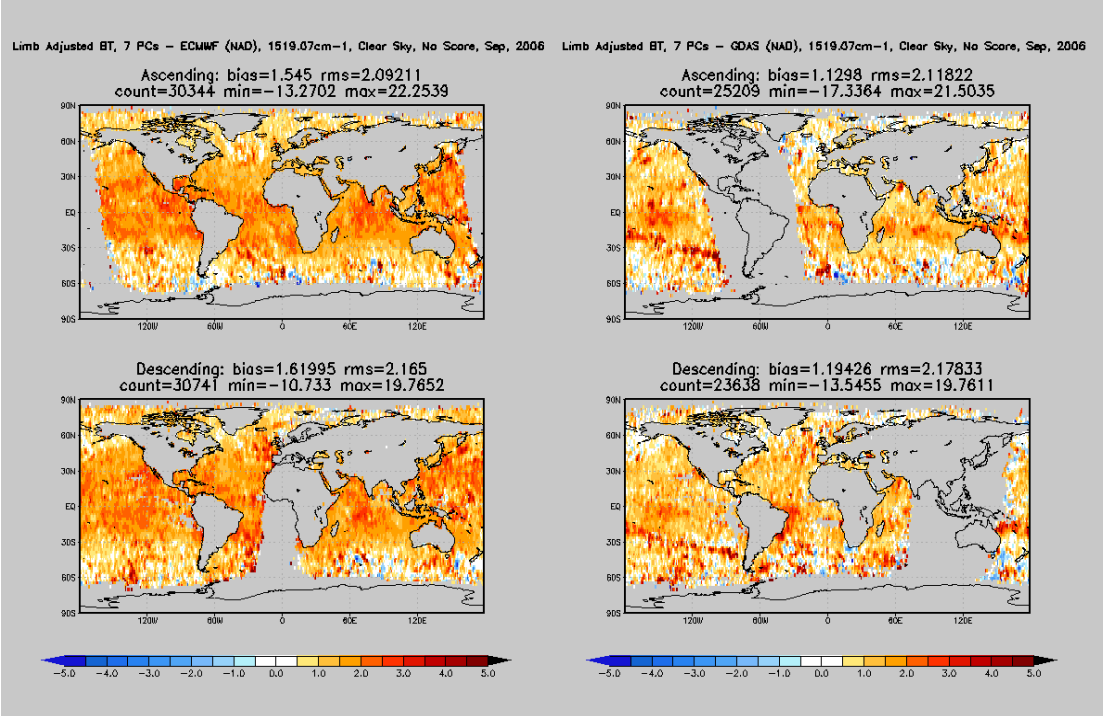

Fig. 5.24: Observed AIRS minus ECMWF simulated AIRS (left panel) and observed AIRS minus NCEP simulated AIRS (right panel) for upper tropospheric water vapor channel at 1519.07 cm^{-1} wavenumber for September 2006.

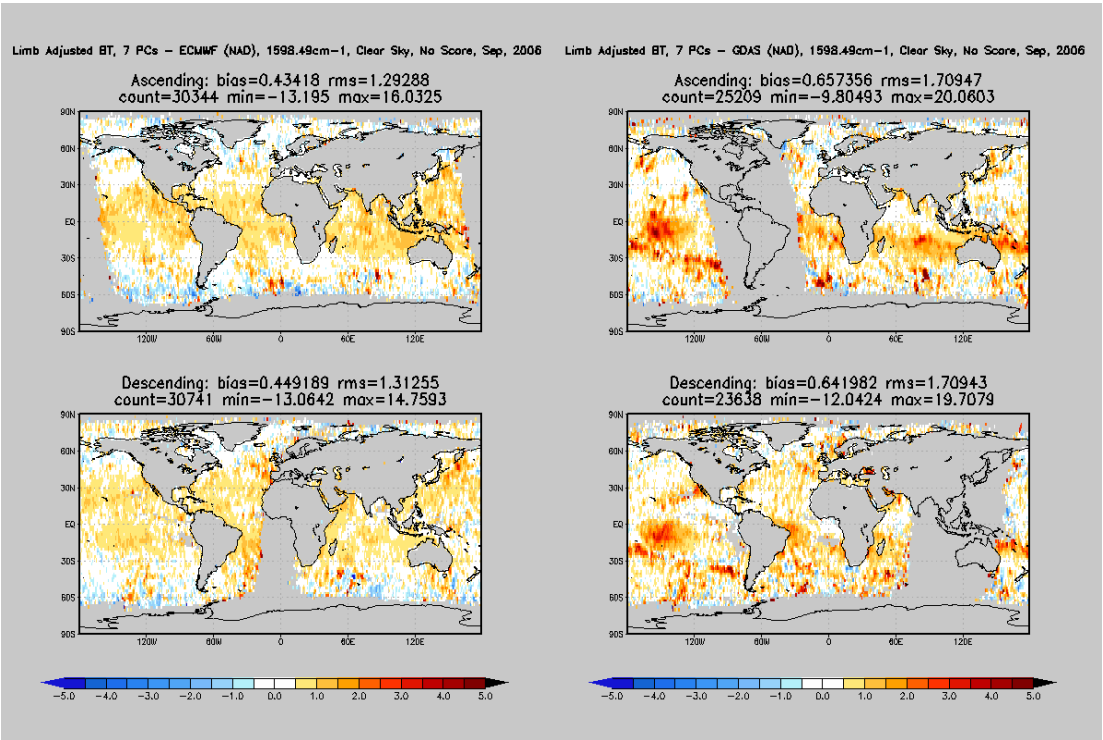

Fig. 5.25: Observed AIRS minus ECMWF simulated AIRS (left panel) and observed AIRS minus NCEP simulated AIRS (right panel) for lower tropospheric water vapor channel at 1598.49 cm^{-1} wavenumber for September 2006.

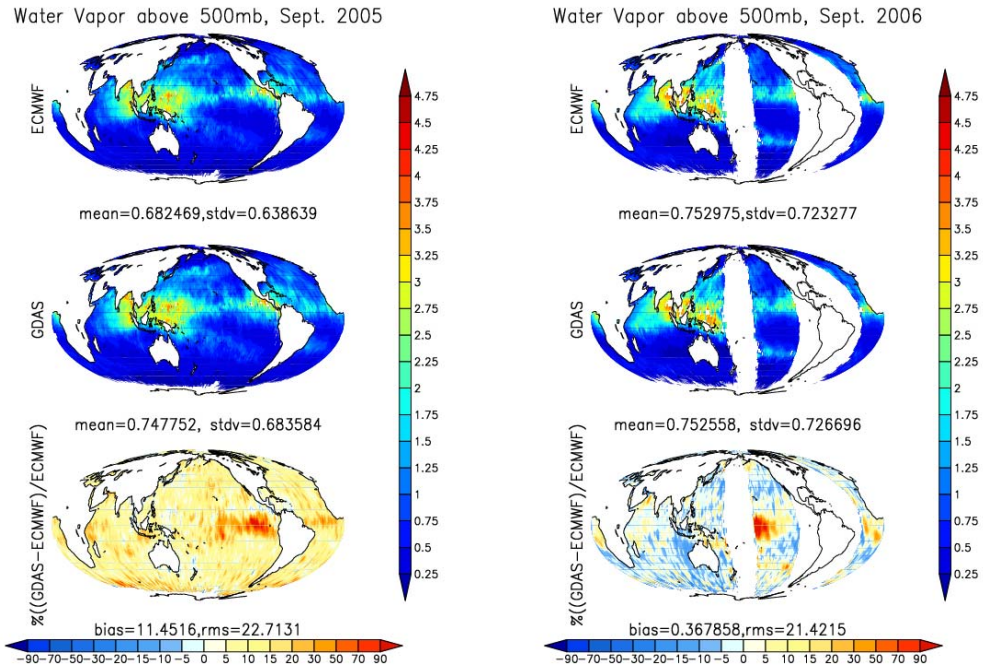

Fig. 5.26: Comparisons of ECMWF and GDAS precipitable water above 500 mb for September 2005 and 2006.

Table 5.1 Tabulated bias from Figs. 5.13 through 5.26

		2003	2004	2005	2006
a	ECMWF TPW	23.22 mm	23.29	22.70	22.34
b	NCEP TPW	24.15 mm	24.44	24.02	24.01
c	NCEP - ECMWF	0.93 mm	1.14	1.32	1.67
d	ECMWF PW above 500mb	0.69 mm	0.68	0.68	0.75
e	NCEP PW above 500 mb	0.79 mm	0.78	0.75	0.75
f	NCEP - ECMWF	21.14%	20.96%	11.45%	0.37%
g	ECMWF 1519cm^{-1}	0.73 K	0.61	0.71	1.55
h	NCEP 1519cm^{-1}	2.34 K	2.16	1.06	1.13
i	NCEP – ECMWF*	-1.61 K	-1.55	-0.35	0.42
j	ECWMF 1598cm^{-1}	0.10 K	-0.01	-0.10	0.43
k	NCEP 1598cm^{-1}	0.86 K	0.90	0.56	0.65
l	NCEP – ECMWF*	-0.76 K	-0.91	-0.66	-0.22
m	SUM OF DIFF*	-2.37 K	-2.46	-1.01	0.20

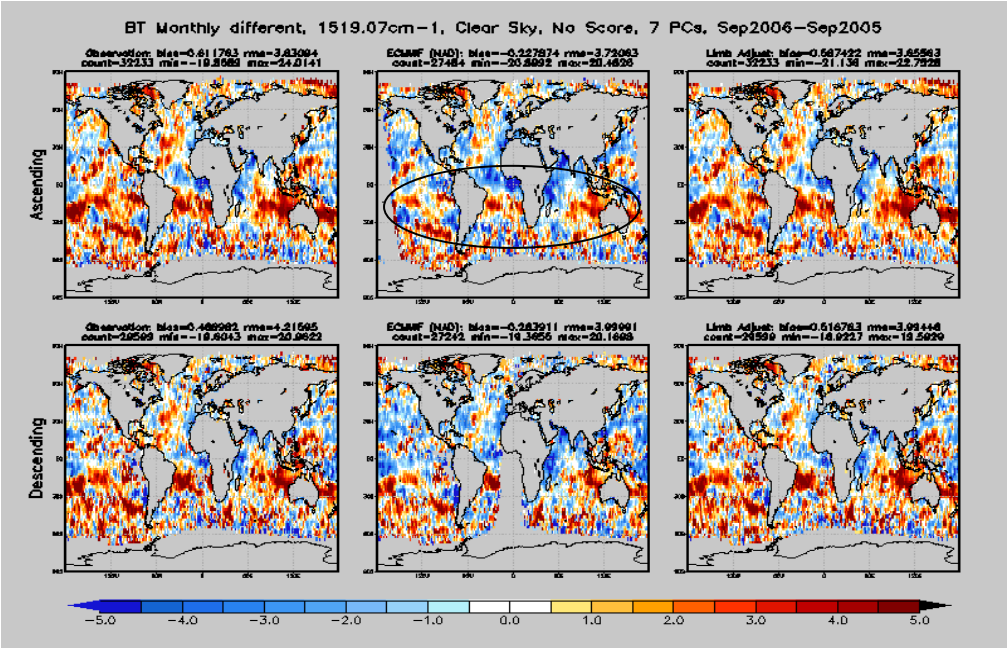

Fig. 5.27a: Annual difference between September 2006 and 2005 for AIRS channel 1519.07 cm^{-1} for AIRS observation (left), AIRS simulated from ECMWF for nadir (center), and limb adjusted AIRS (right).

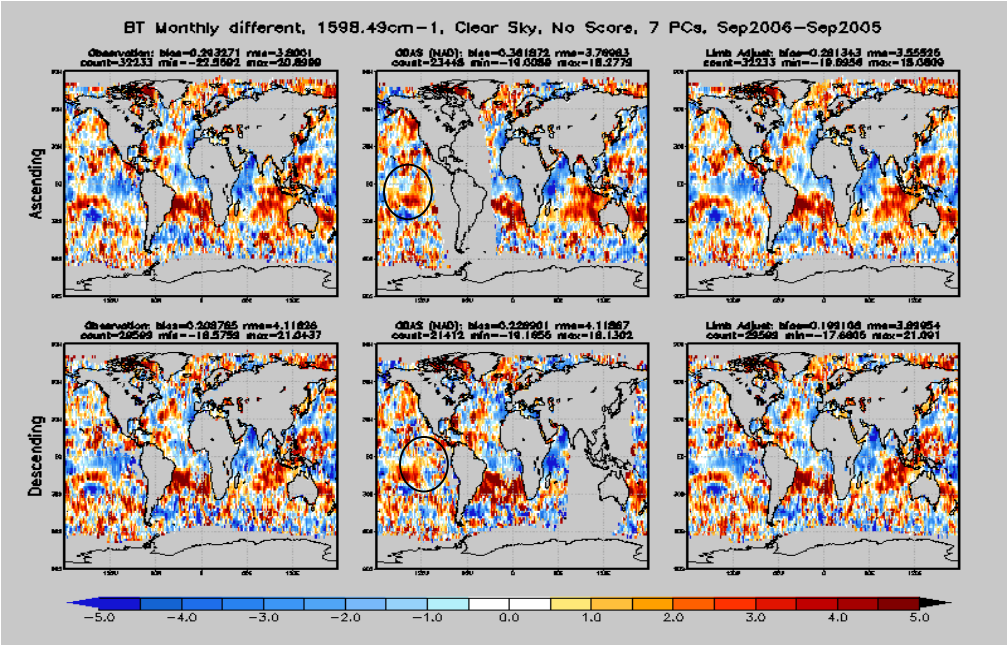

Fig. 5.27b: Annual difference between September 2006 and 2005 for AIRS channel 1519.07 cm^{-1} for AIRS observation (left), AIRS simulated from NCEP for nadir (center), and limb adjusted AIRS (right).

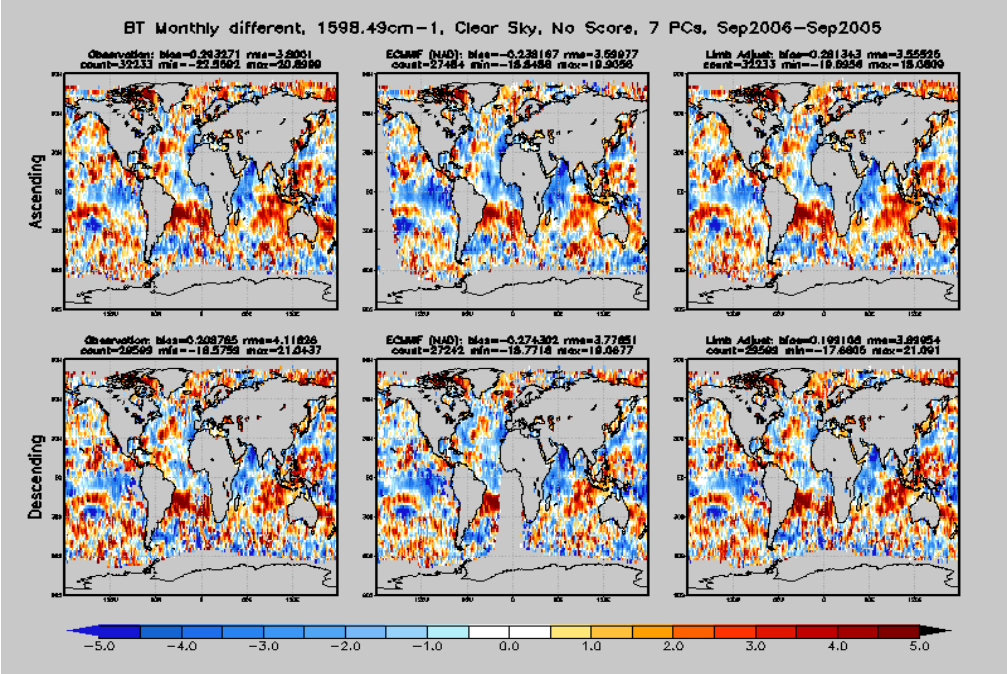

Fig. 5.28a: Annual difference between September 2006 and 2005 for AIRS channel 1598.49 cm^{-1} for AIRS observation (left), AIRS simulated from ECMWF for nadir (center), and limb adjusted AIRS (right).

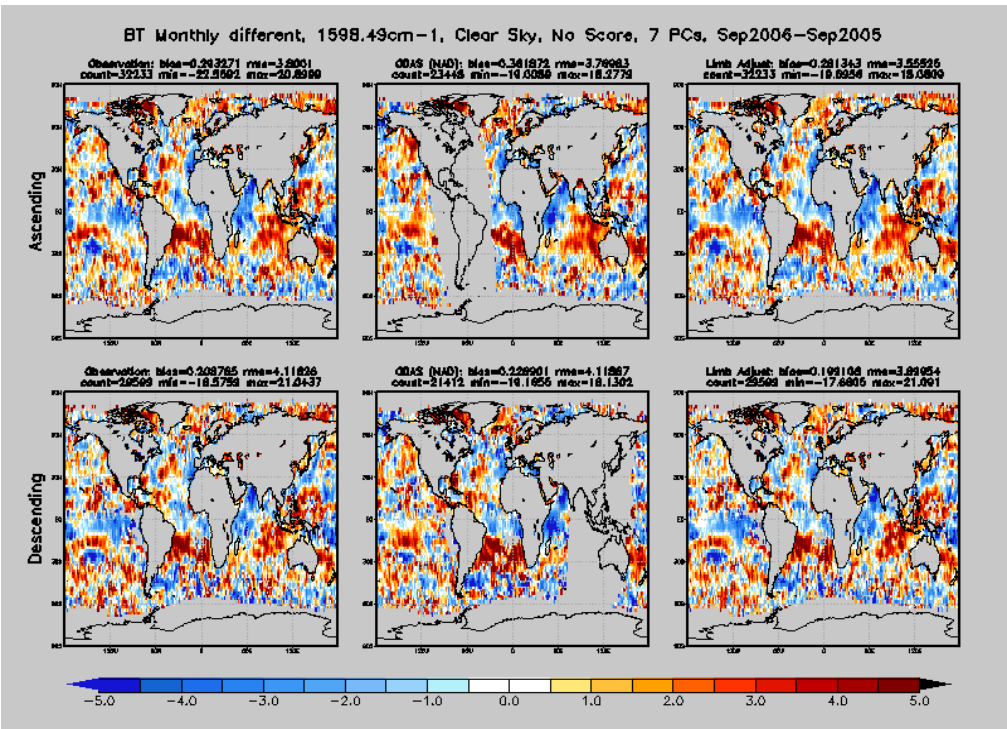

Fig. 5.28b: Annual difference between September 2006 and 2005 for AIRS channel 1598.49 cm^{-1} for AIRS observation (left), AIRS simulated from NCEP for nadir (center), and limb adjusted AIRS (right).

In summary, the SRIR climatology can validate model analyses and detect changes in both model physics and data assimilation procedures. The "golden years", when ECMWF's analyses agreed exceptionally well with the SRIR climatology, were 2003, 2004 and 2005. The above results have been reported to ECMWF.

Chapter 6: Summary, Conclusions and Further Study

The Spectrally Resolved Infrared Radiance (SRIR) climatology created in this research from AIRS observations is the first step in establishing a long-term record of thermal infrared radiances at high spectral resolution to help monitor climate change and assess the accuracy and realism of weather and climate analyses and forecasts.

Generation of the SRIR climatology required execution of the following procedures:

1. Screening the AIRS observations outliers
2. Converting the radiance observations to brightness temperatures (BT) and mapping them into ascending and descending orbit daily grids
3. Transforming the observations within the gridded datasets to principal component scores and stored in principal component (PC) gridded datasets
4. Adjusting the PC grids for viewing angle (limb darkening)
5. Computing viewing-angle adjusted brightness temperatures (AABT) from the PC datasets
6. Screening the BT and AABT daily datasets for clear sky values and averaging to produce monthly clear sky and all sky datasets.

Thus, the SRIR climatology consists of monthly brightness temperature datasets of two types – at the original viewing angle and adjusted for viewing angle to a nadir view - for the period 2003 – 2006 for:

5. Ascending (day), clear sky
6. Ascending, all sky
7. Descending (night), clear sky
8. Descending, all sky datasets

The monthly averaging of the original viewing angle is only for diagnostic purposes. The data must be angle adjusted for monitoring and validation applications.

This dissertation demonstrated the important applications of the SRIR dataset for monitoring interannual changes (section 5.2), and assessing the accuracy of atmospheric model analyses (sections 5.3 – 5.7). Interannual differences of less than 0.1 C in brightness temperature can be resolved, thus demonstrating the capability of the dataset for monitoring long term temperature trends. The ability of the dataset to monitor atmospheric composition changes was demonstrated by the detection of arctic ozone depletion in 2005. The ability to evaluate atmospheric analyses was demonstrated through comparisons of brightness temperatures simulated from NCEP and ECWMWF analyses with the dataset

The operational IASI on the MeTOP satellite series and the future operational CrIS on the NPOESS satellite series will provide continuous observations of high spectral resolution infrared radiances well into the 2020s. Both AIRS and IASI are now in orbit, and intercomparisons of both sensors have generally shown brightness temperature differences between the two sensors of less than 0.1 K [*Tobin et al.*, 2006]. Most importantly, the recently computed trend of the differences is less than .01 K per year, which means both sensors have the stability and the fidelity to accurately detect long term trends of at least a few tenths of a degree K per decade.

Follow-on missions will continue this type of measurement well into this century. Long-term stability of infrared sensors require internal blackbody targets with very high emissivities approaching unity (generally the requirement is > 0.9995). Both AIRS and IASI meet these requirements; however there is no internal monitoring to determine whether the high blackbody emissivity is maintained in orbit. This is why continuous intercomparisons between AIRS and IASI, and later CrIS is needed to demonstrate long term stability. NASA is considering a new mission called Climate Absolute Radiance and Refractivity Observatory (CLARREO), which measures outgoing radiances in the far, near and thermal infrared with high spectral resolution, high stability and internal monitoring. The CLARREO instrument will have a relatively large field of view (~ 100 km), and only nadir. It will have difficulty providing sufficient data sampling for examining regional trends and variability, however it can be used as a benchmark measurement to anchor operational instruments such as AIRS, IASI, and CrIS.

I plan to extend the time series of the SRIR climatology for AIRS into the future, and I plan to start generating the radiance climatology for IASI. Both climatologies will be publicly accessible and will be a NESDIS operational climate product. In addition to sensitivity to trace gases, the SRIR dataset includes signatures in radiative forcings due to changes in clouds, aerosols and surface emissivity. The dataset includes both clear and cloudy data, so cloud forcing studies can be conducted. The clear sky data will enable monitoring of changes in surface emissivity caused by changes in land surface conditions. I expect the SRIR

climatology to encourage research by those interested in monitoring climate change and variability, understanding radiative forcings, and validating models.

Bibliography

Aumann, H.H., M.T. Chahine, C. Gautier, M.D. Goldberg, E. Kalnay, L.M. McMillin, H. Revercomb, P.W. Rosenkranz, W.L. Smith, D.H. Staelin, L.L. Strow and J. Susskind 2003: AIRS/AMSU/HSB on the Aqua mission: design, science objectives, data products, and processing systems. *IEEE Trans. Geosci. Remote Sens*. **41**, 253-264.

Aumann, H.H., S. Broberg, D. Elliott, S. Gaiser and D. Gregorich 2006: Three years of Atmospheric Infrared Sounder radiometric calibration validation using sea surface temperature. *J. Geophys. Res*. **111**

Barkstrom, B. R.; 1984: The Earth Radiation Budget Experiment (ERBE). *Bull. Am. Meteorol. Soc*., **65**, 1170-1185.

Chahine, M.T., T.S. Pagano, H.H. Aumann, R. Atlas, C. Barnet, J. Blaisdell, L. Chen, M. Divakarla, E. Fetzer, M. Goldberg, C. Gautier, S. Granger, S. Hannon, F.W. Irion, R. Kakar, E. Kalnay, B.H. Lambrigtsen, S.Y. Lee, J. Le Marshall, W.W. McMillan, L. McMillin, E.T. Olsen, H. Revercomb, P. Rosenkranz, W.L. Smith, D.H. Staelin, L.L. Strow, J. Susskind, D. Tobin, W. Wolf and L. Zhou 2006: AIRS: Improving weather forecasting and providing new data on greenhouse gases. *Bull. Amer. Meteor. Soc.*, **87**, 911-926.

Christy, J. R., R. W. Spencer, and W. D. Braswell, 2000: MSU tropospheric temperatures: Dataset construction and radiosonde comparisons. *J. Atmos. Oceanic Technol*., **17**, 1153-1170.

DeSouza-Machado, S. G., L. L. Strow, S. E. Hannon, and H. E. Motteler, 2006: Infrared dust spectral signatures from AIRS. *Geophys. Res. Lett.,* **33**, L038, doi:10.1029/2005GL024364.

Engelen, R. J., and A. P. McNally, 2005: Estimating atmospheric CO2 from advanced infrared satellite radiances within an operational fourdimensional variational (4D-Var) data assimilation system: Results and validation, *J. Geophys. Res.*, **110**, D18305, doi:10.1029/2005JD005982.

Goldberg, M. D., and H. E. Fleming, 1995: An algorithm to generate deep-layer temperature from microwave satellite observations for the purpose of monitoring climate change. *J. Climate*, **8**, 993-1004.

Goldberg, M. D., D. S., Crosby, and L. Zhou, 2001: The limb adjustment of AMSU A observations: methodology and validation. *J. Appl. Meteor*., **40**, 70-83.

Goldberg, M.D., Y. Qu, L.M. McMillin, W.W. Wolf, L. Zhou and M. Divakarla 2003: AIRS near-real-time products and algorithms in support of operational weather prediction. IEEE Trans. *Geosci. Remote Sens*., **41**, 379-389.

Goody, R.M., J. Anderson and G. North, 1998: Testing climate models: an approach. *Bull. Amer. Meteor. Soc*. **79**, 2541-2549

Huang H-L., and P. Antonelli, 2001: Application of principal component analysis to high-resolution infrared measurement compression and retrieval. *J. Appl. Meteor*., **40**, 365-388.

Intergovernmental Panel on Climate Change (IPCC). *Climate Change 2007: The Physical Science Basis*. Contribution of Working Group I to the Fourth

Assessment Report of the Intergovernmental Panel on Climate Change. Cambridge (UK): Cambridge University Press; 2007.

Kidwell, K.B. 2000: *NOAA KLM Users Guide: NOAA Polar Orbital Environmental Satellites (POES).* U.S. Department of Commerce. National Oceanic and Atmospheric Administration, Satellite Data Services Division, Washington, D.C. Revised September 2000. http://www2.ncdc.noaa.gov/docs/klm/

Le Marshall, J., J. Jung, J. Derber, M.T. Chahine, R. Treadon, S.J. Lord, M. Goldberg, W. Wolf, H.C. Liu, J. Joiner, J. Woolen, R. Todling, P. Van Delst and Y. Tahara, 2006: Improving global analysis and forecasting with AIRS. *Bull. Amer. Meteor. Soc*. **87**, 891-894.

Maddy, E.S., C.D. Barnet, M. Goldberg, C. Sweeney and X. Liu, 2008: CO2 retrievals from the Atmospheric Infrared Sounder: Methodology and Validation. *J. Geophys. Res*. **113** D11301 doi:10.1029/2007JD009402, 7pgs.

Mears, C. A., M. C. Schabel, and F. J. Wentz, 2003: A reanalysis of the MSU Channel 2 tropospheric temperature record. *J. Climate*, **16**, 3650-3664.

Rodgers, C.D, 2000: Inverse methods for atmospheric sounding: Theory and practice. World Scientific Publishing 238 pgs.

Rosenkranz, P. W, 2003: Rapid radiative transfer model for AMSU/HSB channels, IEEE Trans. *Geosci. Remote Sens*., **41**(2), 362 – 368, doi:10.1109/TGRS.2002.808323.

Schiermeier, Q., Arctic trends scrutinized as chilly winter destroys ozone, *Nature* **435**, 6 (5 May 2005) *Nature*, **449**, 382-383 (2007)

Smith, W.L., and H.M. Woolf, 1976: The use of eigenvectors of statistical covariance matrices for interpreting satellite sounding radiometer observations. *J. Atmos. Sci.*, **33**, 1127-1203.

Spencer, R. W., and J. R. Christy, 1992a: Precision and radiosonde validation of satellite gridpoint temperature anomalies. Part I: MSU Channel 2. *J. Climate*, **5**, 847-857.

Spencer, R. W., and J. R. Christy, 1992b: Precision and radiosonde validation of satellite gridpoint temperature anomalies. Part II: Tropospheric retrieval and trends during 1979-90. *J. Climate*, **5**, 858-866.

Spencer, R. W., and J. R. Christy, 1993: Precision lower stratospheric temperature monitoring with the MSU: Technique, validation, and results 1979–1991. *J. Climate,* **6**, 1194–1204.

Strow, L.L., S.E. Hannon, S. DeSouza-Machado, H.E. Motteler and D.C. Tobin, 2006: Validation of the atmospheric infrared sounder radiative transfer algorithm. J. Geophys. Res. **111** D09S06 doi:10.1029/2005JD006 146, 24 pgs.

Strow, L.L., S.E. Hannon, S. DeSouza-Machado, H.E. Motteler and D.C. Tobin, 2003: An overview of the AIRS radiative transfer model. *IEEE Trans. Geosci. Remote Sens*., **41**, 303-313.

Susskind, J., C.D. Barnet and J.M. Blaisdell, 2003: Retrieval of atmospheric and surface parameters from AIRS/AMSU/HSB data in the presence of clouds. *IEEE Trans. Geosci. Remote Sens*. **41**, 390-409.

Tobin, D.C., H.E. Revercomb, R.O. Knuteson, B.L. Lesht, L.L. Strow, S.E. Hannon, W.F. Feltz, L.A. Moy, E.J. Fetzer and T.S. Cress, 2006: Atmospheric Radiation Measurement site atmospheric state best estimates for Atmospheric Infrared Sounder temperature and water retrieval validation. *J. Geophys. Res*., **111** D09S14 doi:10.1029/2005JD006103, 18 pgs.

Tobin, D.C., H.E. Revercomb, R.O. Knuteson, F.A. Best, W.L. Smith, N.N. Ciganovich, R.G. Dedecker, S. Dutcher, S.D, Ellington, R.K. Garcia, H.B. Howell, D.D LaPorte, S.A. Mango, T.S. Pagano, J.K Taylor, P. Van Delst, K.H. Vinson and M.W. Werner, 2006: Radiometric and spectral validation of Atmospheric Infrared Sounder observations with the aircraft-based Scanning High-Resolution Interferometer Sounder. *J. Geophys. Res*., **111** D09S02 doi:10.1029/2005JD006094, 14 pgs.

Vinnikov, K.Y. and N.C. Grody, 2003: Global warming trend of mean tropospheric temperatures observed by satellites. *Science*, **302**, 269-272.

Volz, F.E., 1973: Infrared optical constant of ammonium sulphate, Sahara Dust, volcanic pumice and flash, *Appl. Opt.,* **12**, 564-658

Wark, D.Q., and H.E. Fleming, 1966: Indirect measurements of atmospheric temperature profiles from satellites: I. Introduction. *Mon. Wea. Rev*., **94**, 351-362

Wielicki, B. A., Barkstrom, B. R., Harrison, E. F., Lee, R. B., Smith, G. L., Cooper, J. E., 1996: Clouds and the earth's radiant energy system (CERES): An earth observing system experiment, *Bull. Amer. Meteorol. Soc.*, **77** (5), 853–868.

Xiong, X., C. Barnet, E. Maddy, C. Sweeney, X. Liu, L. Zhou and M. Goldberg, 2008: Characterization and validation of methane products from the Atmospheric Infrared Sounder (AIRS). *J. Geophys. Res.*, **113** G00A01 doi:doi:10.1029/2007JG000500, 14 pgs.

Zou, C., Goldberg, M., Cheng, Z., Grody, N., Sullivan, J., Cao, C. and Tarpley, D., 2006: Recalibration of microwave sounding unit for climate studies using simultaneous nadir overpasses. *J. Geophys. Res.*, **111**, D19114: doi: 10.1029/2005JD006798, issn: 0148-0227.